Insight into the origins of metasomatism along the southern margin of the North Atlantic Craton, South Greenland

Brendan Hoare

2017

Declaration

I declare that this thesis has not been submitted as an exercise for a degree at this or any other university and it is entirely my own work.
I agree to deposit this thesis in the University's open access institutional repository or allow the library to do so on my behalf, subject to Irish Copyright Legislation and Trinity College Library conditions of use and acknowledgement.

Brendan Hoare

Abstract

The cratonic sub-continental lithospheric mantle (C-SCLM) has been isolated from mantle convection since it stabilised more than 2.5 billion years ago. Volatiles introduced into the C-SCLM drive metasomatism, ultramafic magmatism and diamond formation, yet the source of volatiles, their abundance and residence in the C-SCLM is poorly unconstrained.

The halogen composition of ultramafic lamprophyre (UML) provide an excellent opportunity to investigate the provenance of metasomatic agents in the C-SCLM. This thesis provides novel, combined elemental (F, Cl, and Br) and isotopic (δ^{37}Cl) halogen data for UML from the North Atlantic Craton (NAC), South Greenland. The UML display positively fractionated δ^{37}Cl compositions (+1.0 ‰ to +1.2 ‰), consistent with recycled halogens within the UML source region. The Br/Cl composition of the UML ranges from 0.0047 to 0.0049, precluding derivation from an asthenospheric source, instead suggesting addition of a high Br/Cl metasomatic component from the C-SCLM of the NAC. The data are consistent with a scenario in which halogen-enriched fluids were liberated from a subducting slab beneath the NAC at ~1.8 Ga and provide clear evidence of subduction metasomatism in the NAC. The favored scenario for the halogen enrichment of the NAC follows that Br and Cl were delivered into the overlying C-SCLM of the NAC from fluids/melts released from serpentinized oceanic peridotite during antigorite dehydration. The high F/Cl of both UML comparative to fluids released during antigorite dehydration but low F/Cl comparative to kimberlite likely results from the mixing of a depleted upper mantle melt in terms of F/Cl and a low F/Cl and enriched Br and Cl component relative to depleted upper mantle in the C-SCLM.

Variation in whole-rock mantle incompatible trace element compositions of both UML suggest the sampling of a spatially heterogeneous C-SCLM. The spatial position of UML at Nigerdlikasik relative to those from Pyramidefjeld could suggest the trace element enriched MARID source sampled by UML at Nigerdlikasik. This could reflect a flux of incompatible trace elements released at greater depth in subduction in addition to fluids/melts released during antigorite dehydration. The similarities between UML from Nigerdlikasik and lamproite from Aillik Bay could demonstrate an as yet unrecognized link between the lamproite source region at Aillik Bay and subduction metasomatism. In either case the δ^{37}Cl composition of MARID type phlogopite from the C-SCLM underlying Nigerdlikasik clearly demonstrates the potential of the formation, or retention, of subducted volatiles in the MARID suite. The constancy of Br/Cl and δ^{37}Cl compositions between UML at Nigerdlikasik and Pyramidefjeld, yet strong variation in incompatible trace element compositions suggest halogens released during antigorite dehydration can be effectively decoupled from traditional indicators used in the discrimination of subduction metasomatism. This work demonstrates that metasomatised C-SCLM domains have a capacity to record and preserve halogen signatures related to subduction metasomatism on billion-year timescales, allowing the discrimination of agents involved in metasomatism of ancient C-SCLM regions.

Acknowledgments

First and foremost, I wish to thank my supervisor Dr Emma Tomlinson for providing me the opportunity of this M.Sc. project, her help and encouragement has been invaluable and I am excited to continue onward with a Ph.D project under her guidance. I would also like to thank my co-supervisor Dr John Caulfield who has been an invaluable soundboard for the entirety of the project.

I wish to also thank, Colin Reid, Leona O'Conner, Paul Guyett, Dr Teresa Ubide and Dr Thomas Riegler for assistance during SEM analysis, as well as Francis Hendron, Noel McGinley, Maura Morgan and Cora McKenna for technical assistance and sample preparation. I would like to extend thanks to the whole of the Department of Geology for the many beers enjoyed over these two years of study but especially Paul Guyett and Clare Stead for many a spicy evening.

Table of Contents

Chapter 1.0: Context of thesis 21

Chapter 2.0: Literature review 25

2.1. Lamproite, kimberlite and UML 25

2.1.1. Lamproite 25

2.1.2. Kimberlite 26

2.1.3. Ultramafic lamprophyre (UML) 28

2.2. The halogens elements: Novel tracers of mantle metasomatism? 29

2.2.1. Distribution of the halogen elements on Earth 29

2.2.2. Chemical behaviour of the halogen elements 33

2.2.3. Halogens as a tracer for volatile recycling in the mantle 34

2.2.4. Cl isotopes as a tracer of volatile recycling in the mantle 38

Chapter 3.0: Selected samples and sample petrology 41

3.1. Geological setting 41

3.2. Selected samples 44

3.3. Ultramafic lamprophyre petrology 45

3.4. Xenolith petrology 47

Chapter 4.0: Methods 55

4.1. Bulk-rock analysis 55

4.1.1. WD-XRF 55

4.1.2. $\delta^{37}Cl$ isotope by IRMS 55

4.2. Mineral analysis 57

4.2.1. SEM-EDX 57

4.2.2. LA-ICP-MS 58

Chapter 5.0: Results 63

5.1. Whole-rock geochemistry 63

5.1.1. Major and trace element compositions 63

5.1.2. Halogens 68

5.2. UML major element mineral chemistry 71

5.2.1. Olivine 71

5.2.2. Spinel 74

5.2.3. Phlogopite 74

5.3. Xenolith major and trace element mineral chemistry 80

5.3.1. Olivine 80

5.3.2. Clinopyroxene 80

5.3.3. Orthopyroxene 89

5.3.4. Phlogopite 89

5.3.5. Ilmenite 99

5.3.6. Spinel 99

Chapter 6.0: Discussion 103

6.1.1. Assessing potential crustal contamination 103

6.1.2. Late-stage fluid mobility 106

6.1.3. Crustal incorporation of halogens 107

6.2. Magma composition and classification 108

6.2.1 Magma composition and classification 108

6.2.1. Exsolution of halogens during UML emplacement 110

6.3. Whole-rock geochemistry and origins of halogens in UML 111

6.3.1. Option (i): Halogen systematics reflect sampling of a primordial mantle reservoir 111

6.3.2. Option (ii): Halogen systematics reflect sampling of the Earth's convecting mantle 112

6.3.3. Option (iii): Halogen systematics reflect interaction and emplacement within overlying C-SCLM 112

6.3.4. The halogens subduction pathway 114

6.3.5. A role for sediments? 116

6.3.6. Sensitivity of halogens for tracing subduction metasomatism in the C-SCLM 118

6.3.7 Halogens in kimberlites and related rocks: implications from UML of South Greenland 119

6.3.8. Review of the subduction model 120

6.4. Evidence of metasomatism from xenoliths 121

6.5. Petrogenesis of the Nigerdlikasik and Pyramidefjeld UML suites 125

7.0 Synthesis 129

References 133

Figure Contents

Figure 1: εSr vs εNd for Type-I and Type-II clinopyroxene as well as whole-rock data for kimberlite and orangeite, modified from Grégoire et al., (2002)……..…27

Figure 2: Br (p.p.b.) vs Cl (p.p.m.) for mantle melts from glasses in MORB and OIB from the Atlantic, Pacific and Indian Oceans and High $^{3}He/^{4}He$ from Baffin Bay, Canada. Data taken from Kendrick et al., (2017 and references therein)……..……...…35

Figure 3: Compilation of reported Br/Cl and $\delta^{37}Cl$ for mantle melts (MORB: mid-ocean ridge basalt; HIMU 'high-μ': defined as mantle domains with highly radiogenic Pb isotope compositions; EM-I: enriched-mantle I; EM-II: enriched-mantle II), subduction inputs, subdcution outputs, and eclogite-facies ophiolites. Blue shaded field demarks the range of Br/Cl of HIMU, EM-I, EM-II and MORB reported to date. Data reported for mantle melts (Kendrick et al., 2017 and references therein), subduction inputs (Muramatsu et al., 2007; John et al., 2011; Kendrick et al., 2013; Chavrit et al., 2016; Li et al., 2017), subduction outputs (John et al., 2011; Kendrick et al., 2013; Kendrick et al., 2014) and eclogite-facies ophiolite (John et al., 2011). Data for $\delta^{37}Cl$ [‰ versus standard marine ocean chloride (SMOC)] (Barnes et al., 2017 and references therein)…..36

Figure 4: F vs Cl data for Atlantic, Pacific and Indian ocean MORB and Enriched Mantle-I (EM-I), Enriched Mantle (EM-II), HIMμ and Kimberlite. F and Cl data for MORB, OIB (Kendrick et al., 2017) and Kimberlite (Paul et al., 1976; Kjarsgaard et al., 2009). *Kimberlite data from Paul et al., (1976) was obtained through spectrophotometry is shown in filled squares……...37

Figure 5: $^{206}Pb/^{204}Pb$ vs $\delta^{37}Cl$ from Icelandic sub-aerial glasses modifed from Halldórrsson et al., 2016). $\delta^{37}Cl$ data for MORB (Sharp et al., 2007; Boniefacie et al., 2008), Enriched Mantle-I (EM-I) and Enriched Mantle-II (EM-II) and HIMμ (John et al., 2010). $^{206}Pb/^{204}Pb$ data from PetDB database (www.earthchem.org/petdb).....39

Figure 6: A simplified geological map of the North Atlantic Craton modified from Wardle and Hall, (2002) displaying UML, kimberlite and lamproite localities from (Nelson, 1989; Tappe et al., 2004; Tappe et al., 2006; Tappe et al., 2007; Nielsen et al., 2009; Tappe et al., 2009; Tappe et al., 2011)……..42

Figure 7 (a-f): Photomicrographs of ultramafic lamprophyre (UML) and hosted mineral phases from Nigerdlikasik and Pyramidefjeld. Photomicrograph a: (Nigerdlikasik) and b: (Pyramidefjeld) displays the texturally heterogeneity of the UML studied. Photomicrographs b and c display macrocryst olivine. Olivine in c) is inferred to derive from the C-SCLM whilst d) is implied to have at least in part crystallized from the UML melt. e) Displays a scanning electron microscope image under a back-scatter electron detector which displays FeO zonation implying complex FeO evolution of the UML melt. f) Displays serpentinization of olivine that appears on a textural basis to be a magmatic feature……46

Figure 8 (a-e): Photomicrographs of 60-200μm thin-sections of C-SCLM xenoliths recovered from UML at Nigerdlikasik and Pyramidefjeld……...49 - 53

Figure 9: Calibration lines for volatile elements for WD-XRF analysis based on the following reference materials: AGV2, ALI, ANG, BCR2, BEN, BHVO1, BIR1, BR, DNC1, DRN, DTN, DTS1, DTS2, FKN, FtikiGA, GH, GSN, GSP2, IFG, MAN, MRG1, NIMD, NIMG, NIML, NIMN, NIMP, NIMS, PCC1, PMS, QLO1, RGM1, SDC1, STM1, SY2, SY3, UBN, W2, WSE…….……....56

Figure 10: % Recommended Standard Value (RSV) for reference materials that were used as quality monitors for all experiments plotted in order of atomic mass. Range bars represent 1s. For ease of comparison, an area has been shaded to highlight the data that is within the ± 5% of RSV……...……60
Figure 11: Major elements for ultramafic lamprophyre (UML) from Pyramidefjeld and Nigerdlikasik (this work) as well as other UML and kimberlite from the North Atlantic Craton, SW. Greenland. Data from Nielson and Jenson, (2005); Gaffney et al., (2007); Nielson et al., (2009); Tappe et al., (2011); Tappe et al., (2017)…….....66
Figure 12: Incompatible trace element variation diagrams for ultramafic lamprophyre (UML) from Nigerdlikasik and Pyramidefjeld normalized against primitive mantle of Sun and McDonough, (1989). Panel a) shaded field of UML from Sarfatoq (Gaffney et al., 2007; Nielson et al., 2009; Tappe et al., 2011), Panel b) shaded field of kimberlite from Maniitsoq (Nielson et al., 2009; Tappe et al., 2011). Panel c) shaded field of lamproite from Aillik Bay, Canada (Tappe et al., 2007)……..…67
Figure 13: Br/Cl and $\delta^{37}Cl$ composition of ultramafic lamprophyre (UML) from Nigerdlikasik and Pyramidefjeld with compilation of reported Br/Cl and $\delta^{37}Cl$ for mantle melts (MORB: mid-ocean ridge basalt; HIMμ 'high-μ': defined as mantle domains with highly radiogenic Pb isotope compositions; EM-I: enriched-mantle I; EM-II: enriched-mantle II) , subduction inputs, subdcution outputs, and eclogite-facies ophiolites.Blue shaded field demarks the range of Br/Cl of HIMU, EM-I, EM-II and MORB reported to date. Data reported for mantle melts (Kendrick et al., 2017 and references therein), subduction inputs (Muramatsu et al., 2007; John et al., 2011; Kendrick et al., 2013; Chavrit et al., 2016; Li et al., 2017), subduction outputs (John et al., 2011; Kendrick et al., 2013; Kendrick et al., 2014) and eclogite-facies ophiolite (John et al., 2011). Data for $\delta^{37}Cl$ [‰ versus standard marine ocean chloride (SMOC)] (Barnes et al., 2017 and references therein)…….....69
Figure 14: Br/Cl vs F/Cl for a variety reservoirs delivered in, and fluids released during, subduction as well as mantle derived melts. References; Sediments (John et al., 2011; Li et al., 2016), Mantle melts (Kendrick et al., 2017 and references therein), Fore-arc serpetinite (Kendrick et al., 2013), Volcanic ashes and lavas and veins in eclogite-facies ophiolite (John et al., 2011). Seafloor serpetinite field assuming F concentration of ~200 p.p.m. (Mevel et al., 2003) and Br/Cl from the range reported for seafloor serpentinites by Kendrick et al., (2013). Range in kimberlite F/Cl reported by (Paul et al., 1977; Kjarsgaard et al., 2009)……70
Figure 15: NiO vs Mg# in olivine (Mg / Mg + Fe) x 100 for macrocryst olivine (core and rim) as well as olivine from xenoliths recovered within ultramafic lamprophyre (UML) from Nigerdlikasik and Pyramidefjeld, shaded area displaying ultra-depleted olivine from Ubekendt Ejland (Greenland). Inset histogram displays frequency of Mg# of macrocryst olivine from UML……..73
Figure 16: Ti / (Ti + Al + Cr) and Cr / (Cr + Al) vs Fe_T^{2+} / (Fe_T^{2+} + Mg) for groundmass spinel from ultramafic lamprophyre (UML) for Nigerdlikasik and Pyramidefjeld. Panels a) and b) show kimberlitic spinel from Maniitsoq for comparison, and Panels c) and d) show UML spinel from Sarfartoq. Data from supplementary database of Nielsen et al., (2009) with a shaded field displaying areas of main density… 77
Figure 17: TiO_2 and Al_2O_3 vs Mg# (Mg / Mg + Fe) for groundmass phlogopite from ultramafic lamprophyre (UML) at Nigerdlikasik and Pyramidefjeld. Panels a) and b) show kimberlitic phlogopite from Maniitsoq, and Panels c) and d) show UML phlogopite from Sarfartoq. Data from supplementary database of Nielsen et al., (2009). Kimberlite field in Panel a) after Mitchell, (1995)……....79

Figure 18: Mg# in olivine vs modal (%) olivine in xenolith recovered from ultramafic lamprophyre (UML) for Nigerdlikasik and Pyramidefjeld compared to C-SCLM xenoliths from Greenland: Ubekendt Eijand (Bernstein et al., 2006); Wiedermann Fjord (Bernstein et al., 1998); Sarfartoq (Garrit, 2002) and Kaapvaal (Boyd, 1999). Schematic melting curve from Boyd, (1989)…….83

Figure 19: Incompatible and rare-Earth element (REE) trace element variation diagrams for clinopyroxene from C-SCLM xenoliths recovered from xenoliths (NX-02l NX-03) from ultramafic lamprophyre (UML) from Nigerdlikasik. Panel (a) normalized against primitive mantle of Sun and McDonough (1989). Panel (b) REE normalized against chondrite of (McDonough and Sun, 1995). Dark grey field displays range of compositions of Type-I type clinopyroxene of the phlogopite-ilmenite-clinopyroxene (PIC) assemblage of Grégoire et al., (2002). Dark grey field displaying range of compositions of mica (phlogopite)-amphibole (K-richterite)-rutile-ilmenite-diopside assemblage of Dawson and Smith (1977) from Grégoire et al., (2002)……...……..…88

Figure 20: Al_2O_3 vs Mg# (Mg / Mg + Fe) for phlogopite from C-SCLM xenoliths recovered in ultramafic lamprophyre (UML) from Nigerdlikasik and Pyramidefjeld. Field for mica (phlogopite)-amphibole (K-richterite)-rutile-ilmenite-diopside (MARID) of Dawson and Smith (1977), based upon data from Dawson and Smith, (1977) and Waters, (1987a). Field for PIC based upon data from Jones et al., 1982 and Waters (1987b) reclassified by Grégoire et al., (2002) as belonging to the phlogopite-ilmenite-clinopyroxene (PIC) assemblage…...……..…96

Figure 21: Ba, Sr, Nb/Ta and Nb vs Cl for phlogopite from xenoliths recovered from ultramafic lamprophyre (UML) from Nigerdlikasik, South Greenland…….97

Figure 22: Nb/Ta vs Zr/Hf for phlogopite from mantle xenoliths recovered in ultramafic lamprophyre (UML) from Nigerdlikasik (NX-01; NX-02; NX-03) and Pyramidefjeld (PX-01) as well as whole-rock Nb/Ta vs Zr/Hf for UML. Chondritic Nb/Ta and Zr/Hf from McDonough and Sun, (1995). MARID for data phlogopite from Giuliani et al., (2015). Calculated trend of a mix of depleted residual peridotite (BP6-PE) of Weyer et al., (2003) and carbonatite (Chakhmouradian, 2006) modelled by Aulbach et al., (2013). Dark grey field displaying whole-rock kimberlite Nb/Ta vs Zr/Hf from Maniitsoq (Nielsen and Jensen, 2005; Nielson et al., 2009; Tappe et al., 2011) and light grey field displays UML compilation from the NAC (Tappe et al., 2004; Tappe et al., 2006; Gaffney et al., 2007; Nielsen et al., 2009; Tappe et al., 2011)……..98

Figure 23: Incompatible trace element diagram for ultramafic lamprophyre (UML) from Nigerdlikasik and Pyramidefjeld normalized against primitive mantle of Sun and McDonough (1989). For comparison average continental crust (ACC) of Rudnick and Gao, (2003) and shaded field showing range of compositions of lamproite from Aillik Bay, Canada (Tappe et al., 2007). Calculated 0.1% melt at 6 GPa is shown following the method of Tappe et al., (2011), they were obtained by utilizing the experimentally determined bulk peridotite/kimberlitic melt partition coefficients of Brey et al. (2008) using a batch partial melting equation of Dasgupta et al., (2009)……....104

Figure 24: Contamination index (C.I) of Clement, (1982) vs ln(Si / Al) for ultramafic lamprophyre (UML) from Nigerdlikasik and Pyramidefjeld. Contaminated and uncontaminated fields for Lac de Gras kimberlites, Canada, from Kjarsgaard et al., (2009). Data for uncontaminated Sarfartoq and Sisimiut. UML from (Gaffney et al., 2007; Nielsen et al., 2009; Tappe et al., 2011) and Faeringehavn from (Tappe et al., 2017)...……...…...105

Figure 25: MgO / CaO vs SiO / Al2 2 3O for ultramafic lamprophyre (UML) from Nigerdlikasik and Pyramid -efjeld. Compared with UML data from Sarfartoq (Gaffney et al., 2007;Nielsen et al., 2009; Tappe et al., 2011), Sisimiut (Nielsen et al., 2009), Faeringehavn (Tappe et al., 2017) and kimberlite from Maniitsoq (Gaffney et al., 2007; Nielsen et al., 2009; Tappe et al., 2011) and Tikiusaaq (Tappe et al., 2017). Fields for experimentally produced melt compositions from synthetic and natural carbonated peridotites under high pressures are after Gudfinnsson and Presnall (2005). UML-kimberlite discrimination from Rock, (1991). Arrows indicate recalculated compositions after subtraction of xenocrystic olivine……..…109

Figure 26: Kα series energy-dispersive X-ray scanning electron microscope (EDX-SEM) map of for chlorine (A) for serpentine veins in xenolith PX-01 recovered from ultramafic lamprophyre (UML) from Pyramidefjeld. Kα series foir Mg (bottom right) and back-scatter electron (BSE) image shown for comparison. White stippled field shows veins cross-cut by infiltration of UML…….....113

Figure 27: Clinopyroxene / carbonatite distribution coefficients (Kd) between clinopyroxene from xenoliths NX-02 and NX-03 from Nigerdlikasik and carbonatite from Coltorti et al., (1999). Shaded field shows the range in distribution coefficients (Kd) reported by Coltorti et al., (1999)……..122

Figure 28a: Schematic displaying the evolution of the North Atlantic Craton (NAC) through time. 1a displays the NAC at ~1.8 Ga with the ongoing subduction of oceanic slab from the South. Potential sources for fluids liberated from the oceanic slab is shown (1b); with sepentinized oceanic lithosphere (grey), metasomatised forearc mantle (blue) and a potential additional sedimentary source (e.g. sediments; dark grey) implied for Nigerdlikasik. 1b displays the NAC during extension and rifting associated with the opening of the Labrador Sea (~150 Ma), upward migration of the lithosphere-asthenosphere boundary (LAB) and localization of low-degree melts into the cratonic sub-continental lithospheric mantle (C-SCLM). Gardar magmatism is shown demonstrating the migration of UML magmatism into the craton interior through time……....126

Figure 28b: Schematic of the evolution of the cratonic sub-continental lithospheric mantle (C-SCLM) of the southern boundary of the North Atlantic Craton (NAC) through time. Panels 1-3 depict the C-SCLM underlying Pyramidefjeld. Panel 1 shows the highly depleted refractory C-SCLM of the NAC metasomatised by trace-element depleted fluids released from serpentine breakdown in the oceanic slab below the NAC at ~ 1.8 Ga. Panel 2 displays PIC-style metasomatism of the C-SCLM shortly prior to or during ultramafic lamprophyre (UML) emplacement. Panel 3 depicts the emplacement of the UML into the C-SCLM and assimilation/sampling of pre-existing highly depleted C-SCLM and preconditioned metasomatic C-SCLM. Panels 4-6 display the same scenario for Nigerdlikasik. The scenario for Nigerdlikasik deviates from that of Pyramidefjeld in that a pre-existing MARID or additional subducted sedimentary component that lead to formation of a MARID type assemblage, is present. This domain is subsequently metasomatised prior to or during emplacement generating a complex assemblage that manifests both PIC and MARID characteristics…….....127

Chapter 1.0: Context of thesis

A record of the formation, history and evolution of the Earth's continents is preserved within ancient regions of cratonic sub-continental lithospheric mantle (C-SCLM). The key characteristic of C-SCLM is the dominant signature of melt depletion, demonstrated by the consistently high #Mg (~92.5) of primary olivine (Bernstein et al., 2007), high bulk MgO and low bulk FeO, Al_2O_3, CaO contents. Such characteristics are widely considered to result from high degree melting (up to ~40%) of the Earth's primitive mantle (e.g. Boyd, 1989). Through studies of the modal mineralogy of C-SCLM xenoliths entrained within kimberlite and other similar magmas it is obviously apparent that phases have been introduced into the C-SCLM after melt extraction and depletion via 'modal' metasomatism (Harte, 1983) with the most obviously apparent those of the mica (phlogopite)-amphibole (K-richterite)-rutile-ilmenite-diopside (MARID) xenolith suite of Dawson and Smith, (1977). Moreover, C-SCLM often contain higher than expected proportion of clinopyroxene and garnet in addition to incompatible trace-element budgets than cannot be simply reconciled with partial melt extraction alone. The most widely accepted model suggests that MARID, garnet and pyroxene were introduced into the C-SCLM after melt extraction and depletion via metasomatism. Nonetheless, the origins of the metasomatic agents affecting the C-SCLM remain enigmatic. Several potential sources are postulated as fluids/melts released from within subducted slabs (e.g. Bell et al., 2005; Simon et al., 2007; Broadley et al., 2016; Wang et al., 2016) as well as low-degree alkaline carbonate-rich mafic silicate or 'carbonatitic' fluids/melts derived from within the asthenosphere (Yaxley et al., 1991; Rudnick et al., 1993; Grégoire et al., 2002; Grégoire et al., 2003; Aulbach et al., 2013; le Roex and Class, 2016).

Due to our lack of ability to directly sample rocks from mantle depths, much of the current understanding of the C-SCLM derives from the petrological and geochemical study of intra-continental magmas and their entrained C-SCLM xenoliths/xenocrysts. However, the complex history and extreme age of C-SCLM with potential for multiple metasomatic events with contrasting agents hinders our understanding of the evolution of the C-SCLM. A further complication arises from the concentration of intra-continental magmas within low shear-wave velocity zones at the margins of lithospheric blocks which implies that C-SCLM xenoliths are strongly biased toward metasomatised material (e.g. Griffin et al., 2009). The difficultly in unravelling and understanding

metasomatism in the C-SCLM is best exemplified by the lack of consensus on the origins of metasomatism in the Kaapvaal craton, perhaps the most complex but also the most constrained of all the Earth's cratons. Within the Kaapvaal both 'subduction' and 'plume' metasomatism has been proposed to explain the petrology, modal mineral abundances and geochemical compositions of the C-SCLM. It is therefore clear that a geochemical proxy for the discrimination of subduction and asthenospheric/plume metasomatism would offer considerable insights into the origins of metasomatism.

The overwhelming concentration of the halogen elements and in the Earth's surficial reservoirs and often unique distribution amongst the Earth's surficial reservoirs suggests that they might offer potential for the discrimination of metasomatic agents in the C-SCLM. Halogen ratios (e.g. F/Cl; Br/Cl; I/Cl) as well as the $^{35}Cl/^{37}Cl$ isotope system ($\delta^{37}Cl$), have already emerged as powerful tracers of recycled material into and within the Earth's convecting mantle (Barnes et al., 2008; Barnes et al., 2009; John et al., 2010; John et al., 2011; Kendrick et al., 2011; Kendrick et al., 2012; Kendrick et al., 2013; Chiaradia et al., 2014; Kendrick et al., 2014a; Kendrick et al., 2015; Halldórsson et al., 2016; Kendrick et al., 2017; Manzini et al., 2017). Unlike the convecting mantle, Earth's C-SCLM has been isolated from mantle convection since it stabilised more than 2.5 billion years ago. Subsequently, much of the Earth's C-SCLM has been subjected to metasomatism by volatile and halogen-bearing alkali fluids and melts, as evidenced by the chemical and mineralogical composition of mantle xenoliths entrained in ultramafic magmas (e.g. Giuliani et al., 2012) and diamond fluid inclusions (Johnson et al., 2000; Burgess et al., 2002; Tomlinson et al., 2006; Tomlinson et al., 2009). Most recently, the halogen elements have been shown to offer potential for the discrimination of metasomatic agents in the C-SCLM (Broadley et al., 2016). However, even with the progress made over the last decade towards constraining the distribution of these elements within the Earth's interior and their behaviour during subduction, our understanding of the cycling of the halogen elements within the Earth's interior and the ancient C-SCLM remains remarkably poorly constrained.

Primitive ultramafic UML are potassic-ultrapotassic, volatile- and alkaline-rich rocks derived from low-degree melting within the convecting mantle that subsequently interact with overlying variably enriched metasomatised C-SCLM (e.g. Tappe et al., 2004; Tappe et al., 2006; Tappe et al., 2008; Tappe et al., 2011). The nominal depletion of halogens in the Earth's convecting mantle suggest that such melts will be extremely sensitive to the addition of halogens from metasomatised C-SCLM domains. It follows

that the investigation of the halogen inventory of UML magmatism and their hosted C-SCLM xenoliths will offer significant potential in elucidating the metasomatic histories of the stable nuclei at the heart of the Earth's modern-day continents. Here, I provide the first combined elemental (F, Cl, Br) and isotopic ($\delta^{37}Cl$) investigation into the origin of metasomatism in C-SCLM along the southern margin of the North Atlantic Craton (NAC) of South Greenland, through the investigation of primitive UML.

Chapter 2.0: Literature review

2.1. Lamproite, kimberlite and UML

Ultramafic lamprophyre (UML), kimberlite and lamproite are varieties of intra-continental magmas that are some of the most extreme, low-degree melting products of the Earth's mantle derived from depths greater than any other igneous rock type. Typically, in terms of distribution they are most commonly confined to areas of cool over-thickened cratonic sub-continental lithospheric mantle (C-SCLM) and surrounding mobile belts as a result of their depth of melting, which is often in excess of 150km. Although relatively minor constituents of continental magmatism these rocks garner significant interest due to their hosting of diamonds and mantle xenoliths scavenged from the C-SCLM during their emplacement and eruption. Continental magmas and their xenolithic cargo provide a unique snapshot of the Earth's interior. And yet, in spite of the extensive interest shown in these exotic intra-plate magmas, their primary magma compositions, potential genetic associations and classification remain a subject of debate (Mitchell and Bergman, 1991; Rock, 1991; Mitchell, 1995; Tappe et al., 2005). Kimberlite, UML and lamproite are often macroscopically very similar, best explained by hypabyssal crystallization of volatile-rich magmas. These varieties of magmatism are typically exceptionally alkaline and display extremely high concentrations of mantle incompatible trace-elements as well as remarkably variable radiogenic isotope compositions. The similarities of UML, kimberlite and lamproite magmatism have often hampered their correct identification which has often led to both the tectonic significance and spatial associations of these magmas being overlooked.

2.1.1. Lamproite

Although derived from melting at a depth in excess of 100 km, lamproite magmas are not confined to ancient cratons and surrounding regions but also areas of exceptionally thick SCLM in non-cratonic orogenic regions. In cratonic regions (e.g. the North Atlantic Craton of Canada and Greenland) lamproite appears within close proximity to the margins of the Archaean cratons and Palaeoproterozoic mobile belts overlying fossil collision zones where former subduction was likely to have been active in the past and in areas that have experienced multiple phases of orogeny and/or aborted rifting (e.g. Mitchell and Bergman, 1991). Within Europe, Cenozoic orogenic lamproites are emplaced along the Mediterranean Rim and display close association in

both space and time with orogenic belts and regions of continental collision, with rocks being emplaced within 30 Ma of the cessation of subduction-related magmatism during periods of extensional rebound (Mitchell and Bergman, 1991). Compositionally, lamproites are comparatively H_2O-rich and CO_2-poor in addition to exhibiting well-developed high-field strength element (HFSE) anomalies and high large-ion lithophile element (LILE) concentrations. Such characteristics coupled with the common spatial relationship of lamproites with fossil subduction and continental suture zones, could imply that subduction processes play a key role in their formation. Such an interpretation is corroborated by the striking similarities in the distribution of incompatible elements within Cenozoic lamproites to preceding subduction magmatism in the Mediterranean Rim (e.g. Prelević et al., 2008).

The high K_2O contents of lamproite magmatism require a K-rich phase in their genesis, with phlogopite or K-richterite likely candidates on account of their stability at P/T conditions prevailing in the deep mantle (e.g. Sudo and Tatsumi, 1990; Konzett et al., 1997). Lamproite magmas display some of the most enriched and extreme radiogenic isotope compositions recorded; requiring enrichment and subsequent isolation of their source from the depleted convecting upper mantle (DMM) as sampled by MORB (mid-ocean ridge basalt) over billion-year timescales. The prevailing theory dictates that lamproite must sample long-term isolated preconditioned and metasomatised C-SCLM (e.g. MARID) or convecting mantle reservoirs (e.g. deeply subducted sediments) that are capable of remaining unperturbed long after delivery into the mantle through subduction recycling (e.g. Foley, 1992; Murphy et al., 2002; Davies et al., 2006).

2.1.2. Kimberlite

Kimberlite in contrast to lamproite are nearly totally restricted to C-SCLM areas emplaced within lithospheric keels of depths in excess of 150 km and are the primary source of diamonds on Earth. Primary or parental melt compositions of kimberlite and the effect of interaction with and/or assimilation of C-SCLM during their emplacement remains contentious. A relatively early recognition and classification of two mineralogically distinct varieties of kimberlite (i.e. micaceous and basaltic) with near-identical eruptive styles, was verified by the measurement of their diverging Pb-Sr-Nd radiogenic isotope compositions (Smith, 1983). This led to a sub-division of kimberlite into Group 1 (G1): kimberlite with initial radiogenic isotopes compositions that are

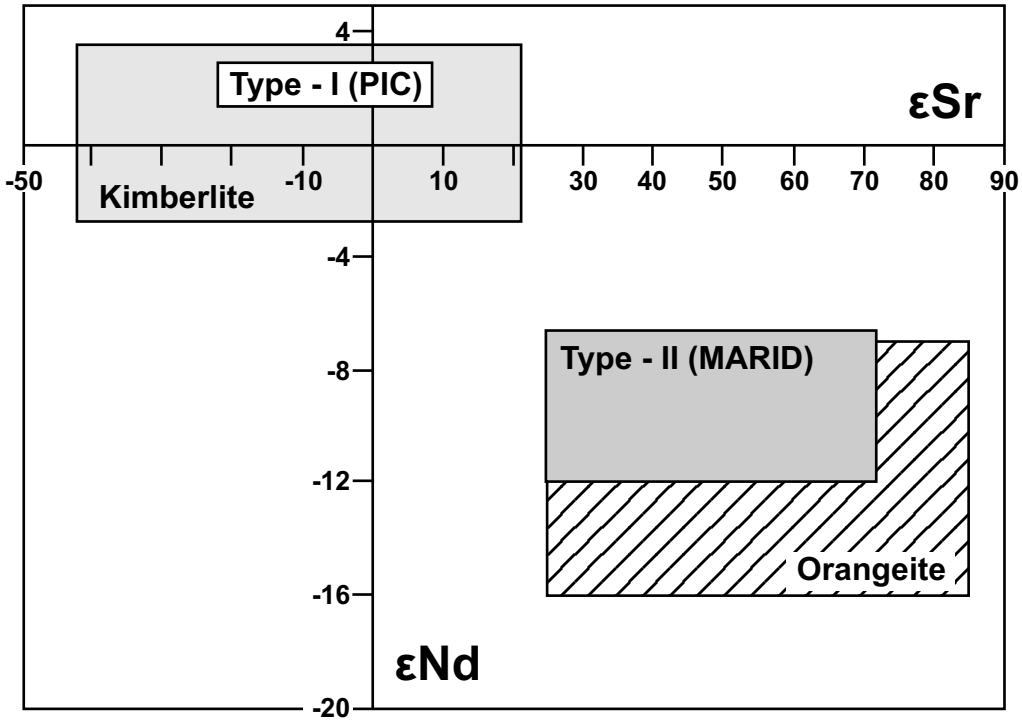

Figure 1: εSr vs εNd for Type-I and Type-II clinopyroxene as well as whole-rock data for kimberlite and orangeite, modified from Grégoire et al., (2002).

comparable with that of an OIB (ocean island basalt)-type source in equilibrium with the convecting mantle and, Group 2 (G2): kimberlite that display ancient and extremely enriched radiogenic isotope compositions. It was subsequently argued that G1 and G2 kimberlites are sufficiently distinct that G2 kimberlites should be termed 'orangeite' (Mitchell and Bergman, 1991) after Wagner, (1928) and that orangeite share greater similarities with lamproite (Mitchell, 1995). Kimberlite (G1) *senso stricto* are CO_2-rich melts that erupt through refractory cratonic lithosphere that display a limited spatial relationship with rifted lithosphere; a fact unlikely to be coincidental on account of the concentration of kimberlite occurrences in the very stable centre nuclei of the Earth's continents. The high MgO, NiO and CO_2 content are best explained through low-degree partial melting of an olivine-rich carbonated peridotite with a depleted Sr-Nd-Pb isotopic character reminiscent of convecting upper mantle. Kimberlite occurrences have been shown to display a temporal link with hotspot tracks (e.g. Heaman and Kjarsgaard, 2000; Heaman et al., 2004), suggesting an OIB-like affinity as supported by the characteristic OIB trace-element ratios (e.g. Nb/U, Ce/Pb; Hofmann, 1988).

Metasomatism of C-SCLM during emplacement of kimberlite has been suggested to form a similar type petrological assemblage to that of MARID termed phlogopite-ilmenite-clinopyroxene or PIC (Grégoire et al., 2002) by reason of similar radiogenic isotopic composition of these phases to convective upper mantle, while orangeite magmatism has been argued to both derive from or generate MARID assemblages (Figure. 1). On the one hand it has been argued that orangeites, similar to anorogenic lamproite derive from low-degree melting of veined MARID assemblages (e.g. Foley, 1992; Mitchell, 2006; Giuliani et al., 2015), while in contrast several workers advocate that orangeite magmatism generates MARID xenolith assemblages (e.g. Konzett et al., 1998; Grégoire et al., 2002). The lack of a consensus into the origins of the MARID xenolith suite and its relationship with orangeite magmatism illustrate the complexities in understanding metasomatism of the Earth's ancient C-SCLM and the potential influence of these metasomes on continental intraplate magmatism.

2.1.3. Ultramafic lamprophyre (UML)

Of all varieties of intra-plate continental alkaline magmatism, the classification of UML has traditionally been the most problematic. Their macroscopic similarities to lamproite and particularly kimberlite as well as the proliferation of increasingly complex nomenclature has often resulted in poor classification. Prior to the IUGS

classification scheme of Le Maitre et al., (2002) updated by Tappe et al., (2005), UML were often simply regarded as varieties of kimberlite, or even 'micaceous' kimberlite (e.g Emeleus and Andrews, 1975) despite bearing limited similarity to orangeite. The failure to recognize this suite of alkaline ultramafic magmatism has meant that the significance of the close spatial relationship of UML with carbonatite on craton and surrounding mobile belts undergoing continental extension is often overlooked. Similar to kimberlite, the high MgO, NiO and CO_2 contents must be explained as a result of low-degree partial melting of an olivine-rich carbonated peridotite within the convecting mantle. However, as with lamproite, UML require an essential melt contribution from a K-bearing phase. The similarities of UML and kimberlite magmatism and unique tectonic controls, suggest origins from a similar asthenospheric carbonated silicate melt that interacts with cold variably enriched overlying cratonic lithosphere generating hybrid magmas that diverge in composition as a function of the degree of C-SCLM enrichment (e.g. Tappe et al., 2006; Tappe et al., 2008; Tappe et al., 2012).

On a conceptual basis lamproite and kimberlite can be considered to represent 'end-member' magmas derived from melting of solely metasomatic C-SCLM or deeply subducted recycled reservoirs and carbonated asthenospheric peridotite respectively. UML form as complex, hybrid mixtures of both. In such a scenario, the origins and agents of metasomatism in the C-SCLM play a fundamental role in the generation and characteristics of UML magmatism. Therefore, the investigation of UML themselves might offer considerable insight into deciphering the nature of metasomatism and the evolution of the Earth's ancient C-SCLM.

2.2. The halogens elements: Novel tracers of mantle metasomatism?

2.2.1. Distribution of the halogen elements on Earth

The halogens are a group of elements within the periodic table designated as group 17 according to modern IUPAC nomenclature. This group comprises the elements in order of increasing atomic and ionic radii; fluorine (F), chlorine (Cl), bromine (Br), iodine (I) and astatine (At). The halogens, as with all volatile and incompatible elements on Earth, are nominally concentrated in the Earth's differentiated crust, terrestrial fluids, serpentinized oceanic mantle, sediments and hydrosphere. As a result of halogens are nominally depleted in the convecting mantle (Table. 1). On Earth, Cl and Br are most abundant of the halogens respectively, either in aqueous solution within the oceans

owing to high halide salt solubility, or in evaporite deposits (Eggenkamp, 2014). F is next most abundant, primarily hosted in fluoride-rich minerals within the crust (as a result of alkali-metal fluoride insolubility) such as; fluorite (CaF_2), fluoroapatite [$Ca_5(PO_4)_3F$] and more rarely cryolite (Na_3AlF_6). I has a low concentration in both minerals and seawater; but due to biogenic assimilation into organic matter, is concentrated in organic-rich marine sediments and is concentrated up to 45 p.p.m. in serpentinized oceanic lithosphere (Kendrick et al., 2013) At has no stable natural or synthetic isotopes. The longest lived of its 32 known radioisotopes ^{210}At, has a half-life of just 8.1-8.3hrs. At is one of the rarest naturally occurring elements on Earth with a maximum of just ~ 30g expected to exist in the Earth's crust at any one time (Wilbur, 2013) and hence won't be discussed here further.

The planetary abundance of halogens in the bulk-silicate Earth (BSE) relative to similarly volatile elements has proved difficult to estimate. This results from the scarcity of chondritic material used as a reference frame for the accretion of the solar systems inner planets and the lack of precision of analytical techniques used for measurement of the heavy halogens (Cl, Br and I). Estimated BSE halogen concentrations fall in the ranges 8 – 44 p.p.m. Cl, 0.045 – 0.4 p.p.m. Br and 0.007 – 0.04 p.p.m. I (Ringwood, 1962; Allen and Reed, 1965; Morgan and Anders, 1980; Sun, 1982; Anderson, 1983; Jambon et al., 1985; Kargel and Lewis, 1993; McDonough and Sun, 1995; Allègre et al., 2001; McDonough, 2003; Lyubetskaya and Korenaga, 2007; Burgess et al., 2009; Kendrick et al., 2017). The variation of BSE estimates of the halogens up to an order of magnitude is not unexpected given the trace concentrations of halogens and the lack of reliable data available, particularly for Br and I (Clay et al., 2017).

It has generally been accepted that the heavy halogens in the BSE are depleted relative to similarly volatile lithophile elements (e.g. Allègre et al., 1995). The depletion of heavy halogens in the BSE has been variably ascribed to; hydrodynamic escape (Kramers, 2003), sequestration of halogens into the Earth's core (Armytage et al., 2013) or impact driven collisional erosion of halogens from the early Earth (Sharp and Draper, 2013). However, recent high-precision halogen data obtained via neutron-irradiation noble gas mass spectrometry (NI-NGMS) across all meteorite classes show that the heavy halogens are not depleted relative to similarly volatile lithophile elements (Clay et al., 2017).

Table 1: Estimated halogen abundances in the Earth

Reservoir	Mass (kg)	F (ppm)	Cl (ppm)	Br (ppb)
Seawater	1.4×10^{21}	1.3 ± 0.07	19,000 ± 970	66,000 ± 3,300
Evaporites	3.0×10^{19}	10 ± 10	550,000 ± 100,000	150,000 ± 100,000
Marine sediments	5.0×10^{20}	1,000 ± 300	40,000 ± 20,000	40,000 ± 20,000
Sedimentary rocks	1.5×10^{21}	550 ± 100	700 ± 400	4,000 ± 3,000
Crustal brines	6.0×10^{19}	20 ± 15	100,000 ± 50,000	600,000 ± 400,000
Continental + oceanic crust	2.6×10^{22}	550 ± 100	300 ± 100	600 ± 250
Convecting mantle	2.8×10^{24}	12 ± 2	5 ± 2	13 ± 6
Primitive mantle	4.0×10^{24}	17 ± 6	26 ± 8	76 ± 25

Reservoir	Mass (%)	F (%)	Cl (%)	Br (%)
Seawater	0.03	~ 0	37 ± 5	44 ± 8
Evaporites	0.001	~ 0	22 ± 5	2 ± 2
Marine sediments	0.01	1.1 ± 0.4	3 ± 2	9 ± 5
Sedimentary rocks	0.04	1.7 ± 0.5	1 ± 1	3 ± 2
Crustal brines	0.001	~ 0	8 ± 6	17 ± 15
Continental + oceanic crust	0.6	30 ± 8	11 ± 4	7 ± 3
Convecting mantle	70 ± 20	67 ± 17	18 ± 8	4 ± 3
Primitive mantle	100	100	100	100

Estimates of halogen concentrations in different surface and mantle reservoirs from various sources modified from Kendrick et al., (2017 and references therein), convecting mantle includes both mid-ocean ridge basalt (MORB) and ocean-island basalt (OIB) sources

Table 1: *continued*

Reservoir	Mass (kg)	F (kg)	Cl (kg)	Br (kg)
Seawater	1.4×10^{21}	$(1.8 \pm 0.1) \times 10^{15}$	$(2.7 \pm 0.1) \times 10^{19}$	$(9.2 \pm 0.5) \times 10^{16}$
Evaporites	3.0×10^{19}	$(3.0 \pm 3.0) \times 10^{14}$	$(1.7 \pm 0.3) \times 10^{19}$	$(4.5 \pm 3.1) \times 10^{15}$
Marine sediments	5.0×10^{20}	$(5.0 \pm 1.8) \times 10^{17}$	$(2.0 \pm 1.6) \times 10^{18}$	$(2.0 \pm 1.1) \times 10^{16}$
Sedimentary rocks	1.5×10^{21}	$(8.3 \pm 2.2) \times 10^{17}$	$(1.1 \pm 0.6) \times 10^{18}$	$(6.0 \pm 4.7) \times 10^{15}$
Crustal brines	6.0×10^{19}	$(1.2 \pm 1.1) \times 10^{15}$	$(6.0 \pm 4.2) \times 10^{18}$	$(3.6 \pm 3.0) \times 10^{16}$
Continental + oceanic crust	2.6×10^{22}	$(1.4 \pm 0.3) \times 10^{19}$	$(7.8 \pm 2.8) \times 10^{18}$	$(1.6 \pm 0.7) \times 10^{16}$
Convecting mantle	2.8×10^{24}	$(3.2 \pm 0.7) \times 10^{19}$	$(1.3 \pm 0.6) \times 10^{19}$	$(3.8 \pm 1.6) \times 10^{16}$
Primitive mantle	4.0×10^{24}	$(4.8 \pm 0.7) \times 10^{19}$	$(7.4 \pm 0.9) \times 10^{19}$	$(2.1 \pm 0.4) \times 10^{17}$

2.2.2. Chemical behaviour of the halogen elements

Atomically, the halogen elements are characterised as missing an electron from a complete valence shell. As a result of this electron configuration, all the halogens display marked electronegativity, which decreases with increasing size of ionic radii (Aiuppa et al., 2009). The increase in atomic radii from one halogen to the next heaviest in the group is observed as an almost perfect doubling of atomic mass, which accompanies an increase in specific gravity and melting/boiling points as well as a decrease in reactivity and solubility; making fluorine the most reactive halogen in magmatic systems. In terms of fluid solubility - F non-withstanding, the halogens are remarkably fluid mobile, with the heavy halogens (Cl, Br and I) strongly partitioning into fluid over a melt phases (Bureau et al., 2000; Straub and Layne, 2003). F has one of the highest electronegativity's of any element and one of the smallest ionic radii of any anion, making it extremely reactive in natural systems (Auippa et al. 2009).

Within silicate melts the larger ionic radii of Cl, Br and I relative to F and their interactions with crystal structure implies that they behave highly incompatibly compared to the moderate incompatibility of F during partial melting of the mantle. The incompatibility contrast of F from Cl, Br and I results from the similar ionic radii of the F^- fluoride ion to that of the OH^- hydroxyl group (Shannon, 1976). F is known to substitute readily for OH^- in volatile-bearing accessory mineral phases commonly found in metasomatically altered mantle assemblages (e.g. Smith et al., 1981); i.e. phlogopite, amphibole, clinohumite and apatite, as well as within nominally anhydrous minerals (NAM) ubiquitous in the mantle, such as: olivine, orthopyroxene, clinopyroxene and garnet, albeit in far lower concentrations (Beyer et al., 2012; Joachim et al., 2014). It is now generally suggested that NAM might represent the only significant F reservoir by volume within the mantle negating volumetrically insignificant metasomes rich in phlogopite, amphibole and apatite (e.g. Beyer et al., 2012; Crépisson et al., 2014; Joachim et al., 2014). The expectation is that F^- behaves in NAM in much the same manner as it does within hydrous minerals in being only moderately incompatible during partial melting (Pyle and Mather, 2009). Consequently, F can be effectively decoupled from Cl, Br and I during mantle fractionation processes (i.e. fractional crystallisation; partial melting etc.). Chlorine is less compatible than fluorine (Beyer et al., 2012; Dalou et al., 2014) as well as having lower potential for substitution with OH^- (John et al. 2011). The larger ionic radii of bromine and iodine do not appear to allow for direct substitution of OH^- in silicate crystal structure and are yet more incompatible

than Cl on account of larger ionic radii (Aiuppa et al., 2009). In contrast, Br and I are instead considered to coordinate with LILE within silicate crystal structure.

2.2.3. Halogens as a tracer for volatile recycling in the mantle

The Earth's uppermost hydrated oceanic mantle, differentiated crust, terrestrial fluids, sediments and hydrosphere are halogen reservoirs that have characteristic elemental halogen compositions that are conventionally described in terms of halogen ratios (e.g. F/Cl, Br/Cl, I/Cl). The subduction of hydrous minerals in altered oceanic slab lithologies (e.g. apatite, chlorite, lawsonite, epidote, paragonite, amphibole, phengite, talc, lizardite-chrysotile-antigorite), subducted sediments and pore fluids are considered to be significant in the subduction of halogens (Kendrick et al., 2011). However, Br/Cl and I/Cl ratios measured in both OIB and MORB are remarkably similar (Figure. 2; 3). The constancy of these ratios and observed lack of fractionation is interpreted to be a result of their similar bulk partition coefficients during melting. The constancy of I/Cl and Br/Cl ratios in the Earth's mantle might also imply that the subduction of I and Br enriched reservoirs (e.g. marine sediments and seafloor serpentinite) are either balanced by altered oceanic crust (ACC) with far-lower I/Cl and Br/Cl ratios or that Br and I are lost preferentially during subduction relative to Cl or F (e.g. Kendrick et al., 2014). A combination of both of the above appears likely on account of the preferential subduction of Cl in serpentinites relative to Br or I evidenced by Br/Cl and I/Cl ratios in melt inclusions that decrease across an arc, from maximum values in the forearc to compositions similar to MORB or lower in the backarc; (Kendrick et al. 2011; John et al. 2011) and the lower than MORB Br/Cl ratios observed in ACC (Chavrit et al., 2016). Across-arc variation in halogen concentrations in melt inclusions have been argued to suggest that Br and I are limited to cycling within the upper mantle with the subduction zone effectively behaving as a 'filter'(Kendrick et al., 2015). The fate of Cl in subduction is less clear, insofar that it appears to devolatilize from the subducting plate with less efficiency and thus is retained to greater depths than either Br or I (Kendrick et al. 2011; John et al. 2011; Kendrick et al. 2014a; Chavrit et al., 2016).

Of all the halogens F appears to devolatilize from the subducting slab with the least efficiency, on account of its moderate incompatibility and incorporation in deeply subducted hydrous mineral phases (e.g. phengite, apatite, phlogopite, K-richterite) and greater potential for retention in anhydrous metamorphic phases beyond slab

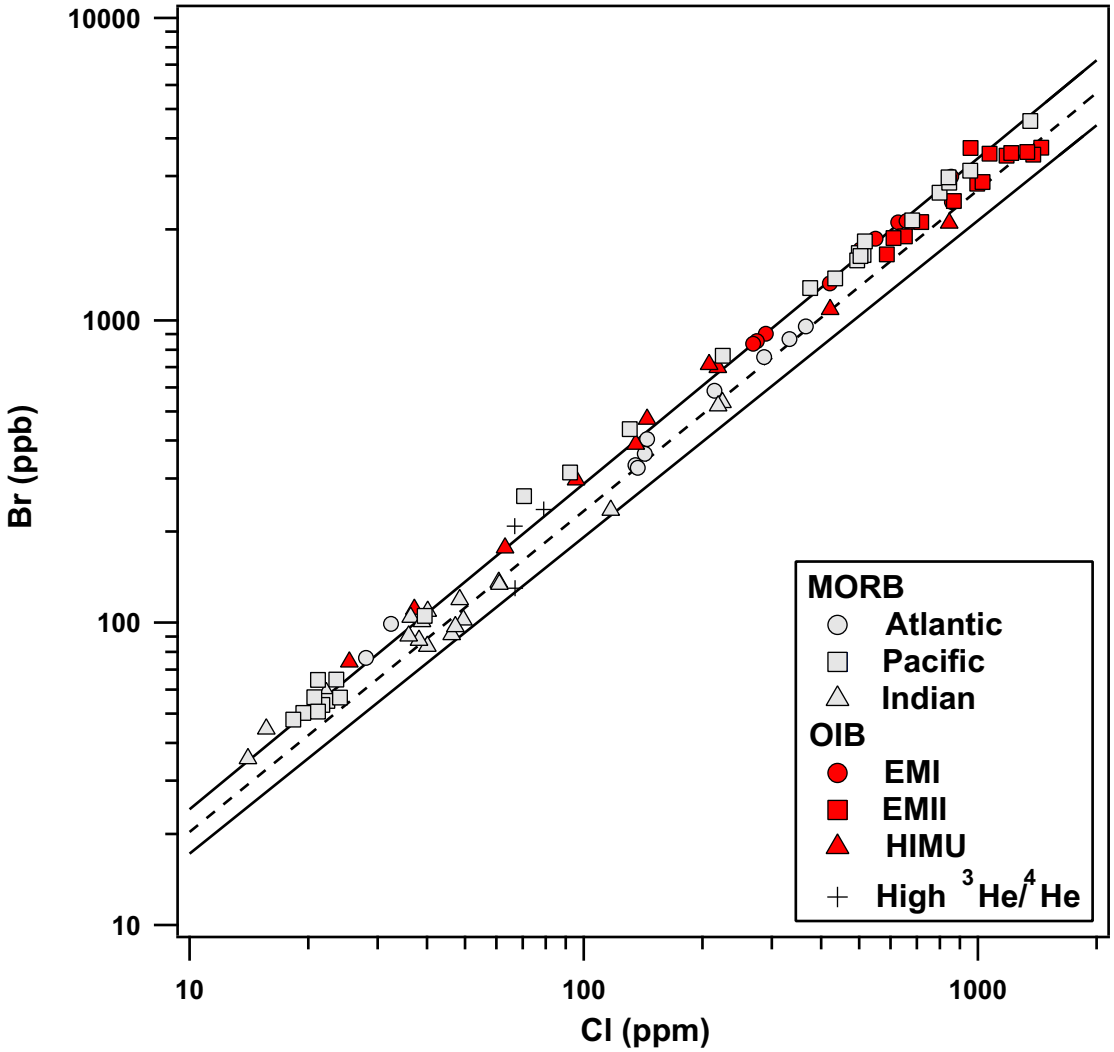

Figure 2: Br (ppb) vs Cl (ppm) for mantle melts from glasses in MORB and OIB from the Atlantic, Pacific and Indian Oceans and High $^{3}He/^{4}He$ from Baffin Bay, Canada. Data taken from Kendrick et al., (2017 and references therein).

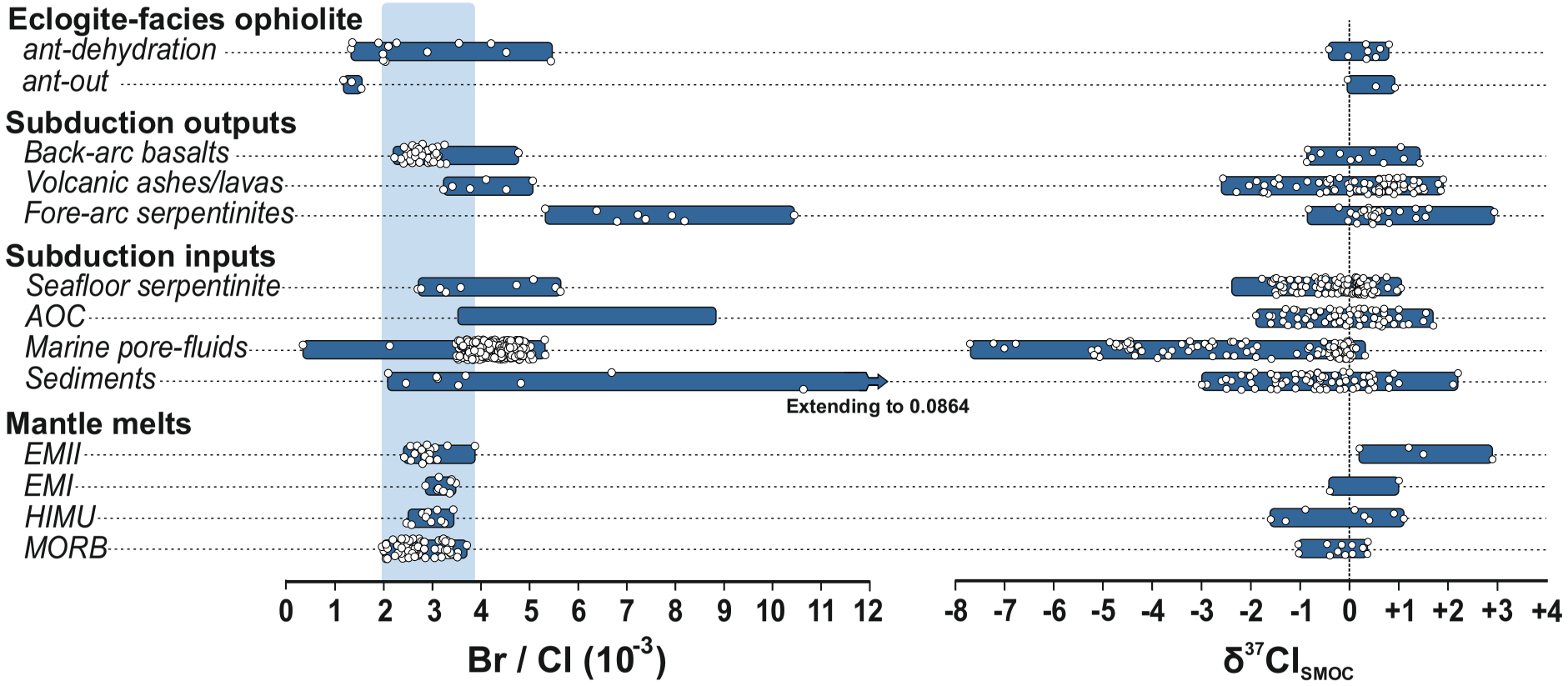

Figure 3: Compilation of reported Br/Cl and $\delta^{37}Cl$ for mantle melts, subduction inputs, subdcution outputs, and eclogite-facies ophiolites. Data reported for mantle melts (Kendrick et al., 2017 and references therein), subduction inputs (Muramatsu et al., 2007; John et al., 2011; Kendrick et al., 2013; Chavrit et al., 2016; Li et al., 2017), subduction outputs (John et al., 2011; Kendrick et al., 2013; Kendrick et al., 2014) and eclogite-facies ophiolite (John et al., 2011). Data for $\delta^{37}Cl$ [‰ versus standard marine ocean chloride (SMOC)] (Barnes et al., 2017 and references therein).

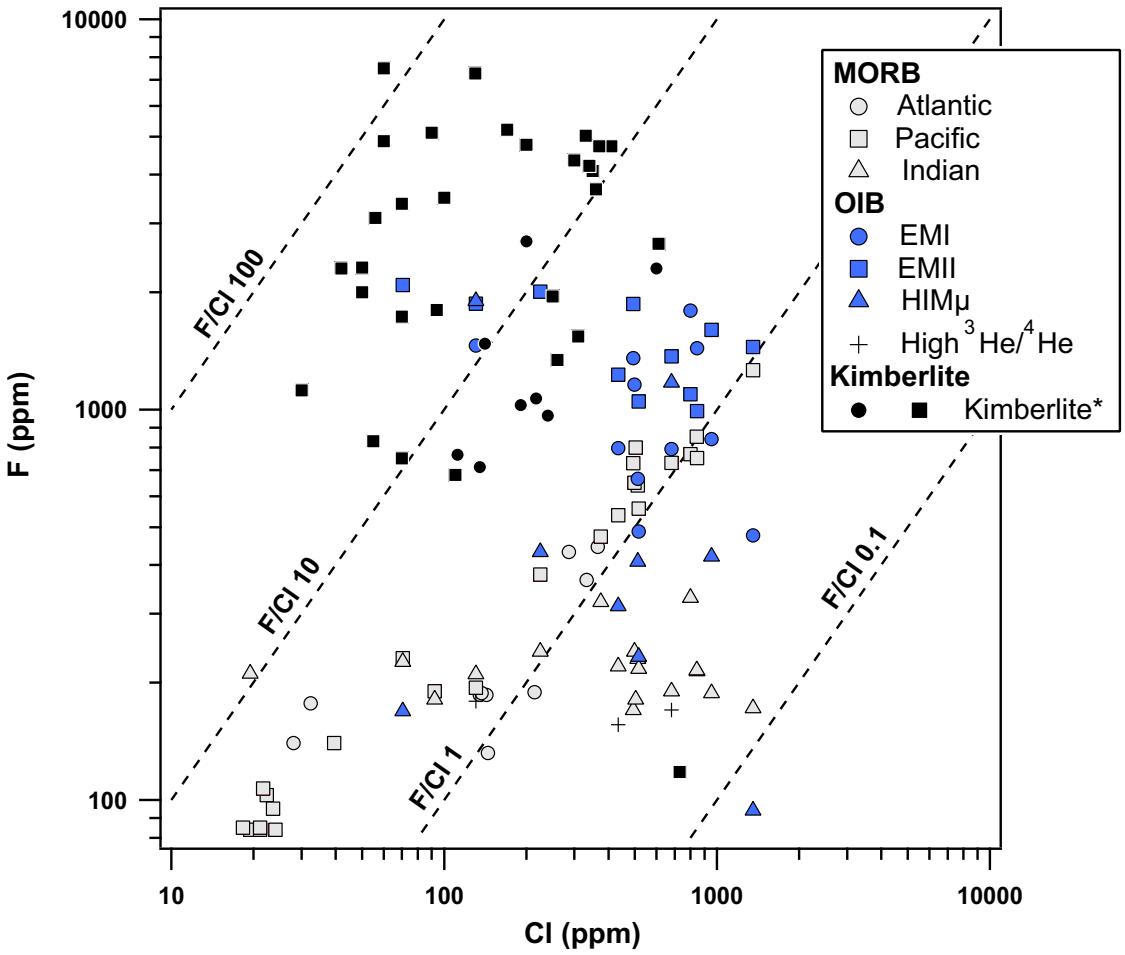

Figure 4: F vs Cl data for Atlantic, Pacific and Indian ocean MORB and Enriched Mantle-I (EM-I), Enriched Mantle (EM-II), HIMμ and Kimberlite. F and Cl data for MORB, OIB (Kendrick et al., 2017) and Kimberlite (Paul et al., 1976; Kjarsgaard et al., 2009). *Kimberlite data from Paul et al., (1976) was obtained through spectrophotometry is shown in filled squares.

dehydration (e.g. olivine). Furthermore, recent experimental work investigating F solubility in wadsleyite and ringwoodite suggests that F behaves in a similar manner to water at temperatures and pressures representative of the mantle transition zone; with wadsleyite and ringwoodite potentially incorporating as much as 665-1045 p.p.m. and 186-1235 p.p.m. F structurally, respectively (Roberge et al., 2015). F storage in the transition zone has wider implications for previous estimates of F concentrations of the mantle that assume fluorine to be largely homogenised within the whole mantle (e.g. McDonough and Sun, 1995). A possible high-F reservoir in the mantle is also tentatively supported by F and Cl data reported for kimberlite (Paul et al., 1976; Aoki et al., 1981; Kjarsgaard et al., 2009). Since kimberlite derive from very low degrees of melting (< 1.0%) in the convecting mantle it would be expected that F/Cl ratios of kimberlite would be lower than MORB based on the relative compatibilities of F and Cl. However, reported F concentrations and F/Cl ratios of kimberlite are often significantly higher than MORB (Figure. 4). This implies that kimberlite tap a uniquely enriched reservoir of F that is not sampled by MORB, either through interaction with F-enriched reservoirs within the C-SCLM, transition zone or EM-type OIB. A primitive F enriched reservoir seems unlikely on account of the low F/Cl observed in high ^{3}He / ^{4}He OIB (albeit from limited analyses) from Baffin Island and Samoa (Figure. 4).

2.2.4. Cl isotopes as a tracer of volatile recycling in the mantle

The Cl isotope composition of the Earths near-surface terrestrial reservoirs and crustal-derived fluids, as with elemental halogen ratios, display significant variation (Figure. 3) as a result of low-temperature fractionation processes near the Earth's surface (Barnes and Sharp, 2017 and references therein). The $\delta^{37}Cl$ composition of the Earth's depleted upper mantle sampled by MORB is largely homogeneous [-0.2 ± 0.5‰ relative to standard marine ocean chloride (SMOC) of 0‰], similar to the chlorine isotope composition of the bulk-Earth, carbonaceous chondrites and halite entrained within kimberlite from Udachnaya-East kimberlite field (Sharp et al., 2007; Sharp et al., 2013). However, debate surrounds the origin of Cl in the Udachnaya-East kimberlites and it should be stated the potential crustal contamination of Udachnaya (e.g. Kopylova et al., 2013; Kopylova et al., 2016) could render its $\delta^{37}Cl$ composition unreliable. Sediments covering a wide range of ages from the Archaen and Proterozoic eras through to the Jurassic period are also similar to MORB averaging 0.0 ± 0.3‰, albeit spanning a greater range, that displays no secular variation in Cl isotope composition

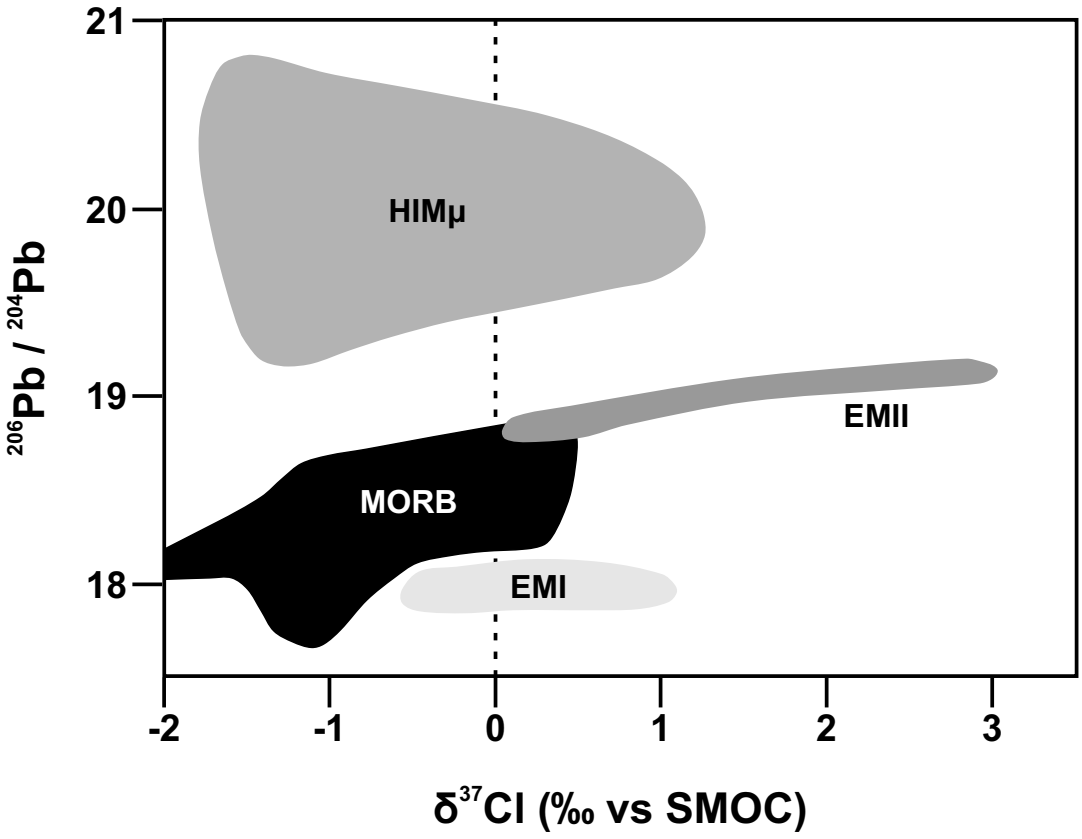

Figure 5: $^{206}Pb/^{204}Pb$ vs $\delta^{37}Cl$ from Icelandic sub-aerial glasses modified from Halldórsson et al., (2016). $\delta^{37}Cl$ data for MORB (Sharp et al., 2007; Boniefacie et al., 2008), Enriched Mantle-I (EM-I) and Enriched Mantle-II (EM-II) and HIMμ (John et al., 2010). $^{206}Pb/^{204}Pb$ data from PetDB database (www.earthchem.org/petdb).

with age (Sharp et al., 2007). These similarities in $\delta^{37}Cl$ composition between crustal and mantle reservoirs implies that the Earth's crust and mantle formed from a complementary and homogenous reservoir with respect to $\delta^{37}Cl$ composition and that a primordial $\delta^{37}Cl$ reservoir distinct from that of solar nebula is unlikely to exist within the Earth. Nonetheless, significant heterogeneity is demonstrated in melt inclusions recovered from OIB magmatism which are shown to sample recycled material (John et al., 2010). Empirical observations of exhumed metamorphic rocks (e.g. John et al., 2011; Selverstone and Sharp, 2015) and theoretical calculations (Schauble et al., 2003) indicate that Cl isotope fractionation is not significant in Cl-bearing phases at high temperatures. Accordingly, the $\delta^{37}Cl$ of individual subduction inputs is preserved during recycling and therefore $\delta^{37}Cl$ can identify the presence of recycled Cl in OIB source regions (Figures. 3 and 5; John et al., 2010; Halldórsson et al., 2016). Given the low concentration of Cl in the mantle, Cl inputs from recycling represent a significant contribution to the mantle chlorine budget making $\delta^{37}Cl$ a remarkably sensitive indicator of even relatively small contributions of recycled material to mantle rocks (John et al., 2010).

Chapter 3.0: Selected samples and sample petrology

3.1. Geological setting

Western and Southern Greenland has been repeatedly subjected to volatile-rich alkaline magmatism, including occurrences of kimberlite, lamprophyre, carbonatite and lamproite over a time span of over 2500 Ma; one of the longest time spans known for such magamatism on Earth (e.g. Larsen and Rex, 1992; Larsen et al., 2009). Alkaline magmatism of Greenland is generally related to major geo-tectonic events; continental collision at ~1800 Ma and subsequent rifting, failed continental rifting in the Gardar period ~1100-1300 Ma and continental rifting followed by the breakup of Rhodinia at ~600 Ma and the opening of the Iapetus Ocean. Rifting at ~150 Ma within the Jurassic in the NAC corresponds to incipient stretching of the lithosphere resulting in the opening of the Labrador Sea and the splitting of the NAC into Canadian and Greenlandic sections in addition to the splitting of the Ketilidian Mobile Belt (with the Canadian section termed the Makkovik Belt; Figure. 6).

The tectonic framework of Western and Southern Greenland (Figure. 6) comprises an Archaean craton which has remained stable since c. 2500 Ma (Chadwick and Garde, 1996; Garde et al., 2002) bounded to the north and south by Palaeoproterozoic mobile belts (Larsen and Rex, 1992). Beyond the southern margin of the NAC lies the Ketilidian mobile belt formed around ~ 1.8 Ga with the accretion of new material to the margin in response to oblique convergence of southern Greenland and the subduction of an oceanic plate from the south (Chadwick and Garde, 1996), which is considered one of several contemporaneous orogenic belts in the North Atlantic Craton (NAC) (Van Kranendonk et al., 1993; Park, 1994; Park, 1995; Garde et al., 2002). Beyond the northern margin of the NAC lies initially the Nagssugtoqidian mobile belt and further north the Rinkian mobile belt. These mobile belts are thought to have formed mainly by the reworking of Archaean crust accreted to the craton through continental collision c. 1850 Ma (Larsen and Rex, 1992).

C-SCLM xenoliths recovered from the Northern boundary of the NAC yield Re-Os T_{RD}^{erupt} model ages of between 3.2 and 2.8 Ga (Wittig et al., 2010); a model age common to a number of other cratons worldwide (e.g. Pearson et al., 1995a; Pearson et al., 1995b; Irvine et al., 2003). 3.2 – 2.8 Ga model ages for the C-SCLM of the NAC are

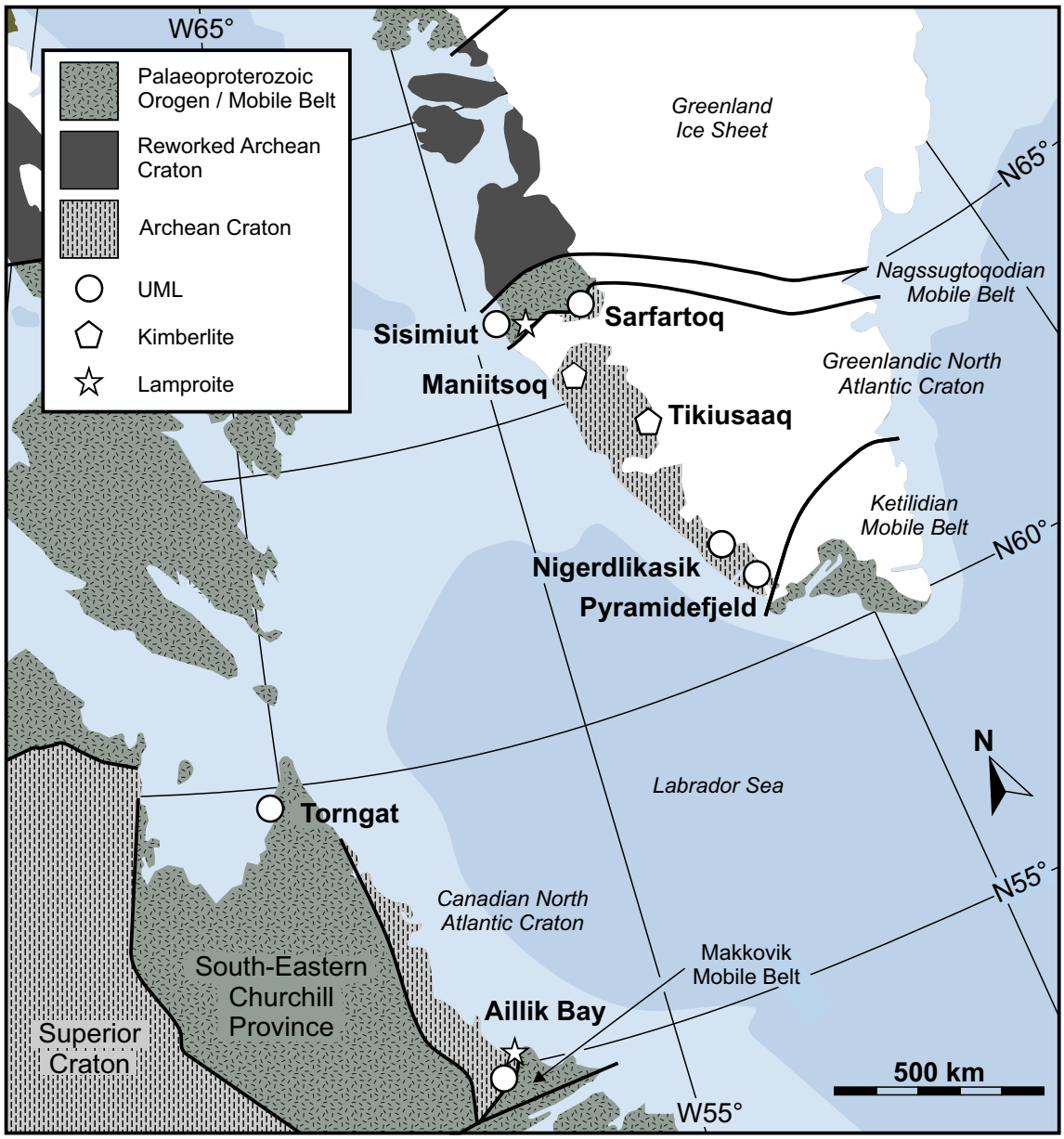

Figure 6: A simplified geological map of the North Atlantic Craton modified from Wardle and Hall, (2002) displaying UML, kimberlite and lamproite localities from (Nelson, 1989; Tappe et al., 2004; Tappe et al., 2006; Tappe et al., 2007; Nielsen et al., 2009; Tappe et al., 2009; Tappe et al., 2011).

coupled with U-Pb zircon ages of overlying on-craton TTG and granite crust which exhibits a strong age mode between 3.1 and 2.9 Ga (Wittig et al., 2010). Taken together, the above data suggests that the main phase of lithospheric formation in the NAC took place between 3.2 and 2.8 Ga (Wittig et al., 2010).

In contrast, PGE isotope systematics of mantle peridotites from the southern boundary of the NAC at Pyramidefjeld and Nigerdlikasik are distinctly enriched in PGE abundances accompanied by higher radiogenic Os systematics that yield T_{RD}^{erupt} model ages that are largely Palaeoproterozoic in age (Wittig et al., 2010). The enriched PGE and Os isotope signature of the C-SCLM underlying Nigerdlikasik and Pyramidefjeld has been inferred to result from substantial metasomatic alteration of their PGE budgets as a result of the formation of the Ketilidian mobile-belt and subduction of an oceanic plate from the south (Wittig et al., 2010). Subduction metasomatism of the C-SCLM along the southern boundary of the NAC is supported by trace element systematics of Gardar period (~1.2 Ga) magmatism (e.g. Goodenough et al., 2002). Rift induced basaltic magmatism of the Gardar province emplaced within the Ketilidian mobile belt and NAC are considered to derive from large-scale decompression melting of SCLM. Gardar magmas display a pronounced HFSE anomaly as well as LREE-enrichment and high Ce/Pb and La/Nb ratios (Goodenough et al., 2002). Such geochemical characteristics are similar to subduction-related basalts of the Basin and Range Province (Fitton, 1995) and lamproite from Aillik Bay (Tappe et al., 2007). The similarities of Gardar period basalts to melts formed via subduction processes suggest that the Gardar basalts derive from the melting of pre-conditioned subduction metasomatised C-SCLM of the NAC and adjacent Ketilidian SCLM (Goodenough et al., 2002). It is also acknowledged that halogens were an important components of Gardar magmas evidenced by the extraordinary F concentration at Ivigtut and its associated cryolite deposit (25 km SSW from Pyramidefjeld). The Ilímaussaq intrusion also displays considerable halogen contents (e.g. Larsen and Sørensen, 1987). As with the geochemical characteritics of Gardar magmas, the extreme concentrations of halogens along the southern margin of the NAC and the Ketilidian mobile belt has been ascribed to sampling of a subduction enriched SCLM associated with the Ketilidian orogeny (Köhler et al., 2009).

3.2. Selected samples

This study investigates two UML samples from Nigerdlikasik and Pyramidefjeld (part of the Trinity College Dublin, Department of Geology collection) and their hosted C-SCLM xenoliths. Both UML were emplaced within Archaean basement of the North Atlantic Craton at Nigerdlikasik and Pyramidefjeld, South Greenland, and are located between the southern margin of the NAC and the Palaeoproterozoic Ketilidian mobile belt and the Tikiusaaq kimberlite-carbonatite complex (Figure. 6). UML emplaced at Nigerlikasik and Pyramidefjeld had previously been termed massive mica-rich kimberlites (e.g. Emeleus and Andrews, 1975) but have been reclassified by Tappe (2005) as part of their updated IUGS classification of igneous rocks. Further geochemical evidence and discussion of this classification is presented in *Chapter 6.2*. For a detailed description of the local structural aspects and mapping of emplacements the reader is referred to (Andrews and Emeleus, 1975), although a brief overview from the publication is provided here. UML at Nigerdlikasik (T.C.D. sample P3580) comprises an isolated narrow dyke of near-constant thickness (~ 0.5m) that occasionally breaks into two separate parallel sheets; possibly indicative of two separate phases of intrusion, emplaced into Archaean basement. UML (T.C.D. sample P3581) at Pyramidefjeld are emplaced as three distinct interconnected sheets occupying parts of the Palaeoproterozoic Pyramidefjeld granite complex extending into the surrounding Archaean gneisses (Emeleus, 1963). P3581 was emplaced at the Eastern end of the Vestvoldgrav-Østvoldgrav sill at the margin of the Pyramidefjeld granite complex.

UML from Nigerdlikasik and Pyramidefjeld can be considered extremely fresh, indicating that these rocks are representative of those originally emplaced. Combined with the unique structure of the NAC and the dominantly asthenospheric source for UML magmatism in South Greenland, the region offers a unique opportunity to investigate any influence of metasomatic C-SCLM material on UML magmatism. This dataset offers a unique insight into the origins of the metasomatic agents within the NAC of South Greenland.

UML magmatism at Pyramidefjeld is dated to between 152 – 150 Ma, comparative in age to those reported for similar rocks from the NAC at Faeringehavn and Tikiusaaq (Larsen et al., 2009; Tappe et al., 2017). No recent high-precision age data exists for UML at Nigerdlikasik. Bridgewater, (1970) and Andrews and Emeleus, (1971) report K-Ar ages from phlogopite separates for dykes at Pyramidefjeld and Nigerdlikasik which are broadly similar (220 – 193 Ma), albeit comparatively older when directly

compared to the high-precision data from Pyramidefjeld. It is probable that the UML at Nigerdlikasik and Pyramidefjeld are coeval due to the large tectonic control on melting and the close spatial relationship with rocks of near-identical ages (i.e. Tikiusaaq and Pyramidefjeld). This would suggest that the upwelling asthenospheric component of both UML is likely of similar composition. Thus, any geochemical dissimilarities between both UML would likely reflect assimilation of variably heterogeneous C-SCLM.

3.3. Ultramafic lamprophyre petrology

UML from Nigerdlikasik and Pyramidefjeld are texturally heterogeneous (Figure. 7a-b), both displaying inequigranular macrocrystic textures. Macrocrystic olivine occurs as two distinct populations based upon morphology (Figure. 7c-d). These populations comprise elongate or 'rounded' anhedral olivine ~0.1-2.5mm diameter (Ol-I) interpreted to derive from either within the convecting or lithospheric mantle (i.e. xenocrysts) and as sub to euhedral grains of olivine 0.01-1.4mm in diameter (Ol-II) that have been interpreted to have crystallized, at least in part during magma emplacement and crystallization (e.g. Kamenetsky et al., 2008; Bussweiler et al., 2015). Phlogopite occurs as 100-600 μm euhedral laths that occasionally display reverse zonation which are hosted within a calcite/dolomite carbonate and primary serpentine matrix, with carbonate also forming distinct rhombs' (Figure. 7a). Accessory groundmass phases are typically < 50 μm, comprising: Ca-perovskite occasionally overgrown by rutile, spinel, pyrite, diopside and complex aggregates of apatite. In UML from Pyramidefjeld primary serpentine comprises the majority of the matrix with carbonate a less common constituent, with opaque groundmass phases also making up a far greater proportion of the whole-rock than in UML from Nigerdlikasik.

Olivine is rarely fully replaced by serpentine, and serpentinization where present, forms as irregular banded psuedomorphs after original crystal habit (Figure. 7f). These serpentine psuedomorphs after olivine are not infiltrated by primary interstitial serpentine within the matrix. This implies that serpentinzation of olivine is a primary magmatic feature resulting from interaction of olivine with the UML melt during emplacement and ascent through the lithosphere. Radiating mesh serpentine indicative of formation of chrysotile at low temperature are not present. On this basis olivine from both UML can be considered extremely 'fresh' and unaffected by weathering and alteration at the Earth's surface, a relative rarity among olivine of alkaline ultrapotassic

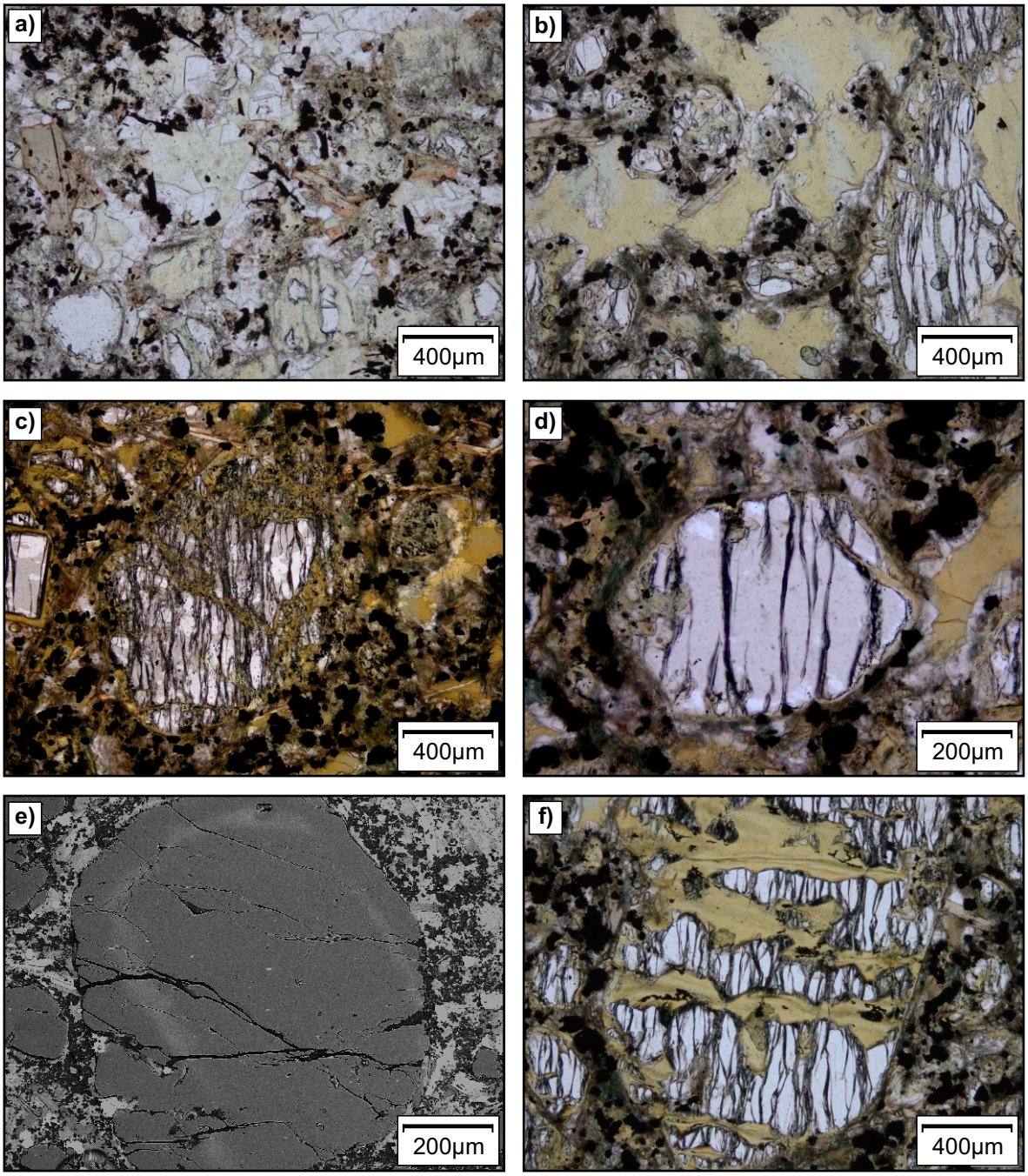

Figure 7 (a-f): Photomicrographs of ultramafic lamprophyre (UML) and hosted mineral phases from Nigerdlikasik and Pyramidefjeld. Photomicrograph a: (Nigerdlikasik) and b: (Pyramidefjeld) displays the texturally heterogeneity of the UML studied. Photomicrographs b and c display macrocryst olivine. olivine in c) is inferred to derive from the C-SCLM whilst d) is implied to have at least in part crystallized from the UML melt. e) displays a scanning electron microscope image under a back-scatter electron detector which displays FeO zonation implying complex FeO evolution of the UML melt. f) displays serpentinization of olivine that appears on a textural basis to be a magmatic feature.

and/or ultramafic magmatism. This also suggests that remobilization of volatile elements (e.g. halogens) is likely to be limited.

3.4. Xenolith petrology

Xenoliths recovered from UML at Nigerdlikasik and Pyramidefjeld are listed in Table. 2 with their modal mineral assemblages. The xenoliths range in type from granular spinel harzburgite (NX-07), texturally typical of depleted C-SCLM worldwide, to strongly metamorphosed phlogopite-bearing dunites/wehrlites. One orthopyroxenite xenolith was also recovered (NX-06). Secondary clinopyroxene is common xenoliths often intergrown with phlogopite ranging in abundance from 1.0 – 9.2 wt. % occasionally found accessory recrystallized olivine. Conversely, phlogopite within NX-01 is closely associated with orthopyroxene. Spinel is relatively common as a minor accessory phase but often not in modal abundance, suggesting a comparative Al_2O_3- and SiO_2-depletion in the C-SLCM of the NAC, relative to other cratons worldwide. Ilmenite occurs in several samples and comprises up to 8 wt. % abundance of the sample NX-03. Several samples display foliation, shear fabrics and grain-boundary recrystallization of olivine. Shear localization by dynamic solid-state recrystallization of olivine is demonstrated by a reduction of grain size of olivine and generation of neoblasts, which in the extreme case of NX-08 has formed an olivine mylonite. Apatite occurs as small < 50 μm grains deposited along grain boundaries commonly found with carbonate minerals (magnesite, dolomite, and calcite). Serpentinization of olivine is observed in three samples (PX-01, NX-02 and NX-03) along highly-channelized sub-parallel vein networks occasionally found with magnetite. These serpentine vein networks are cross-cut by UML infiltration and are implied to be unrelated to UML emplacement or post emplacement alteration and reflect a texture originating in the C-SCLM. The presence of serpentine suggest that the xenoliths are equilibrated at P/T conditions within the antigorite stability field (< 100 km on a typical cratonic geotherm), an interpretation supported by the presence of spinel. Pentandite and barite are commonly found accessory sulphide phases.

Location	Sample	Mineral Modes (%)				
		ol	*cpx*	*opx*	*phl*	*opaque*
Nigerd	NX-01	69.6	0.8	15.6	13.6	0.4
Nigerd	NX-02	88.2	9.2	0.6	2.0	-
Nigerd	NX-03	82.0	3.4	-	7.0	7.6
Nigerd	NX-04	93.2	3.2	2.2	1.4	-
Nigerd	NX-05	86.8	8.0	-	0.4	4.8
Nigerd	NX-06	-	-	100.0	-	-
Nigerd	NX-07	66.1	1.0	24.2	-	8.7
Nigerd	NX-08	100	-	-	-	-
Pyramid	PX-01	87.8	6.6	-	5.6	-

Table 2: Modal mineral assemblages of xenoliths recovered from Pyramidefjeld (Pyramid) and Nigerdlikasik (Nigerd), ol = olivine; cpx = clinopyroxene; opx = orthopyroxene; phl = phlogopite. T°C estimates from the Cr-in-olivine thermometer of De Hoog et al., (2010).

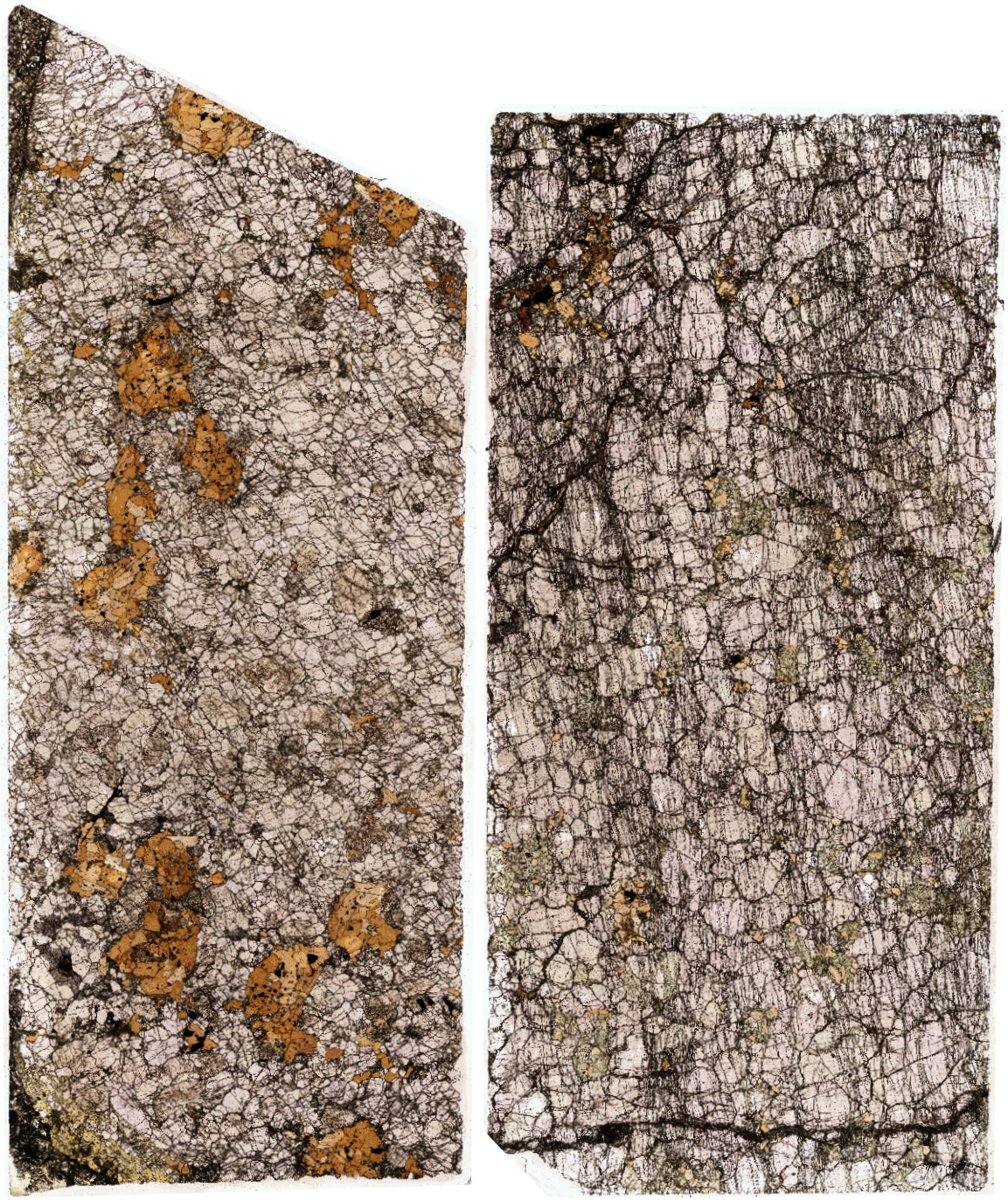

Figure 8a: Photomicrographs of 60μm thin-sections of C-SCLM xenoliths NX-01 (left) and PX-01 (right) recovered from UML at Nigerdlikasik and Pyramidefjeld respectively.

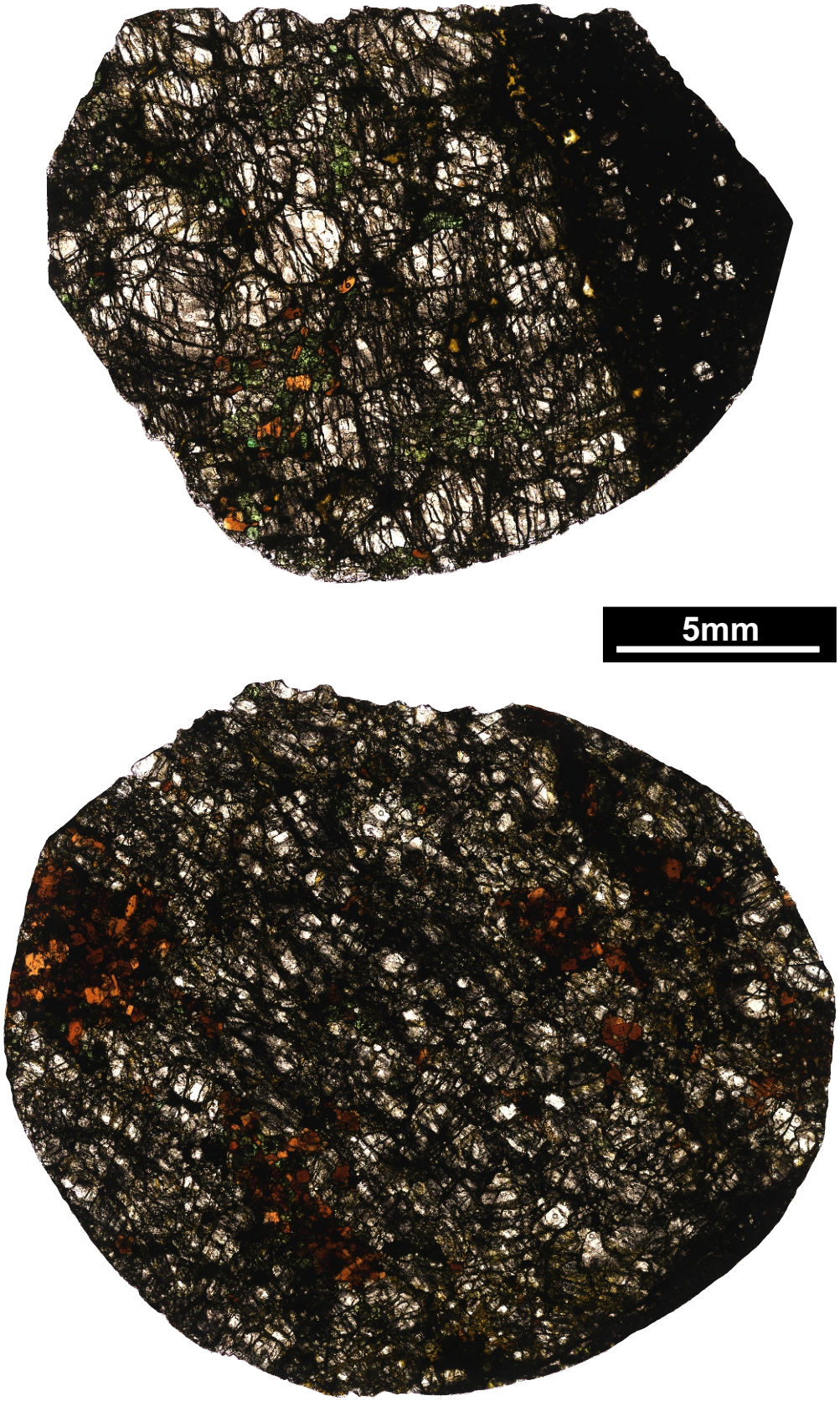

Figure 8b: Photomicrographs of 200μm thin-sections of C-SCLM xenoliths NX-02 (top) and NX-03 (bottom) recovered from UML at Nigerdlikasik.

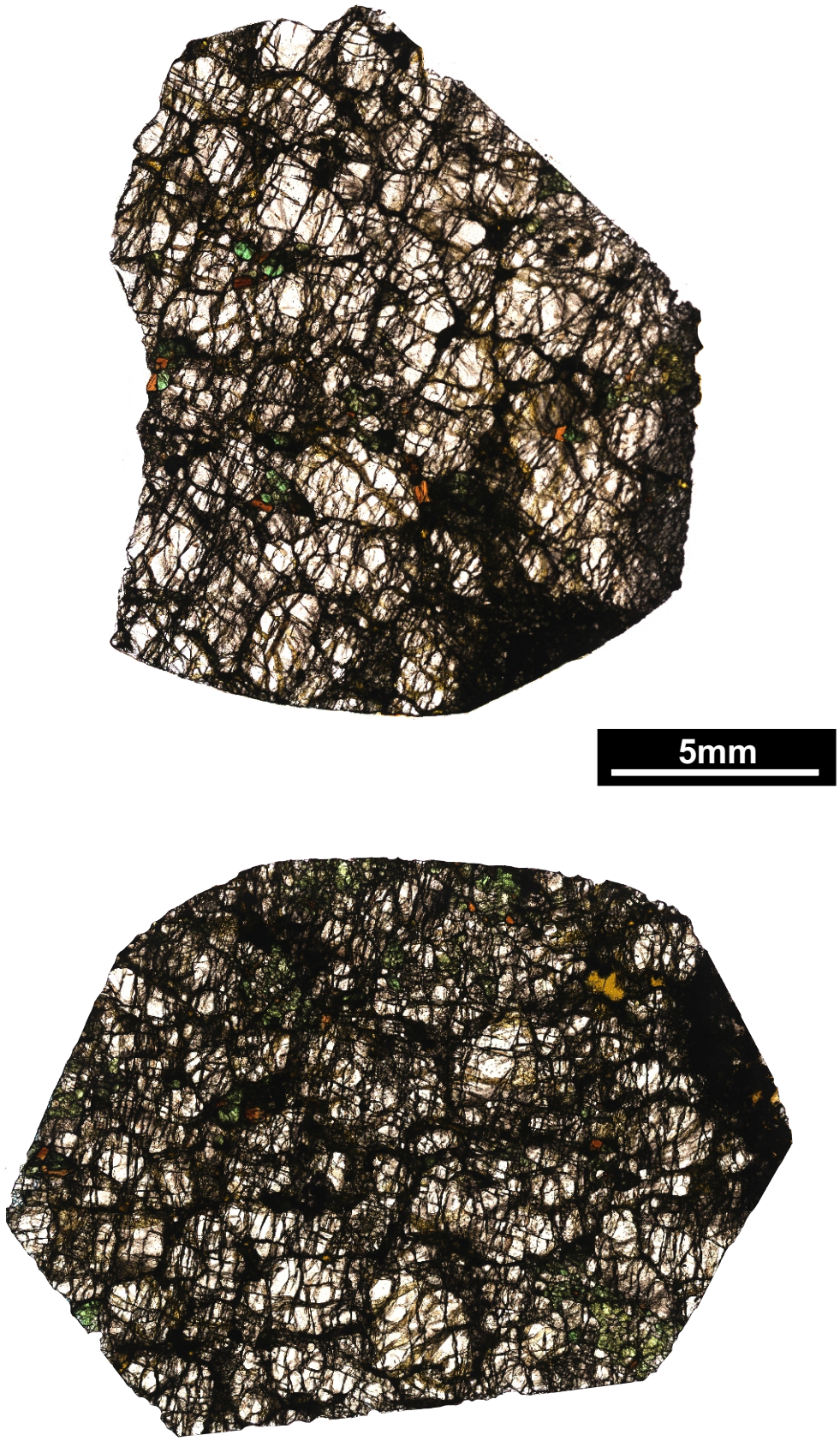

Figure 8c: Photomicrographs of 200μm thin-sections of C-SCLM xenoliths NX-04 (top) and NX-05 (bottom) recovered from UML at Nigerdlikasik.

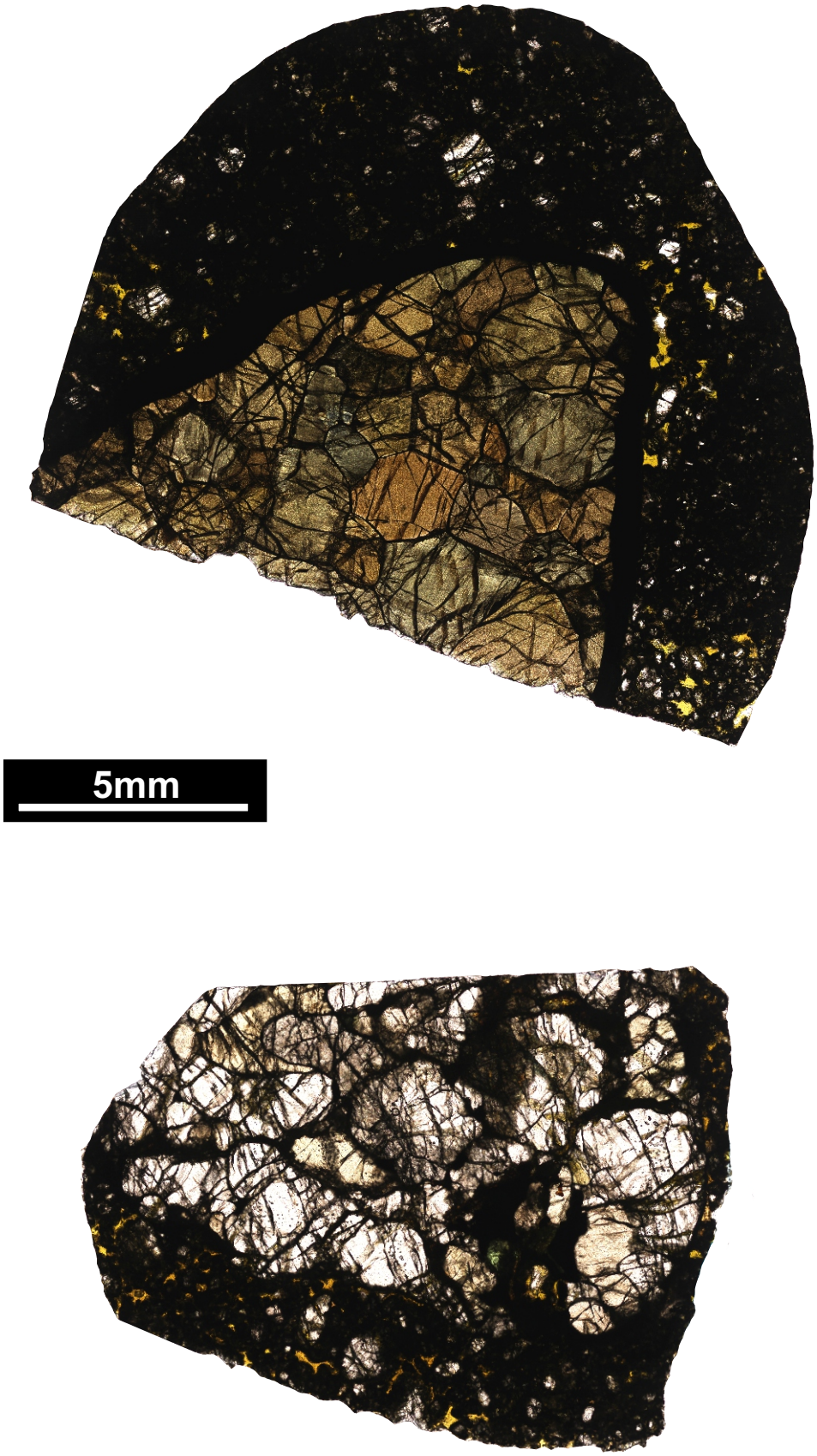

Figure 8d: Photomicrographs of 200µm thin-sections of C-SCLM xenoliths NX-06 (top) and NX-07 (bottom) recovered from UML at Nigerdlikasik.

Figure 8e: Photomicrograph of a 200μm thin-section of C-SCLM xenolith NX-08 recovered from UML at Nigerdlikasik.

Chapter 4.0: Methods

4.1. Bulk-rock analysis

4.1.1. WD-XRF

Whole-rock F, Cl and Br and other additional trace element analysis was undertaken by Professor Matthew Thirlwall at Royal Holloway, the University of London X-ray Fluorescence laboratory. Analysis was undertaken using a 2010 PANalytical Axios sequential X-ray fluorescence spectrometer with a 4Kw Rh-anode X-ray tube. Major elements for both UML were analysed on fused glass discs containing a La_2O_3 heavy absorber. Trace elements were analysed on 10g pressed pellets. Fe was analysed in both fused glass discs and pressed pellets as a comparative internal standard. WD-XRF trace element data for UML from Pyramidefjeld closely follow the trend for all elements analysed via solution ICP-MS by (Larsen et al., 2009), excluding Cs and Yb likely due to spectral interferences of Ti ($K\alpha_1$) and Ni ($K\alpha_1$) respectively. Sample calibrations of F, Cl and Br for a variety of geological standards are provided (Figure. 9). Accuracies of F, Cl and Br analyses in reference materials with similar halogen contents to the studied UML fall within 5% of the calibration lines. Spectral interferences on Cl and Br are expected to be negligible due to the expected relative abundances and intensities of the interfering species (e.g. Mo - $L\gamma_1$; As - $K\beta_1$ and Bi – $L\eta$; Tl - $L\beta_{1,4}$ respectively).

4.1.2. δ^{37}Cl isotope by IRMS

Cl isotope analyses were completed at the University of Texas at Austin by Dr Jaime Barnes based on the procedures of Eggenkamp, (1994) as modified by Barnes and Sharp, (2006) and (Sharp et al., 2007). Whole rock; and picked phlogopite powders, from xenolith NX-01, were washed five times each, in ultrapure deionized water, in order to remove any potential surficial chlorine contamination, and subsequently dried. Chloride was extracted from the rock powders into an aqueous solution via pyrohydrolysis (Magenheim et al., 1994). Chloride in solution was precipitated as AgCl via reaction with $AgNO_3$. The AgCl was then reacted with CH_3I at 80 °C for 48 hours to produce CH_3Cl. CH_3Cl was purified from excess CH_3I on a gas chromatographic system in a continuous He flow before introduction into a ThermoElectron MAT 253 mass spectrometer. Data are reported in standard per mille (‰) notation relative to SMOC (standard-marine ocean chloride). Precision is ± 0.2‰ (1σ) based on the long-

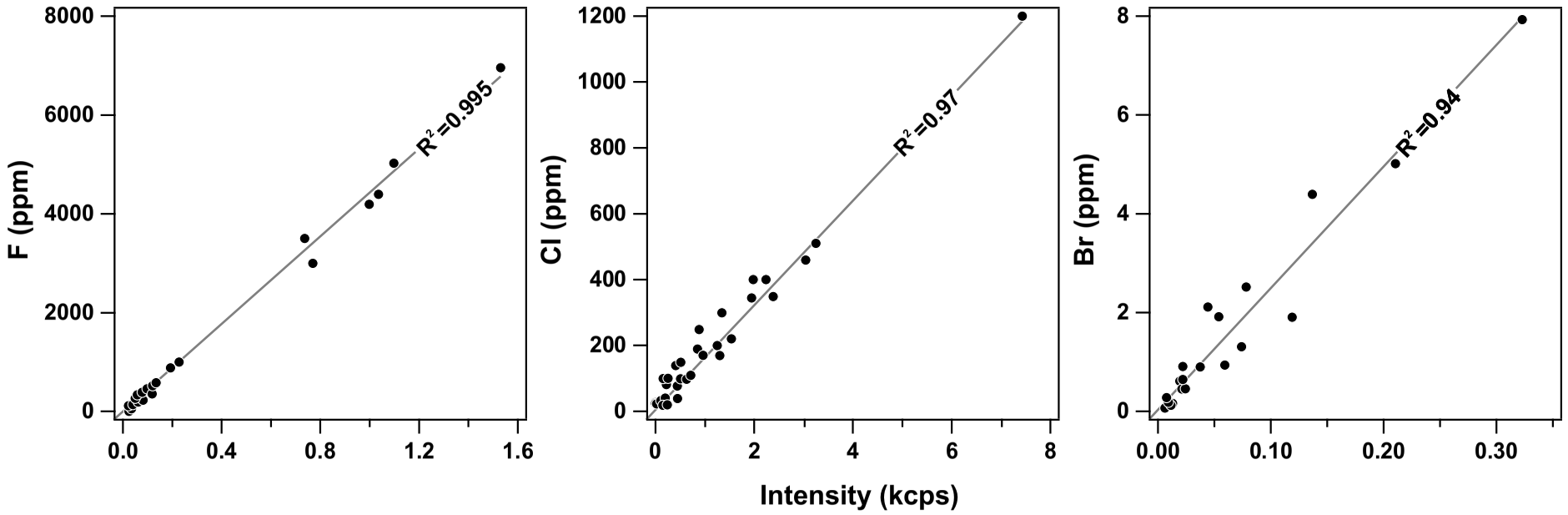

Figure 9: Calibration lines for volatile elements for WD-XRF analysis based on the following reference materials: AGV2, ALI, ANG, BCR2, BEN, BHVO1, BIR1, BR, DNC1, DRN, DTN, DTS1, DTS2, FKN, GA, GH, GSN, GSP2, IFG, MAN, MRG1, NIMD, NIMG, NIML, NIMN, NIMP, NIMS, PCC1, PMS, QLO1, RGM1, SDC1, STM1, SY2, SY3, UBN, W2, WSE.

term average of three internal seawater standards and one internal serpentinite standard. The serpentinite rock standard demonstrates that the pyrohydrolysis process does not increase the analytical error.

4.2. Mineral analysis

4.2.1. SEM-EDX

Major elements of UML and C-SCLM phases were analysed by energy-dispersive X-ray spectroscopy via scanning electorn microscopy (SEM-EDX) at the iCRAG laboratory, Trinity College Dublin (TCD). Analyses were carried out using a Tescan MIRA XMU variable pressure Field Emission Scanning Electron Microscope (FE-SEM) equipped with an Oxford X-Max 80mm^2 EDS detector and a Tescan TIGER MIRA3 Variable Pressure FE-SEM, equipped with two Oxford DEX 150mm^2 detectors. Both the Tescan MIRA XMU and TIGER MIRA3 Variable Pressure FE-SEMs utilize the Oxford Instruments AZtec X-ray microanalysis software suite. A beam current of ~280pA and an accelerating voltage of 20kV was applied for all analytical runs where phlogopite was not analysed. In analytical runs where phlogopite was analysed the acceleration voltage was lowered to 15kV to protect halogen contents from volatile-migration resulting from remobilization during surface heating of sample during analysis. Beam current drift was restricted by frequent analysis of cobalt. The instrument was calibrated using a suite of appropriate mineral standards from the Smithsonian Institute (Jarosewich et al., 1980). The SEM-EDX analysis procedure employed follows Ubide et al., (2017). Analytical biases of 0.06%, 3.7% and 0.65% were attained for the natural diopside reference mineral NMNH 117733 for SiO_2, MgO and CaO respectively, - 0.76% for Al_2O_3 for the natural pyrope reference mineral NMNH 143968 and 0.27% for FeO for the natural olivine reference material NMNH 111312-44.

The analytical bias for MgO measurement comparative to suitable standard material, although acceptable, is slightly high. MgO wt. % concentration for diopside NMNH 117733 was initially reported by Jarosewich et al., (1980) at 18.30 wt. %, with a subsequent and final preferred value of 17.79 wt. % provided by the Smithsonian Institute (following subsequent reanalysis by E. Jarosewich). The bias discussed above is reported as a ± % deviation from the preferred value of 17.79 wt. %. Diopside NMNH 117733 (Natural Bridge, NY) is a quality-control standard monitored by the

iCRAG laboratory in which the analysis was undertaken. Long-term reproducibility of MgO of diopside NMNH 117733 within the laboratory provides an MgO wt. % of 18.36 (n= 39) ± 0.22 (1σ) and a bias of + 3.2 %. The bias of + 3.7 % reported here for comparison corresponds to an MgO wt. % of 18.42 (n= 8) ± 0.11 (1σ) for diopside NMNH 117733 only marginally higher than those above. Bias for MgO measurement reported by Ubide et al., (2017) for pyrope NMNH 143968 (Kakanui, NZ) and basaltic glass NMNH 111240-52 (Juan de Fuca, Pacific Ocean) are reported as + 2.8% and + 2.6% respectively.

A possible explanation of the positive MgO bias on analysis of diopside NMNH 117733 could result from standardization of MgO during analytical setup. In the followed analytical procedure (e.g. Ubide et al., 2017), augite NMNH 122142 (Kakanui, NZ) is used as a calibration standard for MgO. Data presented by Jarosewich et al., (1980) suggest that these grains are considered homogenous in composition, provided that a suitable number of different grains are analysed. In practice, standardisation procedures make use of one grain. Under these circumstances a grain used for standardization having a slightly different composition than that reported may influence SEM-EDX results adversely (e.g. Jarosewich et al., 1980). When a differing calibration standard is used for analysis of MgO (e.g. pyrope NMNH 143968), concentrations of MgO within diopside NMNH 117733 and olivine NMNH 111312-44 (San Carlos) are 17.8 wt. % (n= 14) ± 0.17 (1σ) for an bias of ~ 0 % and 49.27 wt. % (n= 5) ± 0.13 (1 σ) for a bias of 0.8 %, respectively. The combined dataset suggests MgO concentrations could be systemically overestimated when augite NMNH 122142 used within the iCrag laboratory as an MgO calibration standard. If MgO contents within augite NMNH 122142 used in the calibration are higher than those reported by Jarosewich et al. (1980) the procedure would prompt an overestimation of MgO contents. Such an interpretation is supported by analysis of olivine and enstatite unknowns reported for xenolithic and xenocrystic phases recovered from both UML (Table. 8; 10) where augite NMNH 122142 was used as the MgO calibration standard. These phases (both MgO-rich) have a slight overabundance of cations on their respective M-sites.

4.2.2. LA-ICP-MS

Trace elements were analysed in clinopyroxene and phlogopite within several C-SCLM xenoliths recovered from both UML at Nigerdlikasik and Pyramidefjeld by laser-ablation inductively coupled plasma mass spectrometry (LA-ICP-MS) at TCD. LA-ICP-

Laser parameters	Cpx	Phl
Fluence (J cm^{-2})	2.75	2.75
Shots	2000	2000
Laser rep. rate (Hz)	20	12
Laser spot size (µm)	85 x 85	100 x 120
Spot shape	square	slit
Background measurement (s)	60	60
Elements analysed	^{23}Na	^{24}Mg
	^{24}Mg	^{29}Si
	^{29}Si	^{35}Cl
	^{39}K	^{79}Br
	^{45}Sc	^{85}Rb
	^{48}Ti	^{88}Sr
	^{51}V	^{90}Zr
	^{59}Co	^{93}Nb
	^{60}Ni	^{133}Cs
	^{85}Rb	^{137}Ba
	^{88}Sr	^{139}La
	^{89}Y	^{178}Hf
	^{90}Zr	^{181}Ta
	^{93}Nb	^{208}Pb
	^{133}Cs	^{232}Th
	^{137}Ba	
	^{139}La	
	^{140}Ce	
	^{146}Nd	
	^{147}Sm	
	^{160}Gd	
	^{163}Dy	
	^{166}Er	
	^{172}Yb	
	^{178}Hf	
	^{181}Ta	

Table 3: Laser parameters and elements analyzed by laser-ablation inductively-coupled-plasma mass spectrometry (LA-ICP-MS)

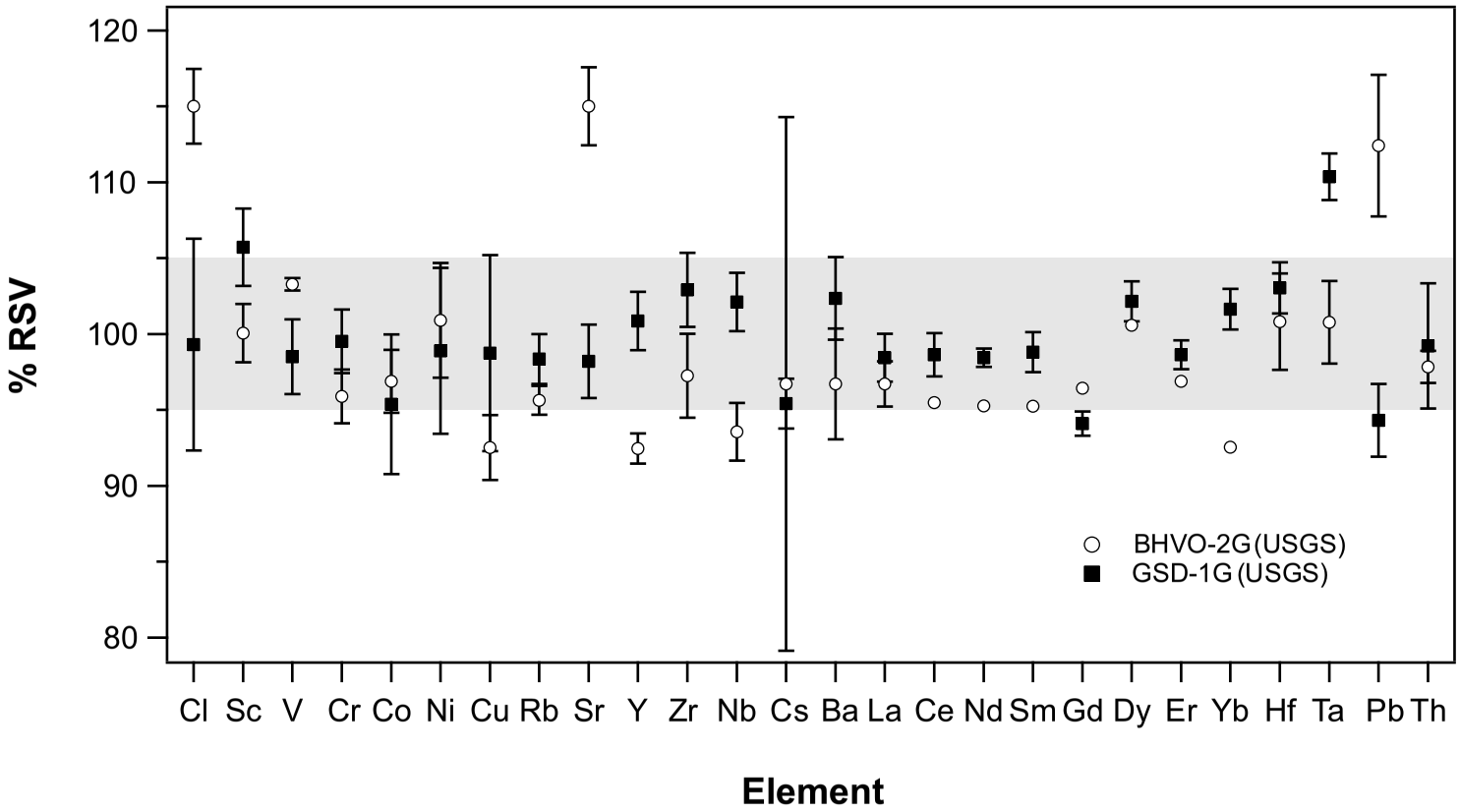

Figure 10: % of Recommended Standard Value (RSV) for reference materials that were used as quality monitors for all experiments plotted in order of atomic mass. Range bars represent 1s. For ease of comparison, an area has been shaded to highlight the data that is within the ± 5% of RSV.

MS analysis was conducted using a Teledyne Photon Machines Analyte G2 laser ablation system, comprising a 193nm ArF excimer laser and a HeLex II active two-volume ablation cell, coupled to a Thermo iCAPQc ICP-MS. Analytical conditions and elements analysed for each phase are reported in Table. 3. The calibration standard used was SRM NIST-612 with USGS GSD-1G and USGS BHVO-2G used as quality control standards. % RSV (recommended standard value) for all analysed elements is shown in Figure. 10.

Chapter 5.0: Results

5.1. Whole-rock geochemistry

5.1.1. Major and trace element compositions

Major and trace-element geochemistry of whole-rock samples from Pyramidefjeld and Nigerdlikasik are reported in Table. 4a and b and are shown in Figure. 11. UML from Nigerdlikasik and Pyramidefjeld have high MgO of 30.92 wt. % and 32.08 wt. % with #Mg 82 and 78, low SiO_2 of 31.0 wt. % and 33.2wt. %, low Al_2O_3 of 3.1 wt. % and 3.0 wt. % and TiO_2 of 3.0 wt. % and 2.2 wt. %, respectively. SiO_2 of Pyramidefjeld at 33.2 wt. % is slightly higher than reported than maximum values for UML at Sarfartoq, Sisimiut and Faeringehavn and transitional kimberlites at Tikiusaaq or kimberlite from Maniitsoq (Figure. 11). Al_2O_3 contents are comparable to UML from elsewhere in South Greenland but significantly enriched comparative to kimberlite from Maniitsoq (Figure. 11). Nigerdlikasik and Pyramidefjeld UML are ultrapotassic in terms of $K_2O/Na_2O > 3$. However, the low bulk K_2O contents of both UML classify both as potassic. K_2O and Na_2O concentrations are comparable to the range observed in UML from Sarfartoq, Sisimiut and Faeringehavn and transitional kimberlites from Tikiusaaq which are all significantly enriched compared to Maniitsoq kimberlites (Figure. 11). P_2O_5 concentrations of UML at Nigerdikasik and Pyramidefjeld are low at 0.43% and 0.51% with little discernible variation in P_2O_5 concentrations between all kimberlite and UML (Figure. 11) suggesting insignificant apatite in the source region. Volatile contents of both UML are high, evidenced by loss-on-ignition (LOI) of 16.2 wt. % for Nigerdlikasik and 14.5 wt. % for Pyramidefjeld. SO_3 contents of both UML fall within a range of concentrations for those reported globally (see GEOROC database) for both kimberlite (~ 0.26 wt. %) and alkaline lamprophyre (0.26 wt. %) albeit below each respective average.

Nigerdlikasik and Pyramidefjeld UML both display high mantle incompatible and compatible element abundances normalized to primitive mantle (values of Sun and McDonough, 1989) on trace element variation diagrams. Incompatible elements are strongly fractionated with systematic enrichment of the most incompatible elements over those more compatible, as demonstrated in the steep profile of the trace (Figure. 12). Both UML display marked depletions in K and Ti as well as a slight depletion in Zr-Hf. Comparatively, UML from Nigerdlikasik are generally more enriched in all

Location	Nigerd	Pyramid
TCD No.	P3580	P3581
Sample	NA-01	PA-01
SiO_2	30.99	33.15
TiO_2	2.16	3.04
Al_2O_3	3.08	2.95
FeO_t	12.70	15.41
MnO	0.23	0.24
MgO	32.08	30.92
Mg#	81.83	78.15
CaO	15.01	11.39
Na_2O	0.10	0.28
K_2O	1.66	1.28
P_2O_5	0.43	0.51
LOI	16.24	14.50
Total (%)	98.71	99.31

Table 4a: Major elements (oxide wt. %) for whole-rock UML from Nigerdlikasik (Nigerd') and Pyramidefjeld (Pyramid'). LOI = volatile loss on ignition, total iron is reported as Fe^{2+}. Mg# = (Mg / Mg + Fe) x 100.

Location	Nigerd	Pyramid
TCD No.	P3580	P3581
Sample	WR-01	WR-02
F	2517	1469
Cl	1242	1245
Br	6.0	5.9
S	1676	2116
Sc	25.7	20.9
V	177.4	243.5
Cr	1936	1556
Co	89	110
Ni	1142	1100
Cu	26.4	87.7
Zn	73.4	99.3
Ga	7.8	11.2
As	1.9	1.3
Rb	103.5	49.0
Sr	1497	821
Y	17.3	13.9
Zr	277.4	205.3
Nb	199.8	116.2
Mo	2.3	2.2
Ba	2696	519
La	129.3	83.6
Ce	207.0	150.5
Nd	75.9	63.2
Sm	9.5	9.6
Hf	5.6	4.2
Ta	8.9	8.4
Pb	14.0	3.2
Th	13.4	8.5
U	2.9	2.0
F/Cl	2.0	1.2
Br/Cl	0.0049	0.0047
δ^{37}Cl	1.0	1.2
Zr/Hf	49.5	48.9
Zr/Nb	1.4	1.8
Nb/Ta	22.5	13.8
Nb/U	68.9	59.2
Nb/Th	14.9	13.6
Ba/Nb	13.5	4.5
Ce/Pb	14.8	46.5

Table 4b: Trace elements (ppm) for whole-rock UML from Nigerdlikasik (Nigerd') and Pyramidefjeld (Pyramid'). Cs and Yb were analyzed but not reported see text due to suspected spectral interferences

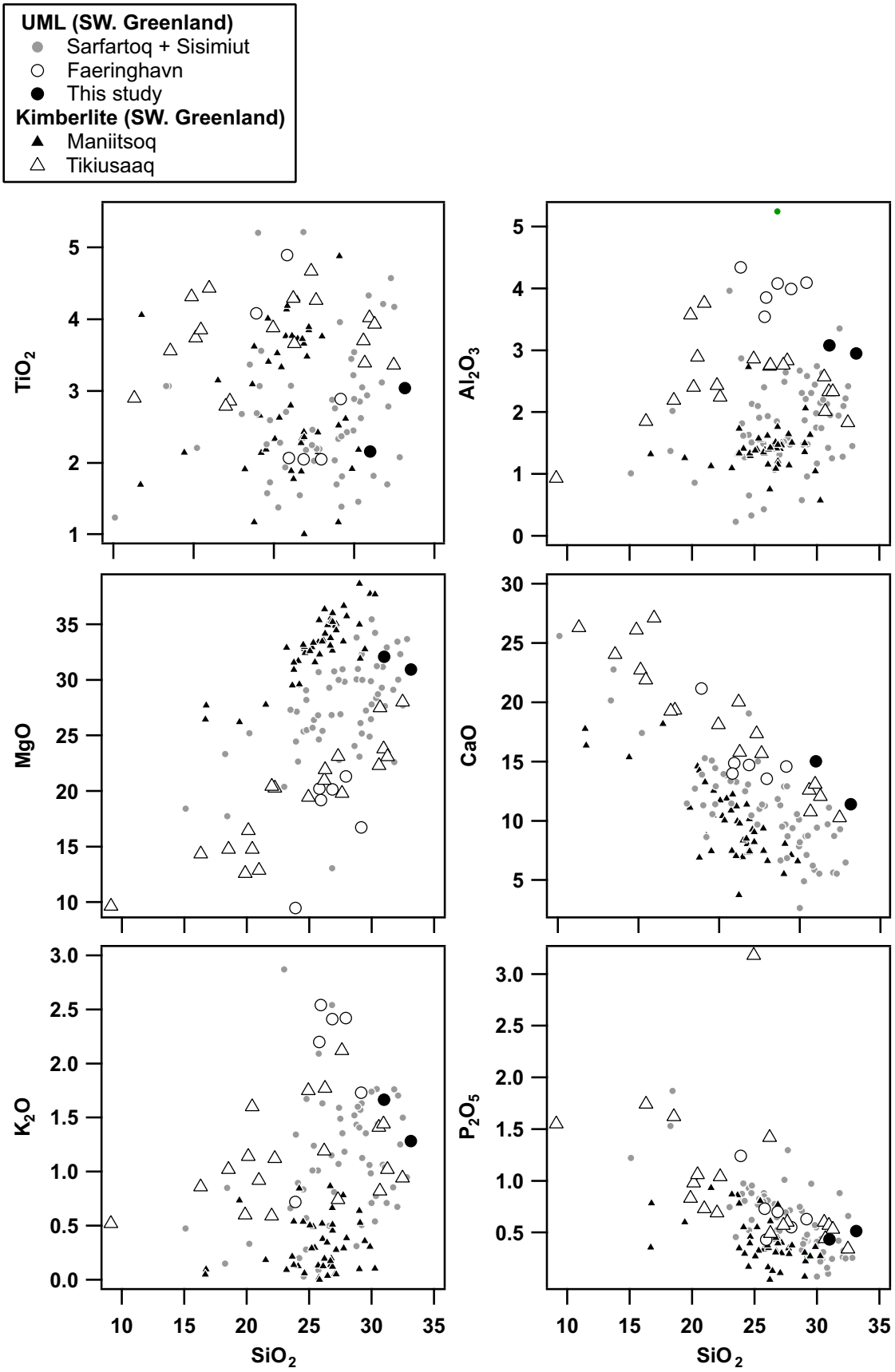

Figure 11: Major elements for ultramafic lamprophyre (UML) from Pyramidefjeld and Nigerdlikasik (this work) as well as other UML and kimberlite from the North Atlantic Craton, SW. Greenland. Data from Nielson and Jenson, (2005); Gaffney et al., (2007); Nielson et al., (2009); Tappe et al., (2011); Tappe et al., (2017).

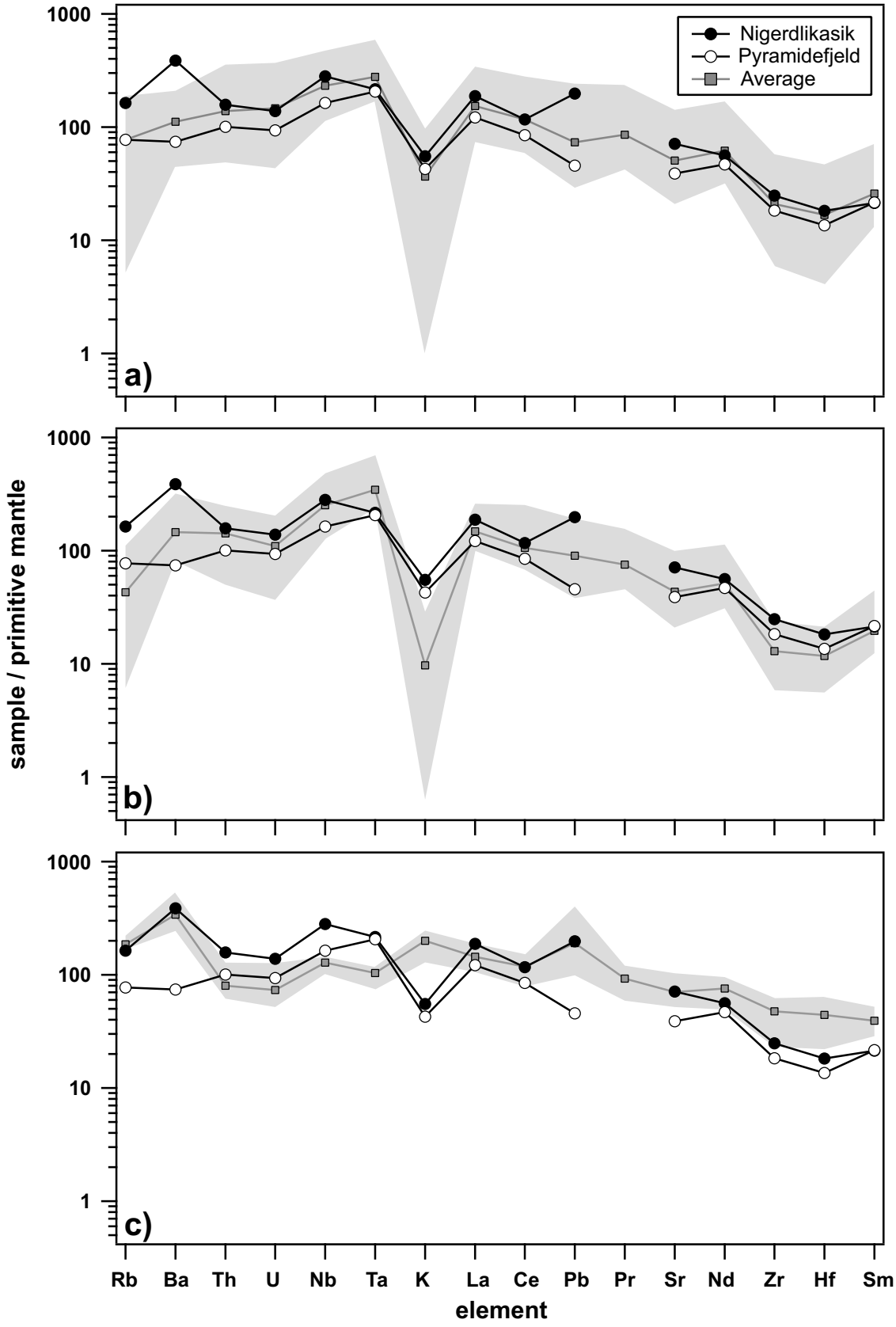

Figure 12: Incompatible trace element variation diagrams for ultramafic lamprophyre (UML) from Nigerdlikasik and Pyramidefjeld normalized against primitive mantle of Sun and McDonough, (1989). Panel a) shaded field of UML from Sarfatoq (Gaffney et al., 2007; Nielsen et al., 2009; Tappe et al., 2011), Panel b) shaded field of kimberlite from Maniitsoq (Nielsen and Jensen, 2005; Nielsen et al., 2009; Tappe et al., 2011), Panel c) shaded field of lamproite from Aillik Bay, Canada (Tappe et al., 2007). Average spider reflects average of respective field. Primitive mantle values of Sun and McDonough, (1989).

elements relative to UML from Pyramidefjeld but particularly in LILE and Nb. LILE enrichment of Nigerdlikasik is evidenced by Ba/Nb of 13.5 and Ce/Pb of 14.8. Pyramidefjeld by contrast has Ba/Nb of 4.5 and Ce/Pb of 46.5 comparative with UML from Sarfartoq and kimberlite from Maniitsoq with and Ba/Nb of ~5 and Ce/Pb of ~50 (Tappe et al., 2011); ratios that are also comparable to OIB magmatism (e.g. Hofmann, 1988). Nb/Ta of UML from Pyramidefjeld is subchondritic at 13.8, a value largely typical for both crustal and mantle rocks. By contrast Nb/Ta is supra-chondritic in UML Nigerdlikasik, which is unusual, although not unheard of for kimberlite or UML, and is relatively common in lamproite (e.g. Murphy et al., 2002; Tappe et al., 2007). Both UML display a strongly supra-chondritic Zr/Hf of ~49.

5.1.2. Halogens

Elemental and isotopic halogen data for the two UML magmas are reported in Table. 4b and Figures. 13 and 14 compared to data from several mantle-derived magmas, subduction inputs, subduction outputs and vein material within obducted eclogite-facies ophiolites recording antigorite dehydration. Halogen concentrations are rarely reported for kimberlite, or lamproite (e.g. Paul et al., 1976; Aoki et al., 1981; Kjarsgaard et al., 2009) and have never been reported for UML. Recent F and Cl concentrations are reported by Kjarsgaard et al., (2009) for the crustally uncontaminated Lac de Gras kimberlites from the Central Slave Craton, Canada. Lac de Gras kimberlites have F contents ranging from 474-1939 p.p.m., distributed around a mean value of 1200 ± 400 p.p.m. (1σ) and Cl contents where above detection (~100 p.p.m.) ranges from 112 – 240 p.p.m.. Fluorine concentrations in UML from Pyramidefjeld are 1469 p.p.m., and are highly comparable to kimberlites from Lac de Gras. By contrast, F concentrations for Nigerdlikasik appear distinctly more enriched with contents of 2517 p.p.m. Chlorine concentrations of UML from Nigerdlikasik and Pyramidefjeld are similar at 1242 and 1245 p.p.m. respectively, significantly enriched compared to kimberlites from Lac de Gras. F/Cl ratios of 2 and 1.2 for UML from Nigerdlikasik and Pyramidefjeld fall within a range comparable for MORB although distinctly lower than F/Cl ratios reported for kimberlite (Paul et al., 1976; Kjarsgaard et al., 2009). To date, Br has not been reported for any kimberlite or similar rock. Br contents are remarkably similar at 5.9 and 6.0 p.p.m. for UML from Nigerdlikasik and Pyramidefjeld respectively, and are both significantly enriched in Br compared to Br estimates of the Earth's primitive and modern-day convecting mantle (Table. 1). Br contents, as with Cl, of both UML are

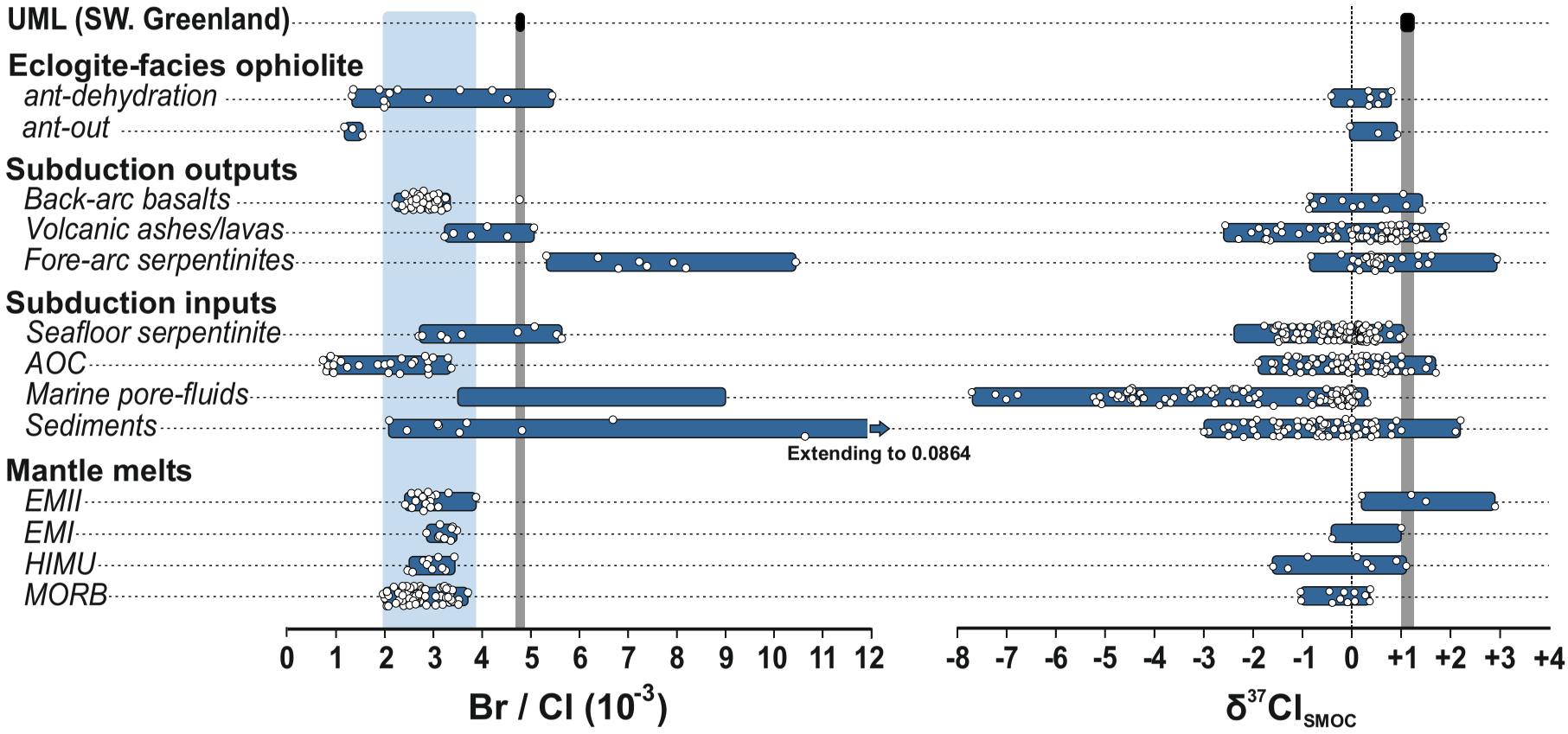

Figure 13: Br/Cl and $\delta^{37}Cl$ composition of ultramafic lamprophyre (UML) from Nigerdlikasik and Pyramidefjeld with compilation of reported Br/Cl and $\delta^{37}Cl$ for mantle melts (MORB: mid-ocean ridge basalt; HIMU *'high-μ'*: defined as mantle domains with highly radiogenic Pb isotope compositions; EM-I: enriched-mantle I; EM-II: enriched-mantle II) , subduction inputs, subdcution outputs, and eclogite-facies ophiolites.Blue shaded field demarks the range of Br/Cl of HIMU, EM-I, EM-II and MORB reported to date. Data reported for mantle melts (Kendrick et al., 2017 and references therein), subduction inputs (Muramatsu et al., 2007; John et al., 2011; Kendrick et al., 2013; Chavrit et al., 2016; Li et al., 2017), subduction outputs (John et al., 2011; Kendrick et al., 2013; Kendrick et al., 2014) and eclogite-facies ophiolite (John et al., 2011). Data for $\delta^{37}Cl$ [‰ versus standard marine ocean chloride (SMOC)] (Barnes et al., 2017 and references therein).

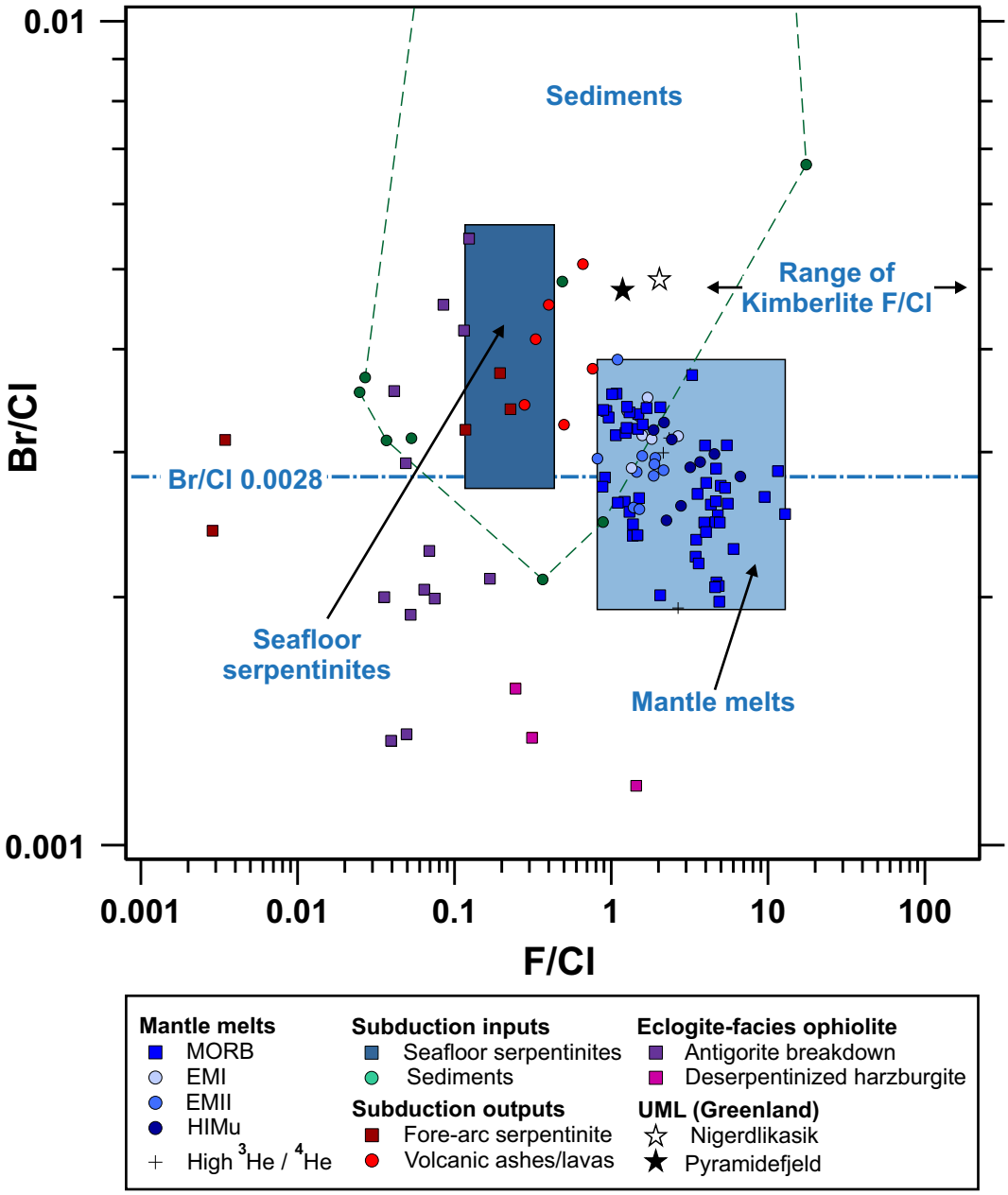

Figure 14: Br/Cl vs F/Cl for a variety reservoirs delivered in, and fluids released during, subduction as well as mantle derived melts. References; Sediments (John et al., 2011; Li et al., 2016), Mantle melts (Kendrick et al., 2017 and references therein), Fore-arc serpetinite (Kendrick et al., 2013), Volcanic ashes and lavas and veins in eclogite-facies ophiolite (John et al., 2011). Seafloor serpetinite field assuming F concentration of ~200 ppm (Mevel et al., 2003) and Br/Cl from the range reported for seafloor serpentinites by Kendrick et al., (2013). Range in kimberlite F/Cl reported by (Paul et al., 1977; Kjarsgaard et al., 2009).

remarkably uniform which generates a near-constant Br/Cl (~0.0048), higher than any reported Br/Cl value of MORB or OIB magmatism.

Nigerdlikasik and Pyramidefjeld UML display positive and statistically indistinguishable δ^{37}Cl values of +1.0 ± 0.2 ‰ and +1.2 ± 0.2 ‰, respectively. UML are enriched in ^{37}Cl relative to depleted upper mantle (Sharp et al., 2007; -0.2 ± 0.5%) as sampled by MORB (Figure. 13), but are comparable to enriched-type OIB (e.g. John et al., 2010). δ^{37}Cl data for kimberlite is limited and non-existent for UML. δ^{37}Cl is reported for halite from the Udachnaya-East kimberlite (Sharp et al., 2007; - 0.18 ± 0.3%) and carbonatite (Eggenkamp and Groos, 1997; - 0.2 ± 0.4%) both similar to δ^{37}Cl of the convecting mantle and BSE. A picked phlogopite separate from xenolith NX-01 has a positive δ^{37}Cl value (+1.3 ± 0.2 ‰) that is statistically indistinguishable from the UML.

5.2. UML major element mineral chemistry

5.2.1. Olivine

Representative olivine mineral analyses are provided in Table. 5. Zonation is common in most olivine macrocyrsts, although unzoned macrocrysts are also observed. Cores range in Mg# composition from ~85 to 93 with lower Mg# component generally corresponding to the lowest NiO content (Figure. 15). Zoning is more commonly normal although reverse zoning is also observed in several samples with resorption features. Generally, cores with Mg# content < 89 have NiO contents of < 0.3 wt. %, while cores with Mg# content > 90 have NiO contents of > 0.3 wt. % extending as far as 0.45 wt. %. Spinel inclusions within high Mg# olivine suggests their origin as scavenged from the C-SCLM during UML ascent as does high Mg# and NiO contents. Several olivine cores, although displaying sharp compositional divides between core and rim, display no obvious habit. Rim composition in terms of Mg# composition converges tightly at 89.5-90.5 and are typically more depleted in NiO comparative to core compositions. A conspicuous overgrowth is observed around a euhedral olivine core of with Mg# composition of 90 (Figure. 7e). This euhedral overgrowth is markedly lower in Mg# composition ~87 and is rimmed by olivine compositionally identical to observed rims surrounding both types of core (e.g. ~Mg# 90 and ~0.15 - 0.2 wt. % NiO). CaO of olivine cores are generally < 0.1 wt. %, with rim composition generally more enriched than cores in zoned olivine with Ca contents extending to 0.24 wt. %. This might be suggestive of equilibrium with a high-Ca melt or a decrease in

Location:	Nigerd	Nigerd	Nigerd	Nigerd	Nigerd	Nigerd	Nigerd	Nigerd
Sample:	NA-02	NA-02	NA-02	NA-02	NA-02	NA-02	NA-02	NA-02
Mineral:	Ol-4	Ol-4	Ol-8	Ol-8	Ol-9	Ol-9	Ol-20	Ol-20
Zone:	core	rim	core	rim	core	rim	core	rim
SiO_2	40.00	40.19	39.28	40.25	39.82	39.86	39.97	40.32
TiO_2	0.03	0.08	0.02	0.04	0.02	0.02	0.02	0.05
Al_2O_3	0.00	0.12	0.08	0.07	0.02	0.02	0.05	0.08
Cr_2O_3	0.03	0.07	0.02	0.05	0.04	0.02	0.06	0.02
FeO	8.14	9.49	14.17	9.73	10.89	9.55	12.47	9.84
MnO	0.07	0.12	0.18	0.16	0.13	0.16	0.17	0.16
NiO	0.36	0.25	0.25	0.18	0.27	0.25	0.24	0.13
MgO	49.89	49.20	45.41	49.47	48.38	49.40	47.20	49.48
CaO	0.10	0.11	0.08	0.18	0.01	0.13	0.05	0.25
Na_2O	0.03	0.05	0.05	0.05	0.06	0.04	0.05	0.04
K_2O	0.01	0.00	0.01	0.01	0.02	0.00	0.02	0.00
Total	98.59	99.66	99.50	100.16	99.63	99.40	100.26	100.35
Si	0.99	0.99	0.99	0.99	0.99	0.99	0.99	0.99
Ti	0.00	0.00	0.00	0.00	0.00	0.00	0.00	0.00
Al	0.00	0.00	0.00	0.00	0.00	0.00	0.00	0.00
Cr	0.00	0.00	0.00	0.00	0.00	0.00	0.00	0.00
Fe	0.17	0.20	0.30	0.20	0.23	0.20	0.26	0.20
Mn	0.00	0.00	0.00	0.00	0.00	0.00	0.00	0.00
Ni	0.01	0.00	0.01	0.00	0.01	0.00	0.00	0.00
Mg	1.84	1.81	1.71	1.81	1.79	1.82	1.74	1.81
Mg#	91.62	90.24	85.11	90.06	88.79	90.21	87.10	89.96
Ca	0.00	0.00	0.00	0.00	0.00	0.00	0.00	0.01
Na	0.00	0.00	0.00	0.00	0.00	0.00	0.00	0.00
K	0.00	0.00	0.00	0.00	0.00	0.00	0.00	0.00
Cations	3.01	3.01	3.01	3.01	3.01	3.01	3.01	3.01

Table 5: Representative major element analyses of macrocrystic olivine from UML at Nigerdlikasik (Nigerd') by energy-dispersive X-ray spectroscopy via scanning electron microscope (SEM-EDX). Analyzes spans the range of reported Mg # - (Mg / Mg + Fe) x 100. Cations normalized against 4 oxygen.

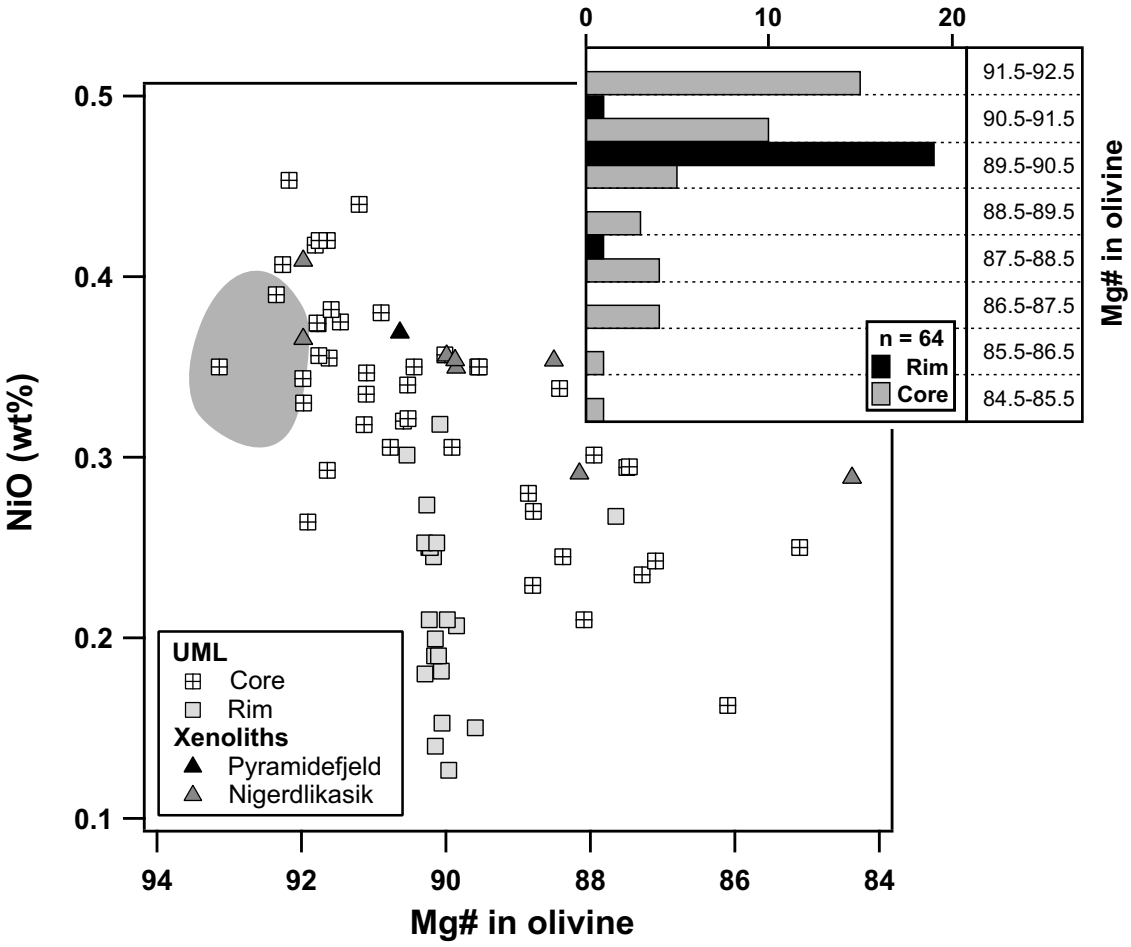

Figure 15: NiO vs Mg# in olivine (Mg / Mg + Fe) for macrocryst olivine (core and rim) as well as olivine from xenoliths recovered within ultramafic lamprophyre (UML) from Nigerdlikasik and Pyramidefjeld, shaded area displaying ultra-depleted olivine from Ubekendt Ejland (Greenland), using data of Bernstein et al., (2007) Inset histogram displays frequency of Mg# of macrocryst olivine from UML.

temperature. These rims could be argued to be representative of the early melt compositions (e.g. Kamenetsky et al., 2008).

5.2.2. Spinel

Representative spinel mineral analyses are provided in Table. 6. Spinel from UML at Nigerdlikasik and Pyramidefjeld follow the T2 'titanomagnatite trend' defined by Mitchell, (1995) characterized by $Fe_T^{2+}/ Fe_T^{2+} + Mg > 0.7$ with increasing TiO_2 and FeO_t contents, corresponding to a decrease in MgO, Cr_2O_3 and Al_2O_3 (Figure. 16). Cr-spinel cores form a tight field corresponding to $Fe_T^{2+}/ Fe_T^{2+} + Mg$ ranging from 0.7 - 0.78 and Ti / Ti + Al + Cr ranging from 0.05 to 0.1 and are similar to Cr-spinel recovered from mantle xenoliths in both UML from Nigerdlikasik (c.f. Table. 12). These cores likely originate from the disaggregated C-SCLM, which form a nucleus for subsequent T2 trend spinel rim growth. Titaniferous-magnetite rims trend from 0.45 to 0.62 Ti / Ti + Al + Cr at $Fe_T^{2+} / Fe_T^{2+} + Mg$ ranging 0.81 to 0.91. These spinel are significantly less magnesian than kimberlite elsewhere on the NAC (e.g. Nielsen et al., 2009) that are buffered at $Fe_T^{2+}/ Fe_T^{2+} + Mg$ at ~ 0.6 (i.e. T1 'magnesian ulvöspinel trend'; Mitchell, 1995) at increasing TiO_2 and Al_2O_3 content (Figure. 16).

5.2.3. Phlogopite

Representative phlogopite mineral analyses are provided in Table. 7. Phlogopite compositions of both UML are similar to the range of compositions reported for UML elsewhere on the NAC (Nielsen et al., 2009). Phlogopite from Pyramidefjeld are generally comprised of distinct core and rims by chemical composition. The core comprised of ~18 wt. % Al_2O_3 and ~3 wt. % TiO_2 and rims that evolve to distinctly lower Al_2O_3 and TiO_2 contents ranging from ~16 – 11 wt. % and 2.5 – 1.0 wt. % respectively at more or less constant Mg# of ~85. Such a trend is typical for UML and atypical of kimberlite which display phlogopite that evolve from constant to higher Al_2O_3 contents from core to rim. By contrast, groundmass phlogopite from Nigerdlikasik evolve at either near-constant; or to more enriched Al_2O_3 concentrations, from core to rim but at higher TiO_2 contents comparative to phlogopite from Maniitsoq kimberlites (Figure. 17) and outside the kimberlite field of Mitchell, (1995). Mg# in phlogopite from Nigerdlikasik display greater variability and are generally higher ~87, although the ranges of core and rim compositions overlap. Mg# compositions overlap Sarfartoq UML and fall within the range of Mg# reported for phlogopite within

Location:	Pyramid	Pyramid	Pyramid	Pyramid	Pyramid	Pyramid	Nigerd	Nigerd
Sample:	PA-01	PA-01	PA-01	PA-01	PA-01	PA-01	NA-01	NA-01
Mineral:	Spn-1	Spn-1	Spn-5	Spn-5	Spn-9	Spn-9	Spn-6	Spn-6
Zone:	core	rim	core	rim	core	rim	core	rim
SiO_2	0.18	0.08	0.00	0.00	0.21	0.32	0.16	1.13
TiO_2	4.30	15.06	2.38	16.89	3.93	16.79	5.15	8.06
Al_2O_3	12.23	5.48	10.36	6.33	11.40	6.19	7.49	4.14
Cr_2O_3	42.21	0.75	48.29	0.36	44.55	0.49	47.44	0.38
FeO_t	26.82	60.35	26.27	59.13	27.27	59.87	25.46	67.16
MnO	0.00	0.66	0.65	0.59	0.29	0.40	0.27	0.67
NiO	0.00	0.00	0.00	0.00	0.25	0.13	0.11	0.12
MgO	11.43	10.05	10.93	11.38	11.22	11.42	12.76	9.81
CaO	0.00	0.31	0.00	0.16	0.00	0.10	0.11	0.86
Total	97.16	92.73	98.88	94.83	99.12	95.71	98.94	92.33
Si	0.05	0.02	0.00	0.00	0.06	0.09	0.04	0.32
Ti	0.86	3.21	0.47	3.49	0.77	3.44	1.02	1.72
Al	3.81	1.83	3.23	2.05	3.51	1.98	2.33	1.39
Cr	8.83	0.17	10.08	0.08	9.21	0.11	9.89	0.09
Fe^{3+}	1.55	6.82	1.51	6.45	1.51	6.57	1.42	8.89
Fe^{2+}	4.39	7.48	4.29	7.12	4.45	7.05	4.19	7.04
Mn	0.00	0.13	0.12	0.11	0.05	0.08	0.05	0.13
Ni	0.00	0.00	0.00	0.00	0.05	0.03	0.02	0.03
Mg	4.51	4.25	4.30	4.65	4.37	4.63	5.01	4.14
Mg#	43.17	22.90	42.58	25.54	42.31	25.37	47.19	20.65
Ca	0	0	0	0	0.00	0.03	0.03	0.26
Cations	24	24	24	24	24	24	24	24

Table 6: Representative major element analyses of groundmass spinel from UML at Nigerdlikasik (Nigerd') and Pyramidefjeld (Pyramid') by energy-dispersive X-ray spectroscopy via scanning electron microscope (SEM-EDX). Mg # - (Mg / Mg + Fe) x 100. Total iron is reported as Fe^{2+}. Fe^{3+} calculated from stoichiometry assuming full occupancy of the B^{3+} site. Cations normalized to 32 oxygen.

Location:	Nigerd	Nigerd	Nigerd	Nigerd	Nigerd	Nigerd	Nigerd	Nigerd
Sample:	NA-01	NA-01	NA-01	NA-01	NA-01	NA-01	NA-01	NA-01
Mineral:	Spn-4	Spn-4	Spn-5	Spn-5	Spn-7	Spn-7	Spn-1	Spn-3
Zone:	core	rim	core	rim	core	rim	core	core
SiO2	0.00	0.30	0.00	0.26	0.39	0.29	0.07	0.14
TiO2	3.80	17.23	7.04	17.74	19.42	3.81	4.13	5.84
Al2O3	9.88	11.07	10.01	9.93	8.60	44.08	9.87	9.52
Cr2O3	48.61	0.29	38.70	0.00	0.05	0.77	47.63	45.68
FeO*	23.35	50.62	28.21	51.15	51.42	30.39	23.03	23.78
MnO	0.40	0.53	0.16	0.56	0.46	0.25	0.19	0.53
NiO	0.00	0.00	0.00	0.00	0.13	0.11	0.14	0.00
MgO	13.10	15.42	13.47	14.54	15.01	19.93	13.26	13.33
CaO	0.03	0.03	0.05	0.20	0.12	0.21	0.30	0.00
Total	99.18	95.50	97.65	94.38	95.61	99.84	98.62	98.83
No. oxygens	32	32	32	32	32	32	32	32
Si	0.00	0.08	0.00	0.07	0.10	0.06	0.02	0.04
Ti	0.74	3.37	1.39	3.54	3.85	0.62	0.81	1.15
Al	3.03	3.39	3.09	3.11	2.67	11.20	3.03	2.93
Cr	9.99	0.06	8.02	0.00	0.01	0.13	9.82	9.42
$Fe^{3+\dagger}$	1.31	5.42	1.98	5.19	5.09	2.99	1.00	1.10
$Fe^{2+\dagger}$	3.77	5.59	4.21	6.18	6.24	2.49	4.02	4.09
Mn	0.07	0.10	0.03	0.10	0.08	0.04	0.03	0.10
Ni	0.00	0.00	0.00	0.00	0.03	0.02	0.03	0.00
Mg	5.08	5.98	5.26	5.76	5.89	6.41	5.15	5.18
Mg#	50.00	35.19	45.98	33.63	34.22	53.90	50.65	49.98
Ca	0.01	0.01	0	0	0	0	0	0
Total cations	24	24	24	24	24	24	24	24

Table 6: *continued*

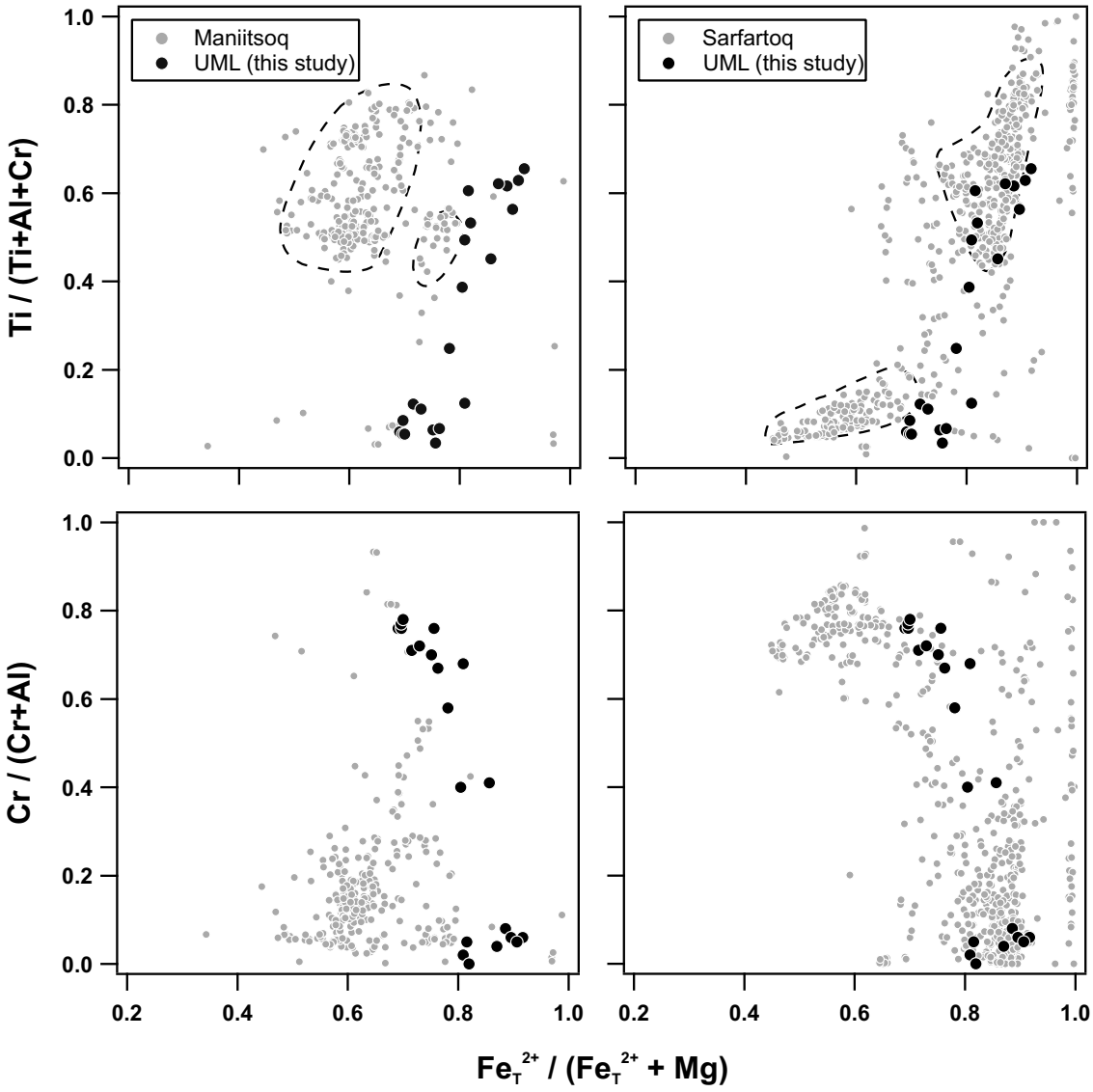

Figure 16: Ti / (Ti + Al +Cr) and Cr / (Cr + Al) vs Fe_T^{2+} / (Fe_T^{2+} + Mg) for groundmass spinel from ultramafic lamprophyre (UML) for Nigerdlikasik and Pyramidefjeld. Panels a) and b) show kimberlitic spinel from Maniitsoq for comparison, and Panels c) and d) show UML spinel from Sarfartoq. Data (grey) from supplementary database of Nielsen et al., (2009) with a dashed field displaying areas of main density.

Location:	Nigerd	Nigerd	Nigerd	Nigerd	Nigerd	Nigerd	Nigerd	Nigerd
Sample:	NA-01	NA-03	NA-02	P3580-1	P3580-1	NA-04	NA-05	NA-06
Mineral:	Phl-1	Phl-6	Phl-6	Phl-7	Phl-7	Phl-8	Phl-8	Phl-9
Zone:	core	core	rim	core	rim	core	rim	core
SiO_2	36.64	36.16	33.16	34.46	34.12	37.06	34.98	36.53
TiO_2	3.86	3.91	3.39	3.34	3.54	4.27	2.66	4.23
Al_2O_3	17.00	16.38	18.43	18.42	18.33	15.90	16.45	16.63
Cr_2O_3	0.13	0.90	0.00			0.34		0.57
FeO_t	5.96	4.73	5.07	6.24	6.06	5.43	7.17	4.97
MnO	0.00	0.00	0.00	0.08	0.07	0.05	0.05	0.00
NiO	0.00	0.00	0.12	0.04	0.06	0.03	0.09	0.06
MgO	21.62	21.53	21.10	21.31	21.33	21.84	22.63	21.72
CaO	0.06	0.17	0.13	0.19	0.19	0.11	0.17	0.15
Na_2O	0.25	0.20	0.17	0.25	0.23	0.34	0.18	0.28
K_2O	9.04	8.97	8.24	8.58	8.58	8.98	8.27	8.91
F	-	-	-	-	-	-	-	-
Cl	-	-	-	-	-	-	-	-
H_2O	4.54	4.07	3.93	4.04	4.02	4.12	4.02	4.12
Total	94.56	92.96	89.80	92.91	92.51	94.36	92.65	94.05
Total+H_2O	99.10	97.03	93.73	96.95	96.53	98.48	96.66	98.16

Location:	Pyramid	Pyramid	Pyramid	Pyramid	Pyramid	Pyramid	Pyramid	Pyramid
Sample:	PA-01	PA-01	PA-01	PA-01	PA-01	PA-01	PA-01	PA-01
Mineral:	Phl-2	Phl-2	Phl-3	Phl-3	Phl-4	Phl-4	Phl-5	Phl-5
Zone:	core	rim	core	rim	core	rim	core	rim
SiO_2	35.28	35.90	34.80	36.60	36.00	36.95	34.82	36.51
TiO_2	2.74	2.37	3.13	1.41	2.64	2.21	3.22	2.44
Al_2O_3	17.26	16.35	18.03	12.68	17.21	15.78	18.26	16.54
Cr_2O_3			0.01	0.04	0.01	0.06		0.05
FeO_t	6.54	6.55	6.94	9.36	6.69	6.43	6.88	6.59
MnO	0.10	0.10	0.10	0.11	0.13	0.10	0.12	0.08
NiO	0.04	0.04	0.00	0.04	0.04	0.02	0.04	0.04
MgO	21.32	21.76	21.37	24.59	21.78	22.59	20.88	22.44
CaO	0.12	0.13	0.13	0.08	0.13	0.19	0.12	0.15
Na_2O	0.29	0.32	0.28	0.25	0.33	0.31	0.33	0.35
K_2O	8.85	8.72	8.64	7.28	8.94	8.99	8.84	8.87
F	-	-	-	-	-	-	-	-
Cl	-	-	-	-	-	-	-	-
H_2O	4.02	4.01	4.05	3.98	4.08	4.07	4.05	4.09
Total	92.51	92.26	93.43	92.41	93.92	93.60	93.50	94.07
Total+H_2O	96.53	96.27	97.48	96.39	98.00	97.67	97.55	98.16

Table 7: Representative major element analyses of groundmass phlogopite from ultramafic lamprophyre (UML) at Nigerdlikasik (Nigerd) and Pyramidefjeld (Pyramid) by energy-dispersive X-ray spectroscopy via scanning electron microscope (SEM-EDX). Total iron is reported as Fe^{2+}. H_2O calculated from stoichiometry assuming no F and Cl contents since neither was analyzed.

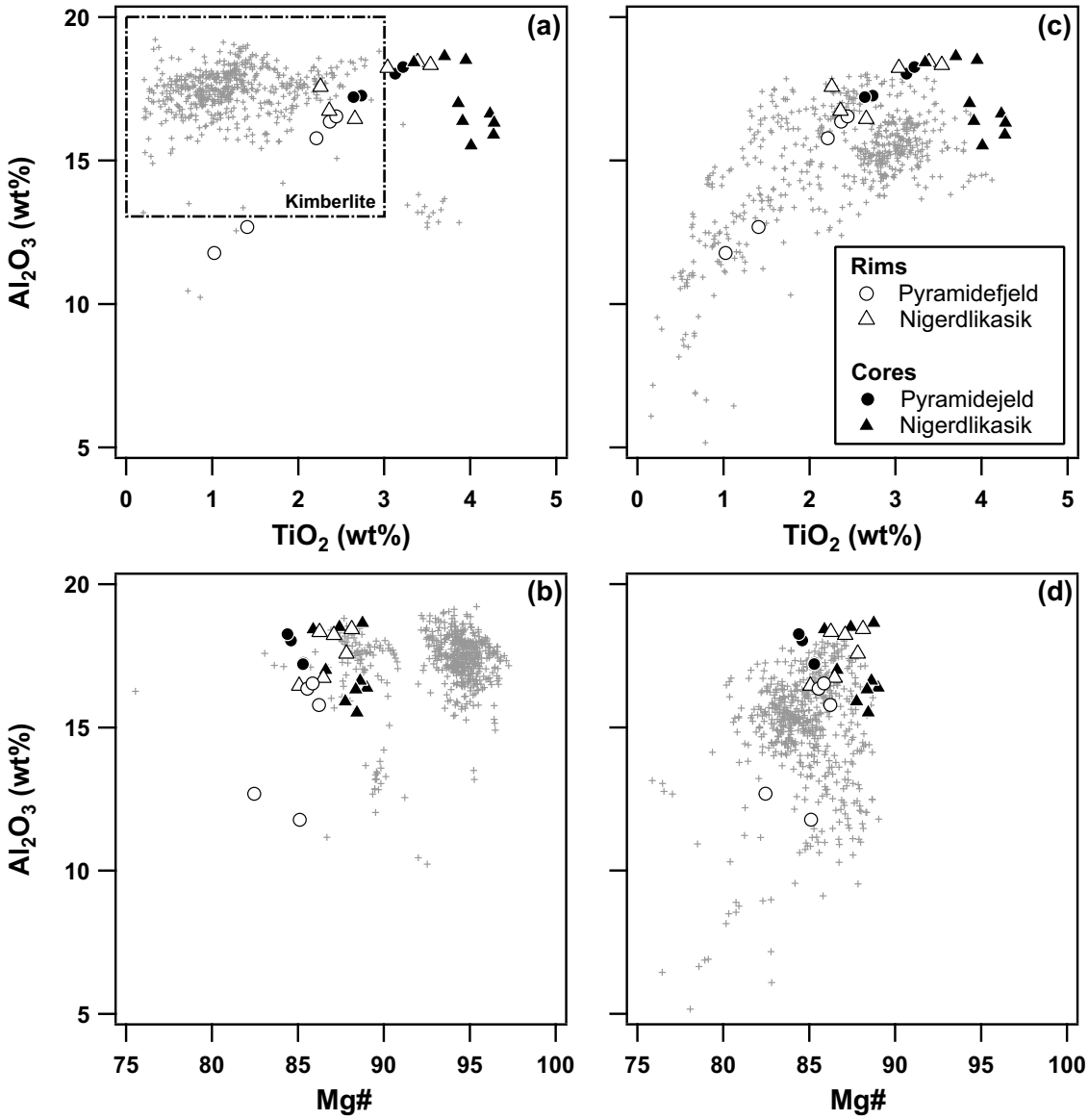

Figure 17: TiO_2 and Al_2O_3 vs Mg# (Mg / Mg + Fe) for groundmass phlogopite from ultramafic lamprophyre (UML) at Nigerdlikasik and Pyramidefjeld. Panels a) and b) show kimberlitic phlogopite from Maniitsoq, and Panels c) and d) show UML phlogopite from Sarfartoq. Data from supplementary database of Nielsen et al., (2009). Kimberlite field in Panel a) after Mitchell, (1995).

Maniitsoq kimberlites, although these are commonly more magnesian (Mg# ~95). Rim overgrowths are common displaying the low Mg# of ~82. Rim compositions therefore reflect higher FeO at the expense of TiO_2 and MgO contents.

5.3. Xenolith major and trace element mineral chemistry

5.3.1. Olivine

Olivine mineral analyses are provided in Table. 8 and illustrated in Figure. 18. Olivine within mantle xenoliths span a range of Mg# from 84 to 92 covering the range observed in macrocryst olivine cores recovered from both UML. The majority of the xenoliths display olivine with Mg# between 88 and 90. The highest Mg# in olivine occurs within one sample (NX-07), a granular harzburgite, and the sample with the lowest modal olivine abundance (Figure. 18). The lowest Mg# (~84) in olivine is seen in sample NX-08 in relict olivine surrounded by recrystallized neoblastic olivine (Mg# ~88). NiO contents range from 0.3 to 0.4 wt. %.

5.3.2. Clinopyroxene

Clinopyroxene major and trace element analyses for selected xenoliths from Nigerdlikasik are reported in Table. 9a and b. Clinopyroxene compositions are chrome-diopside with ~0.8 – 2.4 wt. % Cr_2O_3, 21 - 22 wt. % CaO and 0.9 - 1.5 wt. % Na_2O. TiO_2 and Al_2O_3 contents are fairly low at ~ 0.02 wt. % and 0.4 – 0.8 wt. % respectively. Clinopyroxenes appear largely homogenous with little variation between repeat analyses within each xenolith. However, the granular harzburgite xenolith (NX-07), which displays the lowest modal olivine abundance and highest Mg#, displays greater variability in TiO_2 (up to 1.5 wt. %) and Al_2O_3 (up to 4.5 wt. %). Mg# is high in all analysed clinopyroxene, reflecting low FeO contents, ranging from 94 to 97 with no trivalent Fe substitution observed. In terms of CaO, TiO_2, Cr_2O_3 and Mg#, clinopyroxene compositions for all xenoliths fall within those reported for cratonic mantle peridotites (Grégoire et al., 2002; Grégoire et al., 2003; le Roex and Class, 2016) and comparable to clinopyroxene of the PIC assemblage (e.g. Gregoire et al., 2003).

Two xenolith samples (NX-02 and NX-03) from Nigerdlikasik were analysed for trace elements via LA-ICP-MS and illustrated in Figure. 19 on primitive- and chondrite-normalised trace element variation diagrams. Incompatible elements are generally fairly similar in concentration and profile between the two analysed xenoliths (e.g. Zr = ~ 60

Location	Nigerd	Nigerd	Nigerd	Nigerd	Nigerd	Nigerd	Nigerd	Nigerd
Sample	NX-04	NX-04	NX-02	NX-02	NX-05	NX-05	NX-03	NX-03
Mineral	Ol-3	Ol-5	Ol-8	Ol-10	Ol-11	Ol-14	Ol-16	Ol-17
SiO_2	39.89	40.17	40.12	40.10	39.95	39.71	39.66	39.62
TiO_2	0.03	0.06	0.02	0.03	0.01	0.04	0.04	0.06
Al_2O_3	0.02	0.04	0.00	0.10	0.05	0.02	0.07	0.06
Cr_2O_3	0.01	0.00	0.02	0.02	0.04	0.04	0.02	0.02
FeO	10.06	9.98	9.86	9.85	10.03	10.09	11.70	11.51
MnO	0.13	0.12	0.12	0.12	0.14	0.15	0.12	0.13
NiO	0.33	0.31	0.34	0.36	0.33	0.36	0.27	0.28
MgO	49.91	49.81	50.02	49.96	49.72	49.81	48.42	48.18
CaO	0.02	0.03	0.03	0.02	0.01	0.17	0.02	0.02
Na_2O	0.02	0.00	0.00	0.03	0.00	0.03	0.11	0.09
K_2O	0.00	0.00	0.02	0.00	0.03	0.02	0.01	0.01
Total	100.42	100.52	100.55	100.58	100.30	100.45	100.45	99.99
O	4.00	4.00	4.00	4.00	4.00	4.00	4.00	4.00
Si	0.98	0.98	0.98	0.98	0.98	0.98	0.98	0.98
Ti	0.00	0.00	0.00	0.00	0.00	0.00	0.00	0.00
Al	0.00	0.00	0.00	0.00	0.00	0.00	0.00	0.00
Cr	0.00	0.00	0.00	0.00	0.00	0.00	0.00	0.00
Fe	0.21	0.20	0.20	0.20	0.21	0.21	0.24	0.24
Mn	0.00	0.00	0.00	0.00	0.00	0.00	0.00	0.00
Ni	0.01	0.01	0.01	0.01	0.01	0.01	0.01	0.01
Mg	1.82	1.82	1.82	1.82	1.82	1.82	1.78	1.78
Mg#	89.84	89.89	90.04	90.04	89.83	89.80	88.06	88.18
Ca	0.00	0.00	0.00	0.00	0.00	0.00	0.00	0.00
Na	0.00	0.00	0.00	0.00	0.00	0.00	0.01	0.00
K	0.00	0.00	0.00	0.00	0.00	0.00	0.00	0.00
Cations	3.02	3.02	3.02	3.02	3.02	3.02	3.02	3.02

Table 8: Representative major element analyses of olivine from xenoliths recovered from ultramafic lamprophyre (UML) at Nigerdlikasik (Nigerd) and Pyramidefjeld (Pyramide) by energy-dispersive X-ray spectroscopy via scanning electron microscope (SEM-EDX). Mg# - (Mg / Mg + Fe) x 100. Cations normalized to 4 oxygen.

Location	Nigerd	Nigerd	Nigerd	Nigerd	Nigerd	Nigerd	Pyramid	Pyramid
Sample	NX-03	NX-07	NX-08	NX-08	NX-01	NX-01	PX-01	PX-01
Mineral	Ol-20	Ol-25	Ol-28	Ol-31	Ol-34	Ol-35	Ol-41	Ol-42
SiO_2	39.63	40.26	38.84	39.68	40.00	40.11	40.54	40.34
TiO_2	0.06	0.02	0.04	0.02	0.00	0.00	0.00	0.00
Al_2O_3	0.14	0.11	0.06	0.09	0.00	0.00	0.00	0.00
Cr_2O_3	0.02	0.00	0.02	0.04	0.00	0.00	0.00	0.00
FeO	11.51	7.96	15.04	10.30	9.35	9.52	9.25	9.32
MnO	0.12	0.09	0.19	0.11	0.09	0.07	0.13	0.16
NiO	0.29	0.39	0.30	0.40	0.35	0.34	0.35	0.38
MgO	48.22	51.17	45.06	49.38	49.50	49.53	50.12	50.05
CaO	0.01	0.01	0.03	0.07	0.02	0.00	0.00	0.00
Na_2O	0.09	0.12	0.13	0.13	0.00	0.00	0.00	0.00
K_2O	0.02	0.01	0.01	0.02	0.00	0.00	0.00	0.00
Total	100.11	100.14	99.71	100.24	99.30	99.57	100.39	100.24
O	4.00	4.00	4.00	4.00	4.00	4.00	4.00	4.00
Si	0.98	0.98	0.98	0.98	0.99	0.99	0.99	0.99
Ti	0.00	0.00	0.00	0.00	0.00	0.00	0.00	0.00
Al	0.00	0.00	0.00	0.00	0.00	0.00	0.00	0.00
Cr	0.00	0.00	0.00	0.00	0.00	0.00	0.00	0.00
Fe	0.24	0.16	0.32	0.21	0.19	0.20	0.19	0.19
Mn	0.00	0.00	0.00	0.00	0.00	0.00	0.00	0.00
Ni	0.01	0.01	0.01	0.01	0.01	0.01	0.01	0.01
Mg	1.78	1.86	1.70	1.81	1.82	1.82	1.82	1.83
Mg#	88.19	91.97	84.23	89.53	90.42	90.27	90.62	90.54
Ca	0.00	0.00	0.00	0.00	0.00	0.00	0.00	0.00
Na	0.00	0.01	0.01	0.01	0.00	0.00	0.00	0.00
K	0.00	0.00	0.00	0.00	0.00	0.00	0.00	0.00
Cations	3.02	3.02	3.02	3.02	3.01	3.01	3.01	3.01

Table 8: *continued*

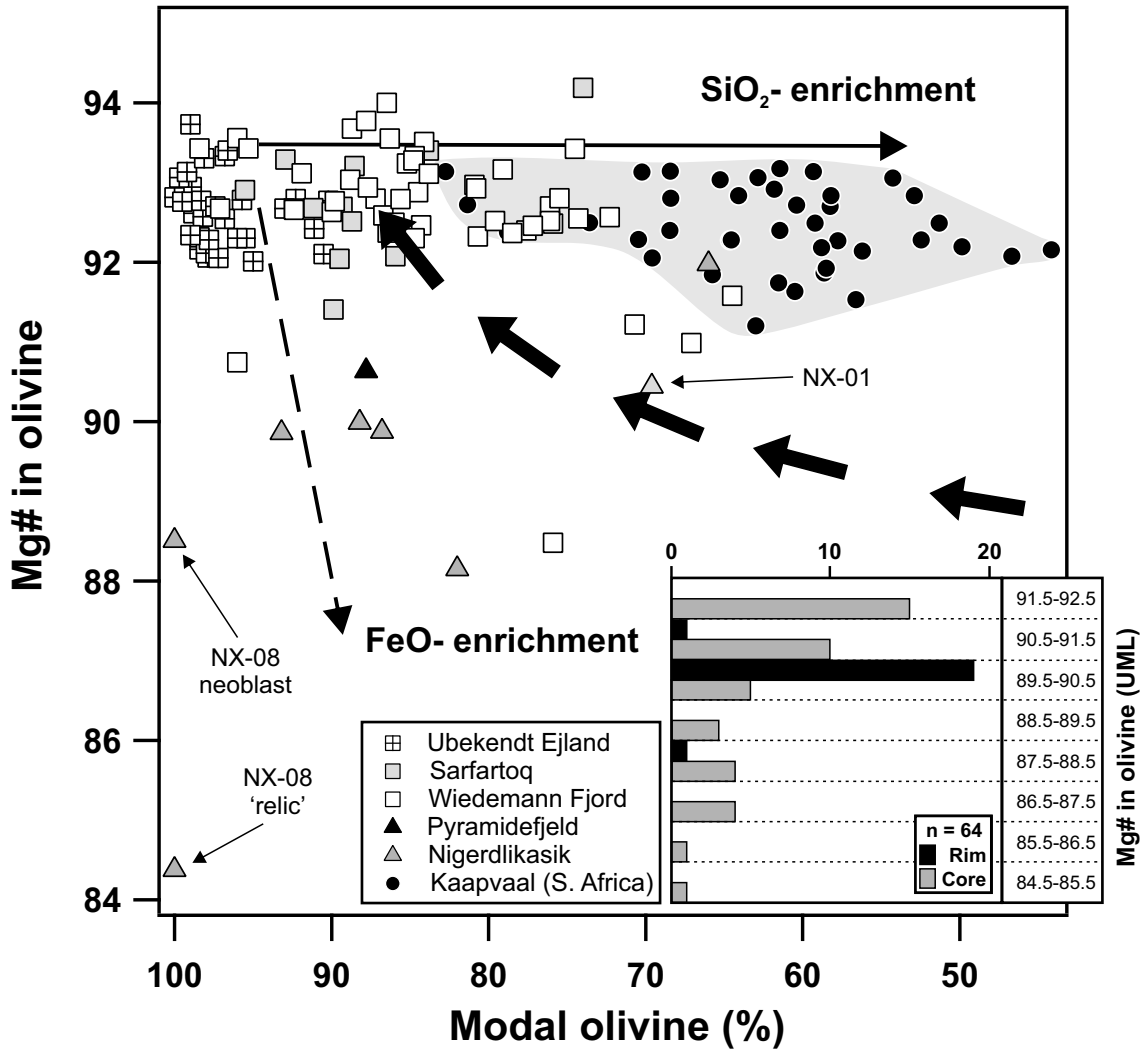

Figure 18: Mg# in olivine vs modal (%) olivine in xenolith recovered from ultramafic lamprophyre (UML) for Nigerdlikasik and Pyramidefjeld compared to C-SCLM xenoliths from Greenland: Ubekendt Eijand (Bernstein et al., 2006); Wiedermann Fjord (Bernstein et al., 1998); Sarfartoq (Garrit, 2002) and Kaapvaal (Boyd, 1999). Schematic melting curve from Boyd, (1989).

Location	Nigerd	Nigerd	Nigerd	Nigerd	Nigerd	Nigerd	Nigerd	Nigerd
Sample	NX-04	NX-04	NX-02	NX-02	NX-05	NX-05	NX-03	NX-03
Mineral	Cpx-1	Cpx-4	Cpx-7	Cpx-9	Cpx-13	Cpx-14	Cpx-23	Cpx-24
SiO_2	54.94	54.71	54.56	54.56	54.76	54.90	54.21	52.50
TiO_2	0.19	0.19	0.17	0.21	0.19	0.17	0.17	1.51
Al_2O_3	0.43	0.43	0.46	0.43	0.44	0.45	0.62	0.72
Cr_2O_3	1.32	1.79	1.97	1.16	1.83	1.81	1.07	0.83
MgO	17.65	17.49	17.27	17.74	17.36	17.37	17.34	17.52
FeO_t	2.61	2.64	2.40	2.47	2.44	2.56	3.07	2.53
MnO	0.06	0.05	0.07	0.10	0.08	0.07	0.09	0.08
NiO	0.04	0.04	0.04	0.05	0.05	0.05	0.02	0.01
CaO	21.92	21.55	21.38	21.74	21.71	21.61	21.28	23.03
Na_2O	1.04	1.21	1.28	1.00	1.17	1.23	1.17	0.44
K_2O	0.02	0.01	0.01	0.01	0.02	0.02	0.04	0.05
Total	100.20	100.09	99.61	99.46	100.05	100.24	99.07	99.21
O	6.00	6.00	6.00	6.00	6.00	6.00	6.00	6.00
Si	1.98	1.98	1.98	1.98	1.98	1.98	1.98	1.93
Al IV	0.02	0.02	0.02	0.02	0.02	0.02	0.02	0.03
Fe^{3+}	0.00	0.00	0.00	0.00	0.00	0.00	0.00	0.04
T-site	2.00	2.00	2.00	2.00	2.00	2.00	2.00	2.00
Al VI	0.00	0.00	0.00	0.00	0.00	0.00	0.01	0.00
Fe^{3+}	0.04	0.04	0.04	0.04	0.03	0.04	0.06	0.00
Cr	0.04	0.05	0.06	0.03	0.05	0.05	0.03	0.02
Ti	0.01	0.01	0.00	0.01	0.01	0.00	0.00	0.04
Mg	0.92	0.90	0.90	0.92	0.91	0.90	0.90	0.93
Fe^{2+}	0.00	0.00	0.00	0.00	0.00	0.00	0.00	0.00
Ni	0.00	0.00	0.00	0.00	0.00	0.00	0.00	0.00
Mn	0.00	0.00	0.00	0.00	0.00	0.00	0.00	0.00
M1-site	1.00	1.00	1.00	1.00	1.00	1.00	1.00	1.00
Mg	0.03	0.04	0.04	0.04	0.03	0.03	0.04	0.03
Fe^{2+}	0.04	0.03	0.04	0.03	0.04	0.04	0.03	0.03
Ni	0.00	0.00	0.00	0.00	0.00	0.00	0.00	0.00
Mn	0.00	0.00	0.00	0.00	0.00	0.00	0.00	0.00
Ca	0.85	0.84	0.83	0.85	0.84	0.84	0.83	0.91
Na	0.07	0.09	0.09	0.07	0.08	0.09	0.08	0.03
K	0.00	0.00	0.00	0.00	0.00	0.00	0.00	0.00
M2-site	1.00	1.00	1.00	1.00	1.00	1.00	1.00	1.00
Cations	4.00	4.00	4.00	4.00	4.00	4.00	4.00	4.00
Mg#	96.06	95.05	95.96	95.72	96.25	95.84	93.85	95.64

Table 9a: Representative major element analyses of clinopyroxene from xenoliths recovered from ultramafic lamprophyre (UML) at Nigerdlikasik (Nigerd) and Pyramidefjeld (Pyramide) via energy-dispersive X-ray spectroscopy by scanning electron microscope (SEM-EDX). Mg# - (Mg / Mg + Fe) x 100. Cations normalized to 6 oxygen.

Location	Nigerd	Nigerd	Pyramid	Pyramid
Sample	NX-07	NX-07	PX-01	PX-01
Mineral	Cpx-25	Cpx-26	Cpx-28	Cpx-30
SiO_2	52.65	53.76	55.15	55.52
TiO_2	0.22	0.19	0.04	0.03
Al_2O_3	4.45	0.82	0.20	0.19
Cr_2O_3	1.35	2.16	1.30	1.43
MgO	15.43	16.88	17.22	17.31
FeO_t	1.51	2.71	2.32	2.06
MnO	0.05	0.08	0.06	0.00
NiO	0.10	0.07	0.00	0.00
CaO	20.82	20.37	22.42	22.81
Na_2O	1.80	1.40	0.90	0.92
K_2O	0.02	0.02	0.00	0.00
Total	98.40	98.43	99.61	100.27
O	6.00	6.00	6.00	6.00
Si	1.93	1.98	2.01	2.01
Al IV	0.07	0.02	0.00	0.00
Fe^{3+}	0.00	0.00	0.00	0.00
T-site	2.00	2.00	2.01	2.01
Al VI	0.12	0.01	0.01	0.01
Fe^{3+}	0.03	0.03	0.00	0.00
Cr	0.04	0.06	0.04	0.04
Ti	0.01	0.01	0.00	0.00
Mg	0.80	0.88	0.93	0.93
Fe^{2+}	0.00	0.00	0.02	0.02
Ni	0.00	0.00	0.00	0.00
Mn	0.00	0.00	0.00	0.00
M1-site	1.00	1.00	1.00	1.00
Mg	0.04	0.04	0.00	0.00
Fe^{2+}	0.01	0.05	0.05	0.05
Ni	0.00	0.00	0.00	0.00
Mn	0.00	0.00	0.00	0.00
Ca	0.82	0.80	0.87	0.88
Na	0.13	0.10	0.06	0.06
K	0.00	0.00	0.00	0.00
M2-site	1.00	1.00	0.99	0.99
Cations	4.00	4.00	4.00	4.00
Mg#	96.05		99.74	99.92

Table 9a: *continued*

Location	Nigerd	Nigerd	Nigerd	Nigerd	Nigerd	Nigerd
Sample	NX-02	NX-02	NX-02	NX-02	NX-02	NX-02
Mineral	Cpx-7	Cpx-8	Cpx-9	Cpx-10	Cpx-11	Cpx-12
SiO_2	54.56	54.44	54.56	54.43	54.41	54.49
TiO_2	0.17	0.19	0.21	0.19	0.19	0.21
Al_2O_3	0.46	0.47	0.43	0.45	0.43	0.42
Cr_2O_3	1.97	1.29	1.16	1.36	1.35	0.97
MgO	17.27	17.51	17.74	17.57	17.59	17.83
FeO_t	2.40	2.44	2.47	2.41	2.42	2.52
MnO	0.07	0.07	0.10	0.07	0.03	0.06
NiO	0.04	0.08	0.05	0.02	0.07	0.05
CaO	21.38	21.75	21.74	21.77	21.66	21.79
Na_2O	1.28	1.04	1.00	1.03	1.00	0.87
K_2O	0.01	0.01	0.01	0.01	0.01	0.01
Total	99.61	99.29	99.46	99.31	99.17	99.20
K	120.7	38.1	158	107.5	372	166
Sc	51.8	50.9	48.12	60.8	34.93	36.86
Ti	242.6	239.9	276.3	249.5	243.6	239
V	287	267	220.8	348	268	270
Co	18.41	17.33	18.03	17.72	18.04	18.99
Ni	306.3	297.1	309	304.7	304	309.9
Rb	0.638	< LOD	0.95	0.383	2.12	0.441
Sr	286	294	186	306	345	305
Y	4.77	4.24	3.784	4.97	5.73	5.04
Zr	63.1	59.1	53.1	63.9	84	57
Nb	0.399	0.241	0.378	0.543	0.83	0.843
Cs	0.0138	< LOD	0.071	0.0136	0.136	0.05
Ba	1.18	0.232	4.44	2.05	0.67	< LOD
La	2.954	2.8	2.74	3.072	3.78	3.91
Ce	13.9	12.51	11.61	14.32	16.59	16.14
Nd	14.44	13.48	11.22	15.1	16.7	16.25
Sm	3.5	3.16	2.72	3.63	4.16	3.77
Gd	2.52	2.37	1.86	2.56	3.03	2.78
Dy	1.54	1.435	1.19	1.697	1.91	1.77
Er	0.409	0.389	0.389	0.431	0.537	0.469
Yb	0.191	0.16	0.149	0.192	0.255	0.183
Hf	3.37	3.45	3.12	3.56	4.19	3.3
Ta	0.0198	0.013	0.0177	0.0169	0.0164	0.0364

Table 9b: Major and trace element analyses for clinopyroxene in xenolith samples NX-02 and NX-03. Trace elements were collected by laser-ablation inductively-coupled plasma-spectrometry (LA-ICP-MS). < LOD are analyses below the limit of detection.

Location	Nigerd	Nigerd	Nigerd
Sample	NX-03	NX-03	NX-03
Mineral	Cpx-21	Cpx-22	Cpx-23
SiO2	53.97	53.29	54.21
TiO2	0.15	0.66	0.17
Al2O3	0.70	0.77	0.62
Cr2O3	1.84	1.19	1.07
MgO	16.69	17.71	17.34
FeOt	2.89	3.17	3.07
MnO	0.09	0.09	0.09
NiO	0.06	0.06	0.02
CaO	20.81	20.88	21.28
Na2O	1.37	0.79	1.17
K2O	0.01	0.04	0.04
Total	98.57	98.64	99.07
K	30.6	108.1	130.7
Sc	55.5	63.8	64.8
Ti	203	209.9	216.2
V	436	505	509
Co	17.89	17.55	17.84
Ni	261	250	253.7
Rb	0.221	0.728	0.663
Sr	530	478	473
Y	5.18	5.46	5.69
Zr	43	61.3	62.2
Nb	0.195	0.236	0.183
Cs	0.0195	0.107	0.0356
Ba	0.61	0.505	0.266
La	9.47	6.35	6.51
Ce	35	27.19	27.16
Nd	23.3	22.13	22.66
Sm	4.18	4.53	4.78
Gd	3.02	3.04	3.08
Dy	1.61	1.783	1.81
Er	0.471	0.48	0.515
Yb	0.23	0.242	0.291
Hf	3.01	3.94	3.97
Ta	0.0056	0.0066	0.0082

Table 9b: *continued*

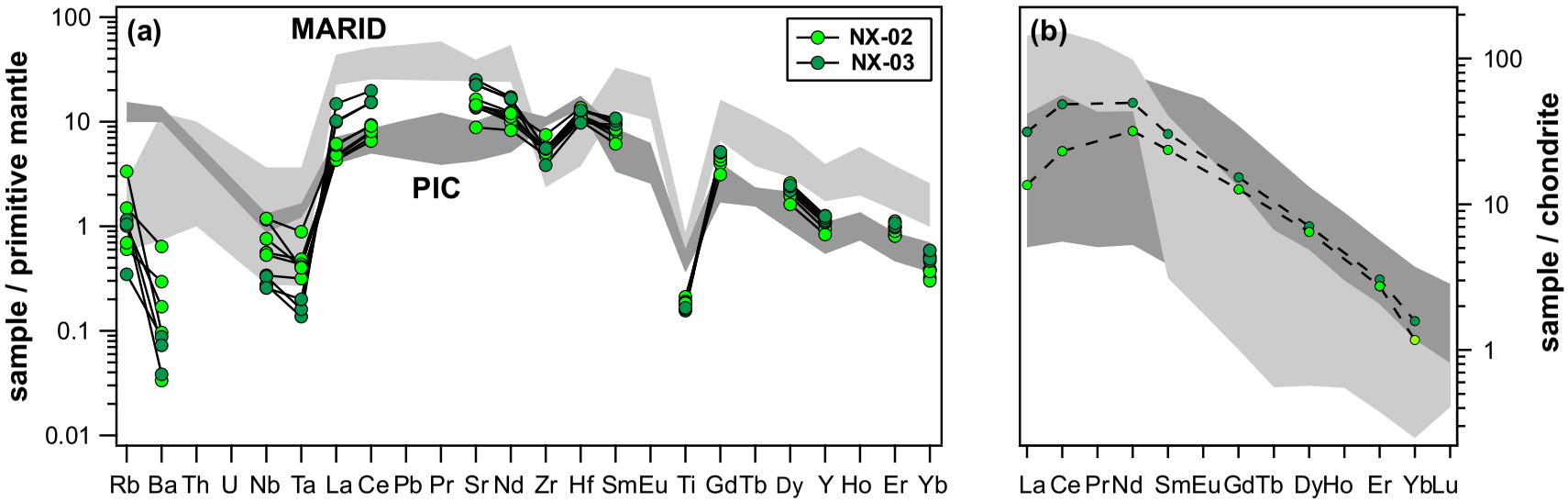

Figure 19: Incompatible and rare-Earth element (REE) trace element variation diagrams for clinopyroxene from C-SCLM xenoliths recovered from xenoliths (NX-02 NX-03) from ultramafic lamprophyre (UML) from Nigerdlikasik. Panel (a) normalized against primitive mantle of Sun and McDonough (1989). Panel (b) REE normalized against chondrite of McDonough and Sun, (1995). Dark grey field displays range of compositions of Type-I type clinopyroxene of the phlogopite-ilmenite-clinopyroxene (PIC) assemblage of Grégoire et al., (2002). Dark grey field displaying range of compositions of mica (phlogopite)-amphibole (K-richterite)-rutile-ilmenite-diopside assemblage of Dawson and Smith (1977) from Grégoire et al., (2002).

p.p.m.; Hf = ~ 3 – 4; Y = ~ 5.5 p.p.m.) although NX-02 is more enriched in Nb-Ta, Sr-Nd and Ce-Pb than NX-03. Respective Nb/La ratios of 0.03 and 0.1 show that relative Nb/Ta depletion is more significant for clinopyroxene in sample NX-03 than NX-02. Both traces display noticeable Zr and Ti anomalies (Figure. 19). Mantle compatible elements (Sc = ~60 p.p.m.; Co = 17 – 19 p.p.m.; Ni = 250 – 300 p.p.m.) are similar but large variation is observed between NX-02 and NX-03 in terms of V, with concentrations of ~280 and ~500 p.p.m. respectively. The range in FME is also more variable between clinopyroxene in both xenoliths (e.g. Sr = ~180 – 530 p.p.m.; Ba = ~ 0.6 – 8 p.p.m.) but no systematic differences between the xenoliths are observed. In contrast to other incompatible elements, clinopyroxene in sample NX-03 is slightly more enriched in REE than clinopyroxene in sample NX-02 as illustrated by La/Yb ratios of ~ 30 and 17 respectively. REE trace patterns are convex up peaking at Ce-Nd. As seen in major element compositions, REE systematics in clinopyroxene from both xenoliths closely mirror those classified as belonging to the PIC assemblage (e.g. Grégoire et al., 2002). However, the strong Zr, Ti and Nb-Ta depletions are comparative to MARID clinopyroxene and are atypical of PIC clinopyroxene, as are Nb/Ta and the low Rb concentrations. Both show a remarkable depletion in Ba relative to either PIC or MARID clinopyroxene, perhaps a result of co-crystallization of, or equilibrium with, surrounding phlogopite (as would be implied by petrographic observations).

5.3.3. Orthopyroxene

Representative major element compositions for orthopyroxene from C-SCLM xenoliths are reported in Table. 10. Orthopyroxene within NX-06, an orthopyroxenite xenolith, has the highest Al_2O_3, FeO and Cr_2O_3 contents of ~5.8 wt. %, 10.7 wt. % and 0.8 wt. % respectively of the three analysed xenoliths. The high FeO contents are reflected in an Mg# of ~83, unusually low for orthopyroxene within C-SCLM. The granular harzburgite (NX-05) and phlogopite harzburgite (NX-01) have major element compositions that broadly overlap compositions expected for C-SCLM.

5.3.4. Phlogopite

Representative phlogopite major and trace analyses for xenoliths are reported in Table. 11a, 11b and 11c as well as Figures. 20, 21 and 22. Phlogopite compositions from xenoliths recovered from UML at Nigerdlikasik are remarkably constant at ~12 wt. % Al_2O_3, ~1 wt. % TiO_2, ~0.5 wt. % Cr_2O_3 and ~9.5 wt. % K_2O. MgO contents are

Location	Nigerd	Nigerd	Nigerd	Nigerd	Nigerd	Nigerd
Sample	NX-06	NX-06	NX-05	NX-05	NX-01	NX-01
Mineral	En-2	En-4	En-7	En-8	En-11	En-12
SiO2	52.04	51.50	55.32	55.26	57.70	57.92
TiO2	0.03	0.04	0.07	0.04	0.08	0.18
Al2O3	5.84	5.72	3.10	2.93	0.93	0.76
Cr2O3	0.86	0.82	0.47	0.49	0.39	0.34
MgO	29.14	29.28	34.73	34.55	35.56	35.84
FeOt	10.70	10.65	5.16	5.20	5.81	5.86
NiO	0.19	0.18	0.09	0.09	0.08	0.05
MnO	0.14	0.11	0.12	0.11	0.16	0.15
CaO	0.66	0.22	0.64	0.60	0.44	0.43
Na2O	0.07	0.10	0.13	0.13	0.01	0.00
K2O	0.00	0.01	-	-	0.00	0.00
Total	99.67	98.64	99.84	99.40	101.17	101.52
O	6.00	6.00	6.00	6.00	6.00	6.00
Si	1.85	1.85	1.91	1.92	1.97	1.97
Ti	0.00	0.00	0.00	0.00	0.00	0.00
Al (T)	0.15	0.15	0.09	0.09	0.04	0.04
Al (M)	0.09	0.09	0.03	0.03	0.00	0.00
Cr	0.02	0.02	0.01	0.01	0.01	0.01
Mg	1.55	1.57	1.79	1.79	1.81	1.82
Mg#	82.93	83.06	92.30	92.22	91.60	91.60
Fe	0.32	0.32	0.15	0.15	0.17	0.17
Ni	0.01	0.01	0.00	0.00	0.00	0.00
Mn	0.00	0.00	0.00	0.00	0.00	0.00
Ca	0.03	0.01	0.02	0.02	0.02	0.02
Na	0.00	0.01	0.01	0.01	0.00	0.00
K	0.00	0.00	0.00	0.00	0.00	0.00
Total cations	4.02	4.02	4.02	4.02	4.01	4.02

Table 10: Representative major element analyses of orthopyroxene from xenoliths recovered from UML at Nigerdlikasik (Nigerd) by energy-dispersive X-ray spectroscopy via scanning electron microscope (SEM-EDX). Mg # - (Mg / Mg + Fe) x 100. Cations normalized to 6 oxygen.

Location	Nigerd	Nigerd	Nigerd	Nigerd	Nigerd	Nigerd	Nigerd	Nigerd
Sample	NX-03	NX-03	NX-02	NX-02	NX-04	NX-04	NX-05	NX-05
Mineral	Phl-1	Phl-4	Phl-6	Phl-7	Phl-12	Phl-13	Phl-17	Phl-18
SiO_2	41.46	41.47	41.54	41.47	41.43	41.36	41.60	41.45
TiO_2	0.96	1.02	1.03	1.05	1.03	1.01	1.06	1.07
Al_2O_3	12.32	12.43	12.12	12.19	12.13	12.12	12.19	12.06
Cr_2O_3	0.50	0.58	0.56	0.53	0.56	0.53	0.58	0.52
FeO_t	4.32	4.19	3.91	3.90	3.86	3.87	3.93	3.94
MnO	0.05	0.09		0.05	0.03	0.05	0.01	0.01
NiO	0.18	0.20	0.20	0.20	0.17	0.23	0.22	0.14
MgO	25.22	25.05	25.50	25.52	25.23	25.43	25.52	25.56
CaO	0.05	0.09	0.06	0.07	0.06	0.05	0.06	0.07
Na_2O	0.30	0.37	0.22	0.23	0.21	0.18	0.25	0.23
K_2O	9.39	9.32	9.54	9.46	9.48	9.33	9.45	9.62
F	-	-	-	-	-	-	-	-
Cl	-	-	-	-	-	-	-	-
H_2O	4.18	4.17	4.17	4.18	4.15	4.19	4.19	4.17
Total	94.74	94.81	94.66	94.67	94.18	94.16	94.87	94.66
Total+H_2O	98.91	98.98	98.83	98.85	98.34	98.35	99.06	98.84
#Mg	91.23	91.43	92.08	92.10	92.09	92.13	92.04	92.05

Location	Nigerd	Nigerd	Pyramid	Pyramid
Sample	NX-01	NX-04	PX-01	PX-01
Mineral	Phl-21	Phl-24	Phl-29	Phl-30
SiO_2	41.07	41.15	42.75	42.89
TiO_2	1.40	1.36	0.18	0.21
Al_2O_3	13.65	13.46	11.24	11.34
Cr_2O_3	1.15	1.12	0.22	0.20
FeO_t	3.75	3.77	4.26	4.35
MnO	0.00	0.00	0.00	0.00
NiO	0.08	0.22	0.09	0.11
MgO	25.02	25.23	26.95	27.13
CaO	0.13	0.13	0.04	0.00
Na_2O	0.33	0.34	0.22	0.18
K_2O	9.05	8.95	9.75	9.66
F	-	-	-	-
Cl	-	-	-	-
H_2O	4.22	4.23	4.21	4.23
Total	95.63	95.72	95.68	96.07
Total+H_2O	99.85	99.95	99.89	100.30
#Mg	92.25	92.26	91.86	91.75

Table 11a: Representative major element analyses of xenolithic phlogopite recovered from ultramafic lamprophyre (UML) at Nigerdlikasik (Nigerd) and Pyramidefjeld (Pyramid) by SEM-EDX. Total iron is reported as Fe^{2+}. H_2O calculated from stoichiometry assuming no F and Cl contents since neither was analyzed.

Location	Pyramid	Pyramid	Pyramid	Pyramid	Nigerd	Nigerd	Nigerd	Nigerd
Sample	PX-01	PX-01	PX-01	PX-01	NX-01	NX-01	NX-01	NX-01
Mineral	Phl-31	Phl-32	Phl-33	Phl-34	Phl-35	Phl-36	Phl-37	Phl-38
SiO_2	42.67	42.28	42.59	42.25	42.13	40.39	40.58	40.47
TiO_2	0.19	0.23	0.17	0.18	1.33	1.31	1.34	1.26
Al_2O_3	11.05	11.20	11.25	11.19	13.80	13.23	13.72	13.64
Cr_2O_3	-	-	-	-	-	-	-	-
FeO_t	3.78	3.80	3.62	3.69	3.30	3.38	3.46	3.54
MnO	0.02	0.02	0.01	0.00	0.06	0.00	0.03	0.02
NiO	-	-	-	-	-	-	-	-
MgO	25.70	26.01	25.80	25.76	23.84	23.48	23.81	23.81
CaO	0.00	0.00	0.00	0.01	0.01	0.00	0.01	0.00
Na_2O	0.20	0.26	0.20	0.19	0.38	0.33	0.40	0.39
K_2O	10.75	10.67	10.62	10.74	10.61	10.58	10.00	10.00
F	0.95	0.93	0.94	0.95	0.21	0.19	0.19	0.20
Cl	0.00	0.00	0.00	0.01	0.06	0.05	0.07	0.06
H_2O	3.71	3.72	3.72	3.69	4.11	3.98	4.02	3.98
Total	95.32	95.40	95.20	94.98	95.73	92.95	93.61	93.38
Total+H_2O	99.03	99.12	98.92	98.67	99.84	96.93	97.63	97.36
#Mg	92.37	92.42	92.69	92.56	92.80	92.53	92.46	92.31

Table 11b: Major element analyses (inc. F and Cl) of xenolithic phlogopite recovered from ultramafic lamprophyre (UML) at Nigerdlikasik (Nigerd) and Pyramidefjeld (Pyramid) by electron microprobe (EMPA). Total iron is reported as Fe^{2+}. H_2O calculated from stoichiometry.

Location	Nigerd	Nigerd	Nigerd	Nigerd	Nigerd	Nigerd	Nigerd	Nigerd
Sample	NX-03	NX-03	NX-03	NX-03	NX-03	NX-02	NX-02	NX-02
Mineral	Phl-1	Phl-2c	Phl-3	Phl-4	Phl-5	Phl-6	Phl-7	Phl-8
SiO_2	41.46	41.31	41.20	41.47	41.30	41.54	41.47	41.44
TiO_2	0.96	0.98	1.00	1.02	0.96	1.03	1.05	1.03
Al_2O_3	12.32	12.02	12.34	12.43	12.36	12.12	12.19	12.25
Cr_2O_3	0.50	0.51	0.56	0.58	0.56	0.56	0.53	0.54
FeO_t	4.32	4.53	4.36	4.19	4.29	3.91	3.90	3.89
MnO	0.05	0.03	0.06	0.09	0.01		0.05	0.03
NiO	0.18	0.01	0.19	0.20	0.18	0.20	0.20	0.20
MgO	25.22	25.17	25.20	25.05	25.18	25.50	25.52	25.38
CaO	0.05	0.01	0.08	0.09	0.08	0.06	0.07	0.07
Na_2O	0.30	0.38	0.40	0.37	0.39	0.22	0.23	0.20
K_2O	9.39	9.11	9.12	9.32	9.22	9.54	9.46	9.50
F	-	-	-	-	-	-	-	-
Cl	-	-	-	-	-	-	-	-
H_2O	4.18	4.13	4.17	4.17	4.17	4.17	4.18	4.17
Total	94.74	94.06	94.50	94.81	94.53	94.66	94.67	94.54
Total+H_2O	98.91	98.19	98.67	98.98	98.70	98.83	98.85	98.71
#Mg	91.23	90.83	91.16	91.43	91.28	92.08	92.10	92.08
Cl	353	334	356	329	358	192	182	190
Rb	656	642	634	620	655	649	612	611
Sr	10.77	10.62	10.64	8.63	10.37	2.794	3.94	2.882
Zr	2.356	2.31	2.336	2.937	2.388	3.463	3.24	3.178
Nb	6.74	6.97	6.46	6.8	5.56	10.56	11.29	11.02
Cs	3.58	3.52	3.4	3.233	3.368	3.364	3.105	3.389
Ba	622	624	583	503.5	581	219.9	224.6	222.3
La	0.007	0.003	0.004	0.003	0.06	0.004	0.002	0.001
Hf	0.08	0.063	0.072	0.099	0.078	0.2	0.12	0.105
Ta	0.332	0.358	0.313	0.334	0.257	0.962	0.952	0.978
Pb	0.12	0.113	0.131	0.108	0.167	0.0288	0.04	< LOD
Th	0.618	0.725	0.288	0.886	0.585	0.071	0.119	0.088

Table 11c: Major and trace element analyses for phlogopite in xenolith samples from Nigerdlikasik (Nigerd) and Pyramidefjeld (Pyramid). Trace elements were collected by laser-ablation inductively-coupled plasma-spectrometry (LA-ICP-MS). < LOD are analyses below the limit of detection.

Location	Nigerd'	Nigerd'	Nigerd'	Nigerd'	Nigerd'	Nigerd'	Nigerd'
Sample	NX-02	NX-02	NX-01	NX-01	NX-01	NX-01	NX-01
Mineral	Phl-9	Phl-10	Phl-21	Phl-22	Phl-23	Phl-24	Phl-25
SiO_2	41.51	41.39	41.07	40.96	41.11	41.15	41.09
TiO_2	1.00	1.04	1.40	1.37	1.36	1.36	1.34
Al_2O_3	12.14	12.21	13.65	13.72	13.80	13.46	13.81
Cr_2O_3	0.54	0.53	1.15	1.11	1.11	1.12	1.10
FeO_t	3.84	3.85	3.75	3.80	3.79	3.77	3.82
MnO	0.01	0.03	0.00	0.00	0.00	0.00	0.00
NiO	0.24	0.16	0.08	0.08	0.20	0.22	0.11
MgO	25.45	25.38	25.02	25.03	24.87	25.23	24.99
CaO	0.05	0.05	0.13	0.08	0.05	0.13	0.12
Na2O	0.22	0.20	0.33	0.38	0.40	0.34	0.34
K_2O	9.65	9.49	9.05	9.25	9.18	8.95	9.11
F	-	-	-	-	-	-	-
Cl	-	-	-	-	-	-	-
H_2O	4.16	4.16	4.22	4.22	4.23	4.23	4.23
Total	94.64	94.34	95.63	95.78	95.86	95.72	95.84
Total+H_2O	98.81	98.50	99.85	100.00	100.09	99.95	100.07
#Mg	92.19	92.16	92.25	92.16	92.12	92.26	92.10
Cl	190.3	180.8	538	549	533	512	524
Rb	597	604	401	426	479	470	454
Sr	3.158	2.819	79.9	81.9	82.47	78.4	79.33
Zr	3.139	3.04	1.45	1.584	1.456	1.597	1.547
Nb	11.54	10.94	0.839	0.921	0.794	0.993	0.823
Cs	3.224	3.104	2.7	2.549	2.927	2.713	2.758
Ba	219.3	222.4	2044	1889	1764	1600	1694
La	0.001	0.002	0.009	0.017	0.007	0.013	0.007
Hf	0.097	0.109	0.044	0.041	0.044	0.045	0.047
Ta	0.968	0.96	0.045	0.057	0.039	0.051	0.039
Pb	0.037	0.026	0.582	0.606	0.609	0.579	0.619
Th	0.183	0.094	0.136	0.145	0.138	0.127	0.123

Table 11c: *continued*

Location	Pyramid'	Pyramid'	Pyramid'	Pyramid'
Sample	PX-01	PX-01	PX-01	PX-01
Mineral	Phl-26	Phl-28	Phl-29	Phl-30
SiO_2	42.27	43.07	42.75	42.89
TiO_2	0.26	0.20	0.18	0.21
Al_2O_3	11.19	11.22	11.24	11.34
Cr_2O_3	0.13	0.12	0.22	0.20
FeO*	4.42	4.28	4.26	4.35
MnO	0.00	0.00	0.00	0.00
NiO	0.17	0.09	0.09	0.11
MgO	26.70	26.94	26.95	27.13
CaO	0.09	0.04	0.04	0.00
Na_2O	0.18	0.18	0.22	0.18
K_2O	9.27	9.62	9.75	9.66
F	-	-	-	-
Cl	-	-	-	-
H_2O	4.17	4.22	4.21	4.23
Total	94.68	95.76	95.68	96.07
Total+H_2O	98.86	99.98	99.89	100.30
#Mg	91.51	91.81	91.86	91.75
Cl	63	67.8	72.8	60.2
Rb	372	398	429	378
Sr	1.35	1.295	1.371	1.259
Zr	1.156	1.001	1.431	1.147
Nb	5.53	5.134	5.22	5.15
Cs	2.469	2.642	2.274	2.32
Ba	1070	470	215.2	431
La	0.0071	0.0050	0.0089	0.0043
Hf	0.0359	0.0249	0.0364	0.0272
Ta	0.398	0.4131	0.379	0.402
Pb	0.205	0.15	0.048	0.164
Th	14.56	11.29	2.763	12.56

Table 11c: *continued*

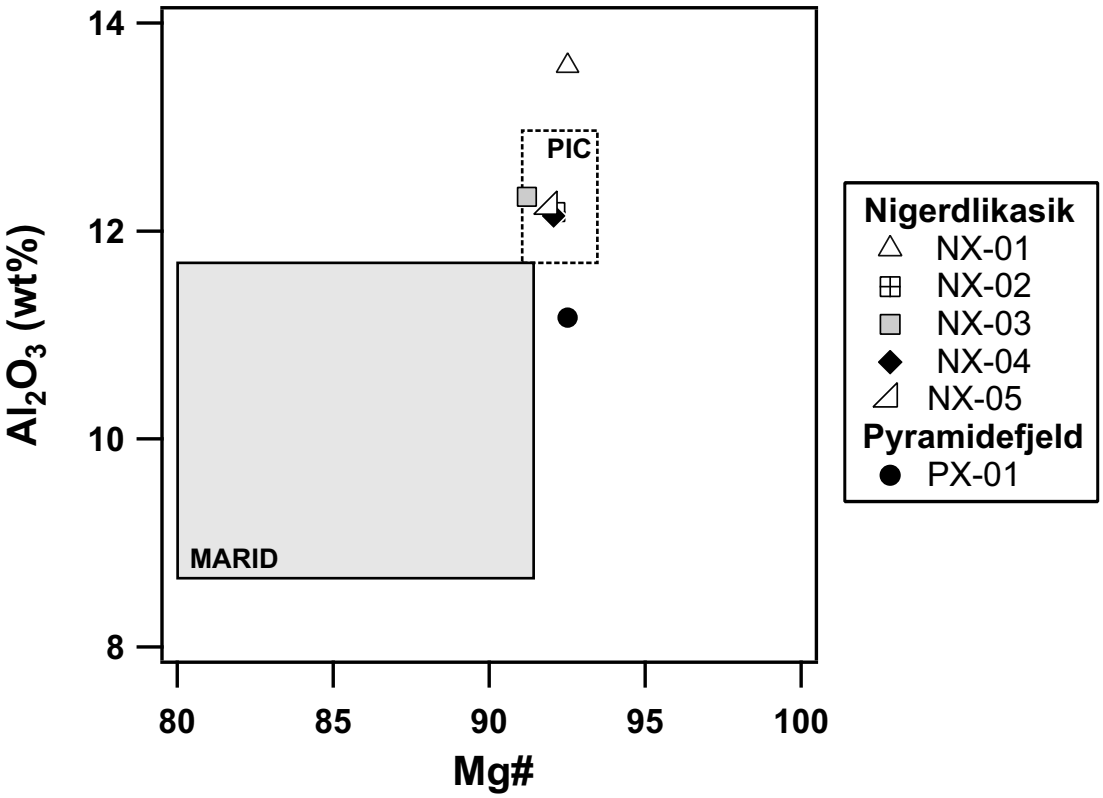

Figure 20: Al_2O_3 vs Mg# (Mg / Mg + Fe) for phlogopite from C-SCLM xenoliths recovered in ultramafic lamprophyre (UML) from Nigerdlikasik and Pyramidefjeld. Field for mica (phlogopite)-amphibole (K-richterite)-rutile-ilmenite-diopside (MARID) of Dawson and Smith (1977), based upon data from Dawson and Smith, (1977) and Waters, (1987a). Field for PIC based upon data from Jones et al., 1982 and Waters (1987b) reclassified by Grégoire et al., (2002) as belonging to the phlogopite-ilmenite-clinopyroxene (PIC) assemblage.

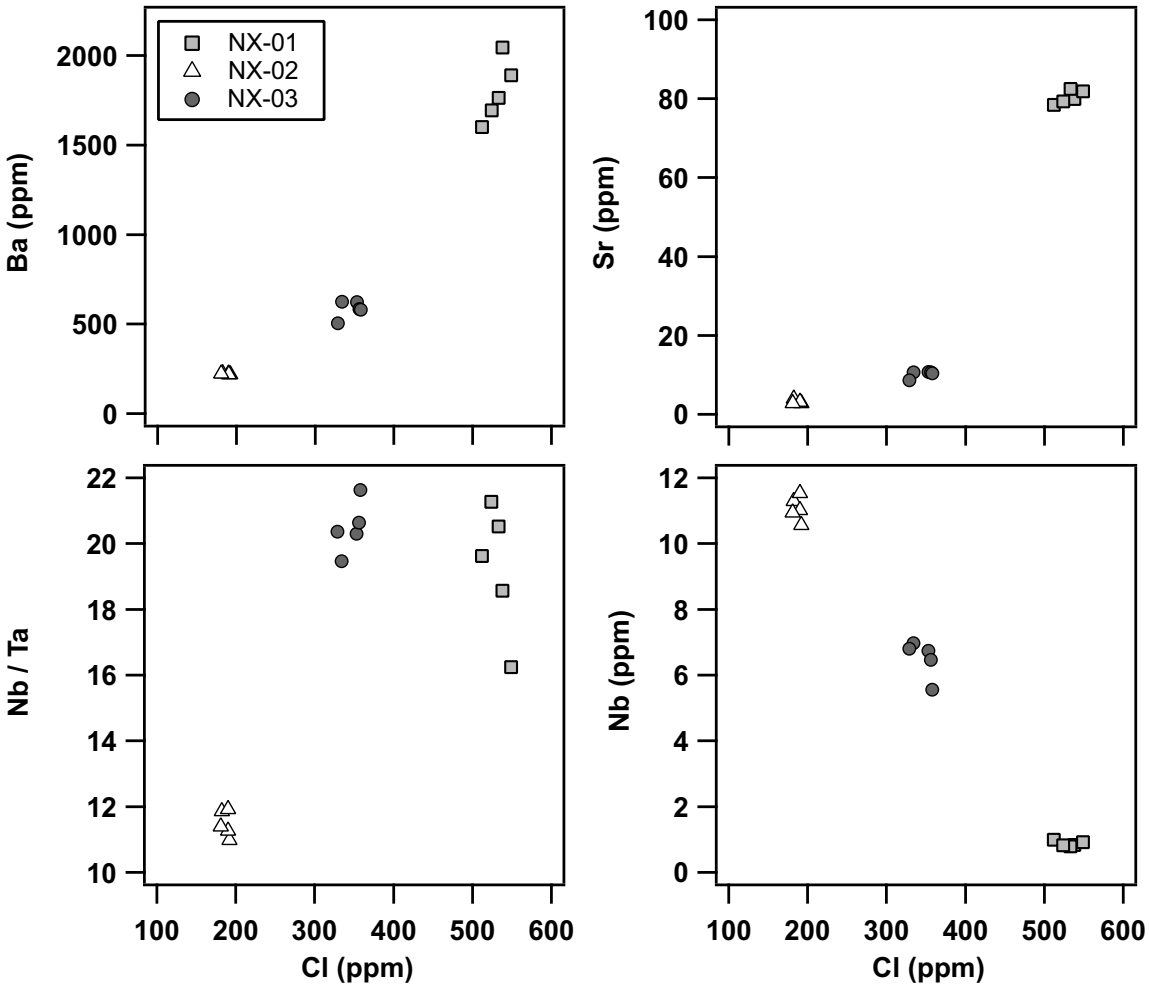

Figure 21: Ba, Sr, Nb/Ta and Nb vs Cl for phlogopite from xenoliths recovered from ultramafic lamprophyre (UML) from Nigerdlikasik, South Greenland.

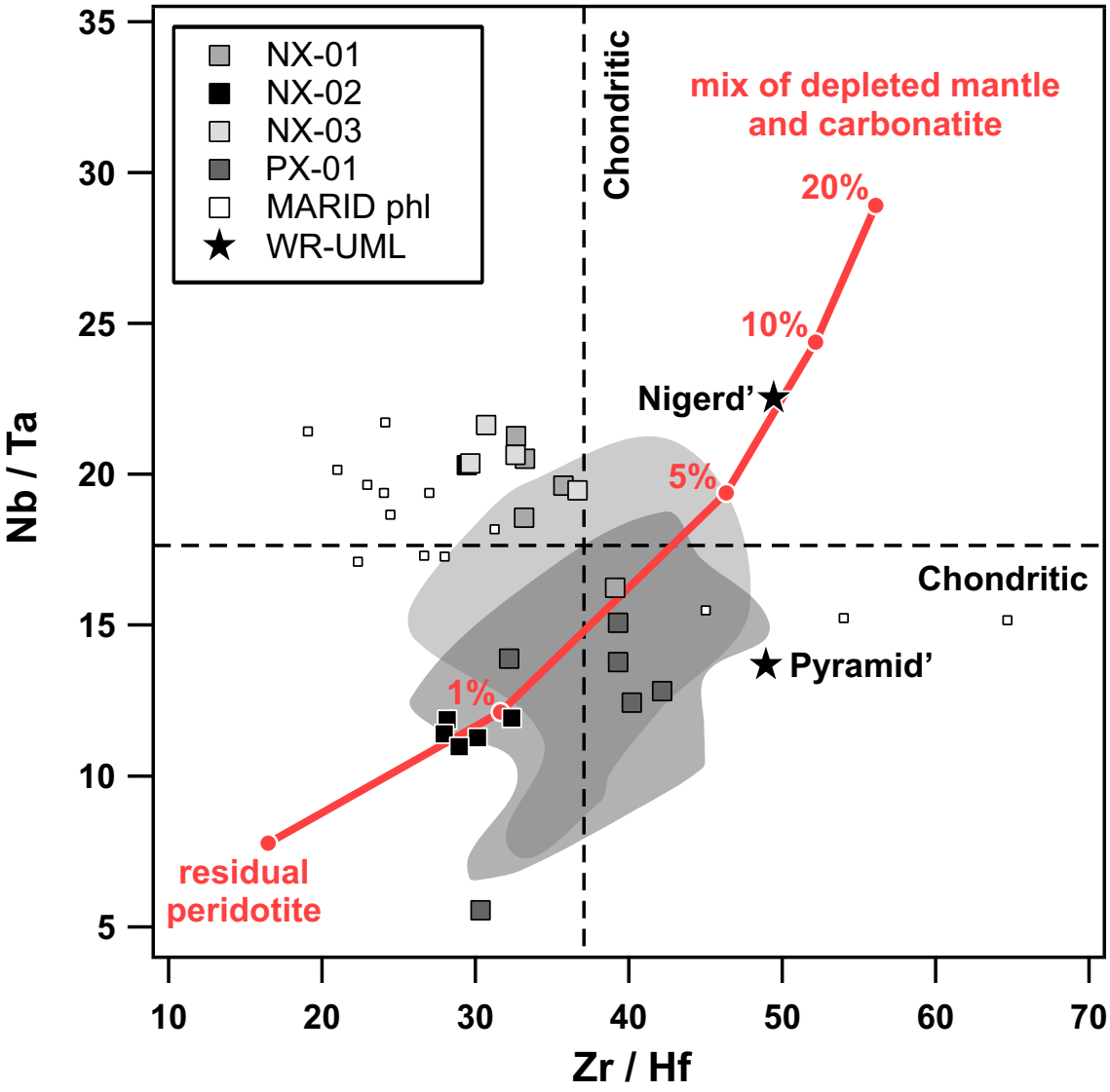

Figure 22: Nb/Ta vs Zr/Hf for phlogopite from mantle xenoliths recovered in ultramafic lamprophyre (UML) from Nigerdlikasik (NX-01; NX-02; NX-03) and Pyramidefjeld (PX-01) as well as whole-rock Nb/Ta vs Zr/Hf for UML. Chondritic Nb/Ta and Zr/Hf from McDonough and Sun, (1995). MARID for data phlogopite from Giuliani et al., (2015). Calculated trend of a mix of depleted residual peridotite (BP6-PE) of Weyer et al., (2003) and carbonatite (Chakhmouradian, 2006) modelled by Aulbach et al., (2013). Dark grey field displaying whole-rock kimberlite Nb/Ta vs Zr/Hf from Maniitsoq (Nielsen and Jensen, 2005; Nielson et al., 2009; Tappe et al., 2011) and light grey field displays UML compilation from the NAC (Tappe et al., 2004; Tappe et al., 2006; Gaffney et al., 2007; Nielsen et al., 2009; Tappe et al., 2011).

high and slightly more variable, reflected in Mg# that ranges from ~90 – 92. One xenolith sample from UML (NX-01) at Nigerdlikasik has higher Al_2O_3 (~13 wt. %). Phlogopite from the one xenolith analysed from Pyramidefjeld (PX-01) displays lower Al_2O_3 contents (~11 wt. %).

The two xenolith samples from Nigerdlikasik that were analysed for trace elements in clinopyroxene (NX-02; NX-03) as well as two additional samples; NX-01 (from Nigerdlikasik) and PX-01 (from Pyramidefjeld), were analysed for a small suite of trace elements in addition to Cl. Analysed elements show a large range in concentrations between each xenolith (e.g. Ba = 200 – 2000 p.p.m.; Rb 300 – 600 p.p.m.; Sr = 2 – 80 p.p.m.; Nb = 0.8 – 11 p.p.m.; Pb 0.02 – 0.5 p.p.m.; Th = 0.1 – 15 p.p.m.). Cl contents range from below limit of detection (< 100 p.p.m.) to ~530 p.p.m. Cl contents are positively correlated with Ba and Sr, compatible elements in phlogopite, and negatively with Nb, a strongly incompatible element in phlogopite (Figure. 21) suggesting a surprisingly high compatibility for Cl in phlogopite. Phlogopite with the highest Cl contents also contain the highest Nb/Ta. There is also dichotomy in Nb/Ta and Zr/Hf; samples NX-01 and -02 display suprachondritic Nb/Ta, while conversely NX-03 and PX-01 display subchondritic Nb/Ta (Figure. 22).

5.3.5. Ilmenite

Ilmenite mineral analyses are reported in Table. 12 from xenolith NX-03. Ilmenite within NX-03 are largely homogenous: TiO_2 ~54 wt. %; MgO ~ 25 wt. %, with unusually high NiO contents ranging from 14 – 18 wt. %. FeO is extremely low > 0.5 wt. % as is Al_2O_3 and SiO_2.

5.3.6. Spinel

Spinel mineral analyses are reported in Table. 13 from xenoliths PX-01, NX-01, NX-03 and NX-07. Spinel are chromite; Cr_2O_3 ~ 52 – 55 wt. %; FeO ~ 22 – 30 wt. %; Al_2O_3 ~ 1 – 10 wt. % and MgO ~ 10 – 12 wt. %. NX-07 by contrast has a high Al_2O_3 content ~41 wt. %, lower Cr_2O_3 ~ 28 wt. % and higher MgO of ~16 wt. %.

Location	Nigerd	Nigerd	Nigerd	Nigerd	Nigerd	Nigerd	Nigerd	Nigerd
Sample	NX-03	NX-03	NX-03	NX-03	NX-03	NX-03	NX-03	NX-03
Mineral	Ilm-1a	Ilm-1b	Ilm-1c	Ilm-2a	Ilm-2b	Ilm-3a	Ilm-3b	Ilm-3c
SiO_2	0.17	0.17	0.13	0.24	0.17	0.13	0.15	0.21
TiO_2	53.31	53.86	53.65	53.50	53.58	54.63	54.66	54.91
Al_2O_3	0.26	0.19	0.23	0.26	0.26	0.43	0.42	0.40
Cr_2O_3	3.67	3.45	3.60	4.56	4.57	3.57	3.61	3.60
MgO	25.00	24.38	24.93	25.18	25.06	21.87	22.01	21.96
FeO_t	0.22	0.17	0.25	0.35	0.27	0.19	0.17	0.28
MnO	0.24	0.22	0.18	0.29	0.25	0.11	0.20	0.11
NiO	15.62	15.92	15.54	14.16	14.16	17.23	17.41	17.34
CaO	0.01	0.03		0.08	0.10	0.06	0.06	
Na_2O	0.11	0.11	0.11	0.08	0.04	0.09	0.09	0.00
K_2O	0.00	0.01	0.01	0.00		0.02	0.01	0.02
Total	98.62	98.50	98.61	98.70	98.48	98.34	98.80	98.85

Table 12: Ilmenite compositions from xenolith NX-03 recovered from ultramafic lamprophyre at Nigerdlikasik (Nigerd)

Location	Nigerd	Nigerd	Nigerd	Nigerd	Nigerd	Nigerd	Pyramid	Pyramid
Sample	NX-01	NX-01	NX-07	NX-07	NX-03	NX-03	PX-01	PX-01
Mineral	spn-2	spn-3	spn-4	spn-5	spn-9	spn-10	spn-2	spn-3
SiO_2	0.11	0.12	0.14	0.11	0.09	0.11	0.04	0.04
TiO_2	3.04	3.04	0.13	0.09	3.81	3.82	1.88	2.01
Al_2O_3	8.49	8.44	41.50	41.68	2.58	2.58	3.34	5.33
Cr_2O_3	52.67	52.10	28.17	28.15	51.93	51.98	55.52	53.11
FeO_t	22.62	23.09	14.02	13.86	31.73	31.82	26.15	26.82
MnO	0.28	0.30	0.15	0.16	0.26	0.28	0.11	0.50
NiO	0.05	0.18	0.17	0.11	0.15	0.17	0.00	0.00
MgO	12.49	12.12	16.00	16.26	8.18	8.30	11.10	10.83
CaO	0.00	0.02	0.02	0.01	0.02	0.02	0.00	0.00
Total	99.76	99.42	100.31	100.44	98.75	99.08	98.15	98.64
Si	0.03	0.03	0.03	0.03	0.03	0.03	0.01	0.01
Ti	0.60	0.60	0.02	0.02	0.80	0.80	0.39	0.41
Al	2.62	2.61	10.94	10.96	0.85	0.84	1.08	1.70
Cr	10.88	10.83	4.98	4.96	11.44	11.41	12.00	11.35
Fe^{3+}	1.15	1.15	0.00	0.00	1.93	1.95	2.08	1.92
Fe^{2+}	3.80	3.92	2.62	2.58	5.46	5.43	3.89	4.15
Mn	0.05	0.05	0.02	0.02	0.05	0.05	0.02	0.09
Ni	0.01	0.04	0.03	0.02	0.03	0.04	0.00	0.00
Mg	4.87	4.75	5.34	5.41	3.40	3.43	4.53	4.37
Mg#	49.61	48.34	67.04	67.66	31.49	31.73	43.09	41.85
Ca	0.00	0.01	0.01	0.00	0.01	0.01	0.00	0.00
Cations	24	24	24	24	24.00	24.00	24.00	24.00

Table 13: Representative major element analyses of spinel from xenoliths recovered from at Nigerdlikasik (Nigerd) and Pyramidefjeld (Pyramid) by energy-dispersive X-ray spectroscopy via scanning electron microscope (SEM-EDX). Mg # - (Mg / Mg + Fe) x 100. Total iron is reported as Fe^{2+}. Fe^{3+} calculated from stoichiometry assuming full occupancy of the B^{3+} site. Cations normalized to 32 oxygen.

Chapter 6.0: Discussion

6.1.1. Assessing potential crustal contamination

Evidence of interaction with, and assimilation of, crustal contamination from basement lithologies in UML from Pyramidefjeld can be ruled out on the basis of the extreme undersaturation in Al and Si (Figure. 11) in addition to a Ce/Pb of 45. These characteristics are comparative to UML and kimberlite elsewhere on the NAC and similar to values reported for uncontaminated OIB ~ 47 (Hofmann, 1988). UML from Nigerdlikasik, although more depleted with respect to Si and Al than UML from Pyramidefjeld, displays a prominent positive Pb anomaly on a primitive-mantle normalized trace element variation diagram (Figure. 12). Since Pb is nominally depleted in the mantle and heavily concentrated in the Earth's crust, positive Pb anomalies (e.g. le Roex et al., 2003) and low Ce/Pb ratios are often used as a geochemical screen for crustal contamination in UML and kimberlite (e.g. Tappe et al., 2011). This prominent Pb enrichment is not observed in UML or kimberlite elsewhere on the NAC and might suggest incorporation and contamination of UML from Nigerdlikasik with basement material during emplacement. Primitive mantle-normalized ACC (average continental crust; Rudnick and Gao, 2003) displays a similar Pb anomaly to UML from Nigerdlikasik, albeit at a slightly lower concentration (Figure. 23). The slightly lower concentration of Pb in ACC comparative to Pb in Nigerdlikasik does not preclude crustal contamination since Pb concentrations from NAC basement rocks of the Tasiusarsuaq Terrane at Tikiusaaq - (Figure. 6), although highly variable dependant on lithology, extend to over 30 p.p.m. (Tappe et al., 2017) and higher than ACC (Rudnick and Gao, 2003). Nonetheless, several lines of evidence suggest that crustal contamination is insignificant. UML from Nigerdlikasik and Pyramidefjeld have low Clement contamination indices (C.I; Clement, 1982) of 1.1 and 1.0 respectively that are also indistinguishable to C.I for both UML using XRF data of Emeleus and Andrews, (1975). Despite being developed for kimberlite they offer a useful comparison, although the mutually opposing effects of the assimilation of C-SCLM and cratonic continental crust limit the effectiveness of this screen (e.g. le Roex et al., 2003). Traditionally, values < 1 are considered uncontaminated, although several authors suggest values as high as 1.5 are also representative of uncontaminated magmas (e.g. Clement, 1982; Taylor et al., 1994). It is notable that Nigerdlikasik has a lower C.I than Pyramidefjeld which might be unexpected given its higher Pb content. Le Roex et al., (2003) noted

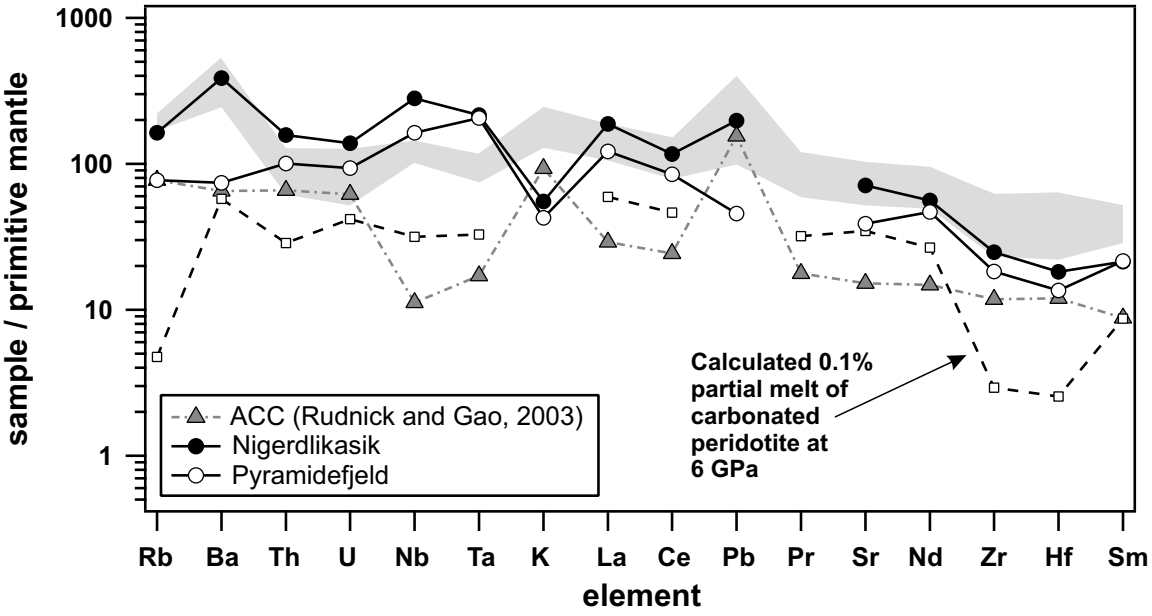

Figure 23: Incompatible trace element diagram for ultramafic lamprophyre (UML) from Nigerdlikasik and Pyramidefjeld normalized against primitive mantle of Sun and McDonough (1989). For comparison average continental crust (ACC) of Rudnick and Gao, (2003) and shaded field showing range of compositions of lamproite from Aillik Bay, Canada (Tappe et al., 2007). Calculated 0.1% melt at 6 GPa is shown following the method of Tappe et al., (2011), they were obtained by utilizing the experimentally determined bulk peridotite/kimberlitic melt partition coefficients of Brey et al. (2008) using a batch partial melting equation of Dasgupta et al., (2006). Primitive mantle values of Sun and McDonough, (1989).

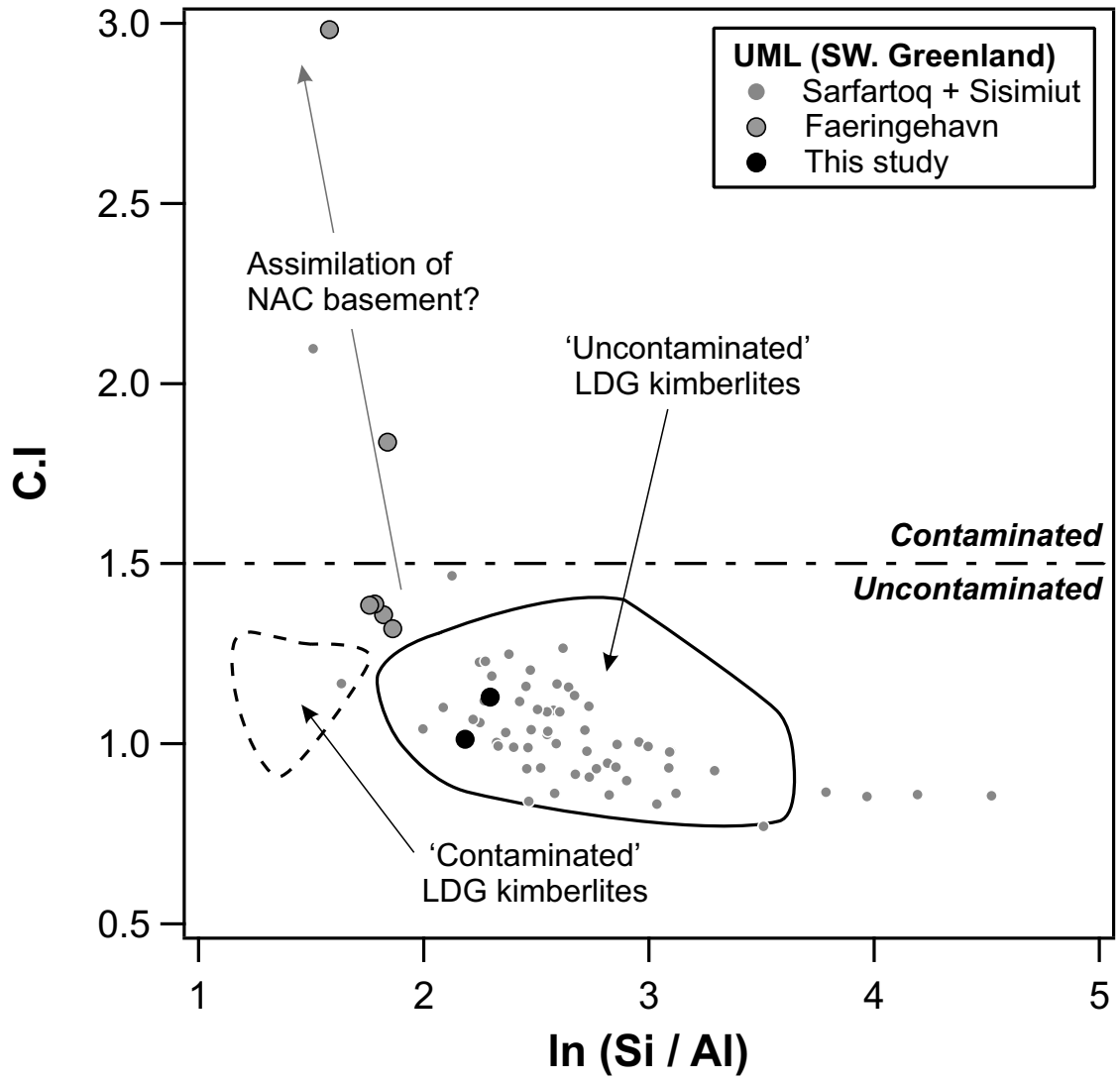

Figure 24: Contamination index (C.I) of Clement, (1982) vs ln(Si / Al) for ultramafic lamprophyre (UML) from Nigerdlikasik and Pyramidefjeld. Contaminated and uncontaminated fields for Lac de Gras kimberlites, Canada, from Kjarsgaard et al., (2009). Data for uncontaminated Sarfartoq and Sisimiut UML from (Gaffney et al., 2007; Nielsen et al., 2009; Tappe et al., 2011) and Faeringehavn from (Tappe et al., 2017).

that comparatively ln (Si/Al) is a far more sensitive screen to the addition of Al_2O_3-rich crustal lithologies than C.I (Figure. 24). In this respect both UML plot well within fields delimitating uncontaminated kimberlite from Lac de Gras (Le Roex, 2003), Canada. UML at Faeringehavn, on the northern boundary of the NAC have initial radiogenic isotope compositions that approach NAC basement which might be inferred to demonstrate assimilation of crustal material (Tappe et al., 2017). It is notable that Faeringehavn UML have both higher C.I ~1.4 (up to ~3) and lower ln (Si / Al). A further comparison with UML from Sarfartoq, that on the basis of Sr-Nd-Pb systematics and high Ce/Pb which preclude significant crustal contamination, plot largely within the uncontaminated field (Figure. 24). Moreover, if extensive crustal contamination for UML at Nigerdlikasik is assumed, the contents of several elements particularly the HFSE but especially Nb, would be expected to be significantly higher prior to contamination, due to the similarly low Nb contents calculated from a 0.1% carbonated peridotitic melt at ~ 6 GPa (c.f. Tappe et al., 2011). It is apparent that crustal contamination alone can explain the differences in primitive mantle-normalized trace element patterns observed between UML at Nigerdlikasik and Pyramidefjeld. Therefore crustal contamination of UML at Nigerdlikasik and Pyramidefjeld or Nigerdlikasik relative to Pyramidefjeld is not considered to be significant.

6.1.2. Late-stage fluid mobility

An alternative solution for Pb-enrichment observed in UML from Nigerdlikasik is through late-stage fluid mobilization, immiscibility and deuteric alteration of ultramafic magmas as a result of the formation of a late crystallizing 'amoeboid' assemblage of serpentine ± carbonate (le Roex et al., 2003). In extreme cases it has been argued that this segregation may lead to 'carbonatitic' bodies, such as those observed within kimberlite at Benfontein, South Africa, which are remarkably similar geochemically and isotopically to carbonatite (e.g. Dawson and Hawthorne, 1973). Such late-stage fluid movement and segregation is expected to offer potential perturbation of the initial concentrations of all fluid mobile elements (FME) not only Pb. UML from Nigerdlikasik and Pyramidefjeld display petrographic evidence of formation of amoeboid-like serpentine + carbonate assemblages (Figure. 7a). Since UML from Nigerdlikasik display enrichment in several other FME it might be argued that the relatively high Pb, Ba, Sr contents relative to Pyramidefjeld might be best explained by

late-stage fluid mobility, particularly as there is no obvious perturbation to the SiO_2 content of UML from Nigerdlikasik.

However, modification of UML composition via late-stage fluid mobilization can be argued to be minor in UML from Nigerdlikasik. Firstly, it should be noted that the general primitive mantle-normalized trace element pattern of Nigerdlikasik relative to Pyramidefjeld (which has no prominent negative Pb-anomaly) is generally more enriched; including elements not as heavily concentrated in the Earth's crust as Pb and including those that are not fluid-mobile (e.g. Nb, Ta, Zr, Hf, Th). Thus, late-stage concentration of FME in volatile-rich amoeboid segregations would be expected to *lower* overall HFSE concentrations and accentuate the Zr-Hf trough observed on the primitive mantle-normalized trace-element variation diagram. Therefore such accumulation would lead to far more highly fractionated HFSE/FME trace element patterns (c.f. carbonatite), yet, UML from Nigerdlikasik displays no such systematics (Figure. 12) and is simply systematically more enriched. On this basis, late-stage fluid remobilization appears to be insignificant in UML from either Pyramidefjeld or Nigerdlikasik

6.1.3. Crustal incorporation of halogens

The high fluid mobility of the halogen elements and overwhelming concentration in the Earth's surficial reservoirs imply that incorporation of crustal lithologies during UML or metamorphic alteration close to or at the Earth's surface could have a significant impact on the halogen inventories of UML magmatism. UML from Pyramidefjeld and Nigerdlikasik are emplaced on craton (e.g. within TTG) or in the case of UML from Pyramidefjeld within a ~1.8 Ga granitoid complex. Apatite is likely the only phase capable of hosting halogens to a significant concentration within TTG or the Pyramidefjeld granites both UML are emplaced within. However, whole-rock UML Cl contents are only slightly exceeded by Cl concentrations reported for apatite from granitoids (e.g. Belousova et al., 2001; Chu et al., 2009). The bulk contents of Cl from rocks themselves are therefore expected to be significantly lower and would be unlikely to exert an appreciable effect to significantly alter halogen contents of either UML or $\delta^{37}Cl$ compositions.

Infiltration of halogen-enriched meteoric waters are also extremely unlikely to have affected either UML due to experimental and theoretical constraints that ^{35}Cl preferably partitions into aqueous phases (Schauble et al., 2003; Barnes and Sharp, 2017 and

references therein). Due to the + 1.0 – 1.2 δ^{37}Cl composition observed in both UML if interaction with meteoric fluids occurred these values would likely be depressed, and overprinted by, the elemental and isotopic composition within fluids. Petrographic evidence of interaction with meteoric fluids or alteration at or near the Earth's surface is also not evident. It is stressed that the UML from Pyramidefjeld and Nigerdlikasik are exceptionally fresh and display no textural evidence of post-emplacement alteration. Serpentine does occur interstitially within the groundmass as a magmatic phase inferred to crystallize at T > 600 °C (e.g. Kopylova et al., 2007) and as alteration rims around large entrained olivine formed at temperatures of ~200-300°C (e.g. Mitchell, 2013). These crystallization temperatures suggests that significant δ^{37}Cl fractionation would not be expected (e.g. Schauble et al., 2003). This data when coupled with δ^{37}Cl compositions of phlogopite within mantle xenolith NX-01, which is statistically indistinguishable from its host UML, suggests that halogen systematics observed in both UML are intrinsic to the original UML and cannot result of either contamination or post-emplacement alteration.

6.2. Magma composition and classification

6.2.1 Magma composition and classification

UML from Pyramidefjeld and Nigerdlikasik have previously been identified as kimberlite (e.g. Emeleus and Andrews, 1975). When classified using the updated IUGS classification scheme for igneous rocks of Le Maitre et al., (2002) updated by Tappe et al., (2005) these rocks are classified as ultramafic lamprophyre UML, more specifically the carbonate-rich variety aillikite. Although petrographically very similar to kimberlite, groundmass phase assemblage and composition is atypical for kimberlite on the basis of groundmass spinel that are characterized by a low ulvöspinel component, Al enrichment [Cr/ (Cr + Al) < 0.85] and the occurrence of Al_2O_3 and TiO_2 enriched and Cr_2O_3 depleted groundmass clinopyroxene. The high Ni, Cr and Mg# contents of UML from Nigerdlikasik and Pyramidefjeld meet the criteria of near-primary mantle derived magmas (e.g. Frey et al., 1978) and resemble experimentally produced high-pressure melts of synthetic carbonated garnet peridotite in the simple CMAS (CaO-MgO-Al_2O_3-SiO_2)-CO_2 system between 5 and 8 GPa suggesting a convective upper mantle source (Figure. 25; Gudfinnsson and Presnall, 2005). Significant accumulation of xenocrystic olivine will artificially increase and displace MgO/CaO and SiO_2 /Al_2O_3 toward the CO_2-free solidus and will lead to an overestimated depth of melting. Brett et al., (2009)

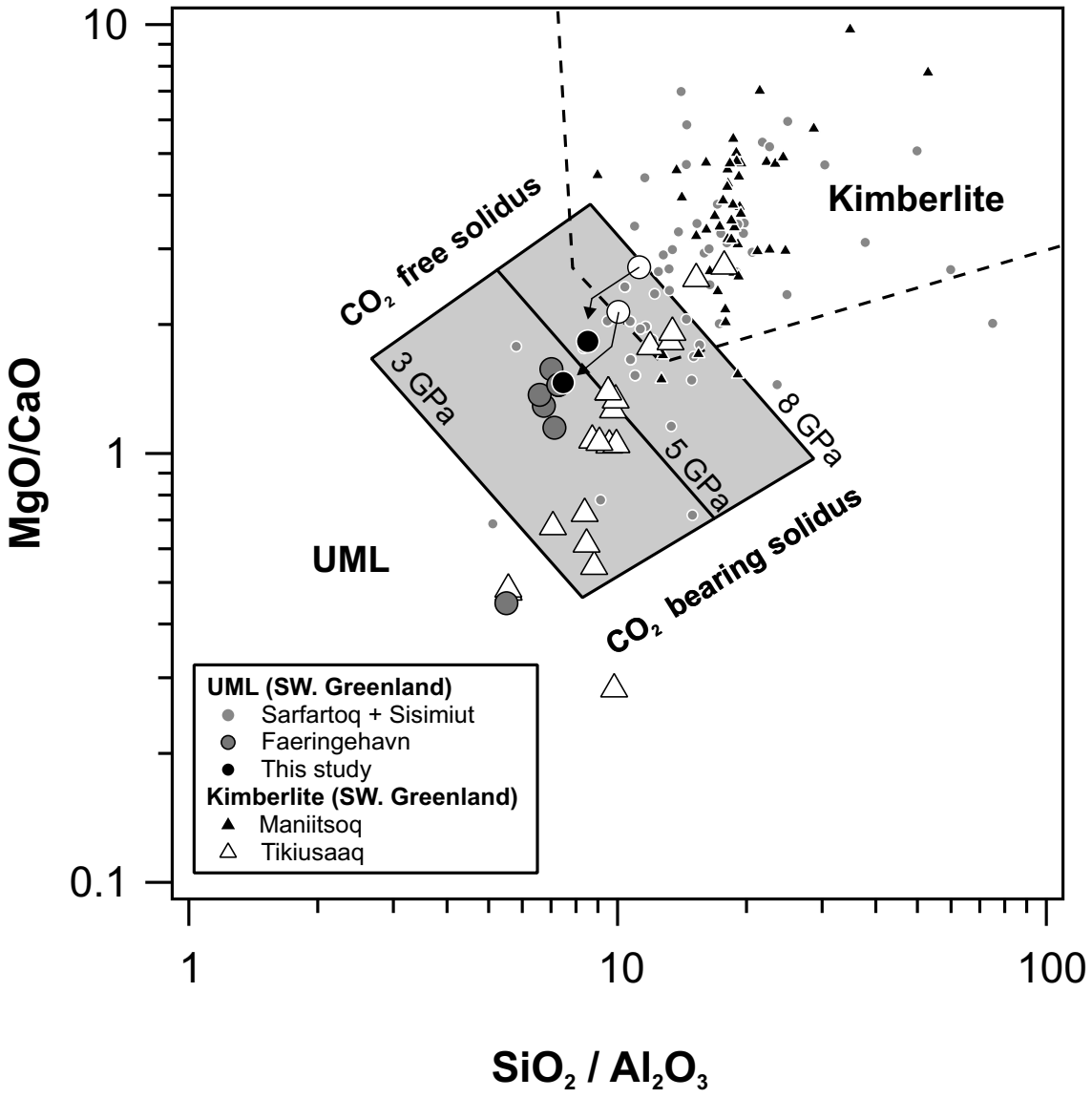

Figure 25: MgO / CaO vs SiO_2 / Al_2O_3 for ultramafic lamprophyre (UML) from Nigerdlikasik and Pyramidefjeld. Compared with UML data from Sarfartoq (Gaffney et al., 2007;Nielsen et al., 2009; Tappe et al., 2011), Sisimiut (Nielsen et al., 2009), Faeringehavn (Tappe et al., 2017) and kimberlite from Maniitsoq (Gaffney et al., 2007; Nielsen et al., 2009; Tappe et al., 2011) and Tikiusaaq (Tappe et al., 2017). Fields for experimentally produced melt compositions from synthetic and natural carbonated peridotites under high pressures are after Gudfinnsson and Presnall (2005). UML-kimberlite discrimination from Rock, (1991). Arrows indicate recalculated compositions after subtraction of xenocrystic olivine.

estimate that olivine within kimberlite (and likely by extension UML due to their similar petrogenesis) is no more than 5% magmatic in origin and that the whole rock inventory is dominated by xenocrystic olivine. Olivine macrocrysts comprise ~25% of the whole rock inventory of rocks from Pyramidefjeld and Nigerdlikasik and so in accounting for 20% incorporation of xenocrystic olivine (Mg# 92.5) both UML are shifted to lower depths toward 5 GPa and into the UML field delimitated by Rock, (1991).

The high K contents of both UML require an essential contribution of a K-bearing phase within its source region. Phlogopite; which is observed in most entrained xenoliths, and K-richterite are major K hosts within metasomatised assemblages in C-SCLM stable up to 7 GPa and 8.5 GPa respectively (e.g. Sudo and Tatsumi, 1990; Konzett et al., 1997). The absence of K-richterite in any entrained mantle xenoliths from either Nigerdlikasik or Pyramidefjeld and the extremely high K/Na ratios and silica under-saturation of both UML suggest phlogopite is the dominant K-bearing phase within the melting assemblage. Elevated HFSE abundances in UML from Nigerdlikasik could suggest the presence of a HFSE-bearing phase such as ilmenite (which is observed in several xenoliths) within its source region.

6.2.1. Exsolution of halogens during UML emplacement

The primary composition of UML and kimberlite and their evolution during ascent through the continental lithosphere during emplacement is contentious. Several petrogenetic models for their formation suggest significant modification of an initial 'primary' upper mantle melt via exsolution of their volatile contents and evolution via magmatic differentiation (Woolley and Kjarsgaard, 2008; Tappe et al., 2017). Exolution of a fluid phase is supported by low Na_2O contents of UML and kimberlite, which is inconsistent with derivation from melting of a fertile peridotite (Stamm and Schmidt, 2017). Exsolution of a fluid phase from a silicate melt will fractionate halogens ratios in the order Br > Cl >> F (Bureau et al., 2000; Straub and Layne, 2003; Köhler et al., 2009). Exsolution of a fluid phase from a carbonated silicate melt at upper mantle or upper crustal levels would therefore be expected to dramatically lower heavy halogen contents in the residual melt, with F by contrast concentrated in the melt phase due to its non-hydrophilic character.

However, since Br/Cl ratios of UML at Nigerdlikasik and Pyramidefjeld are higher than the uniform Br/Cl of the convecting mantle, exsolution of a high Br/Cl and low

F/Cl fluid would necessitate both higher Br and Cl contents relative to F (i.e. lower F/Cl than recorded in both UML) and higher Br contents relative to Cl (i.e. higher Br/Cl than recorded in both UML) within the primary melt. On this basis, exsolution of a fluid phase alone cannot explain the contrasting halogen systematics comparative to convective mantle observed in both UML. However, it should be acknowledged that the halogen concentrations and ratios of both UML might not be indicative of a 'primary' melt composition.

6.3. Whole-rock geochemistry and origins of halogens in UML

The inferred similarly high incompatibility of Cl and Br in nominally anhydrous minerals common to the asthenospheric mantle suggests that little or no fractionation of these elements occurs even during low degrees of melting (e.g. Kendrick et al., 2017). Thus, the high Br/Cl ratios observed in both UML must reflect their mantle source(s). Due to the hybrid mixture of convective mantle and C-SCLM components in UML magmatism the halogen enrichment observed in both UML either result from the sampling of a high Br/Cl and positive δ^{37}Cl component;

i. Within a primordial un-degassed mantle reservoir;
ii. Within the convecting mantle or;
iii. Through interaction of the proto UML melt with a halogen-enriched C-SCLM during emplacement in the NAC

6.3.1. Option (i): Halogen systematics reflect sampling of a primordial mantle reservoir

Due to the High ^{3}He / ^{4}He ratios (up to 27_{Ra}) reported for olivine recovered from UML at Nigerdlikasik and Pyramidefjeld (Tachibana et al., 2006) it is possible that both sample a primordial 'un-degassed' volatile reservoir that is has been unrecorded in OIB to date, perhaps as a result of the relative paucity of halogen data for OIB comparative to noble gas data. Although, at this stage it should be stated some workers question the accuracy of the ^{3}He / ^{4}He data reported for olivine from UML at Nigerdlikasik and Pyramidefjeld (Fin Stuart, pers. Comm; Sebastian Tappe, pers. Comm).

The fractionated + δ^{37}Cl composition of both UML however is strongly suggestive of a dominantly recycled origin due to the lack of fractionation of Cl at high temperatures within the Earth and the inferred lack of Cl fractionation within the solar nebula during accretion of the Earth (e.g. Sharp et al., 2007; Sharp et al., 2013). Therefore, the halogen

composition of Jurassic UML magmatism in South Greenland is best explained by the sampling of recycled halogens from the Earth's halogen enriched surficial reservoirs.

6.3.2. Option (ii): Halogen systematics reflect sampling of the Earth's convecting mantle

The discovery of hydrous ringwoodite in diamond (Pearson et al., 2014) derived from the mantle transition zone as well as the capacity for NAM to contain water in OH^- defects in their structure and OIB (supposedly derived from the lower mantle) that have some of the highest H_2O contents of basalts (e.g. Saal et al., 2002) suggests the deep cycling of water, and halogens within the Earth (as supported by recycled $\delta^{37}Cl$ signatures of OIB). A deep halogen cycle including even the heavy halogens (Cl, Br and I) is further supported by the clustered and high relative abundances of Br in EM-I and EM-II type OIB in comparison to MORB and HIMU reservoirs that straddle the whole range of Br and Cl concentrations reported for mantle melts (Figure. 2). Such a deep cycle of halogens through retention in a subducted slab is theoretically possible if the subduction geotherm is sufficiently low so that subducting serpentine oversteps 'phase A' stability, a transformation in which almost no fluid production is expected (Schmidt and Poli, 2013). Experimental data suggests that similar high-density hydrous aluminosilicate minerals are potentially stable to depths as far as the lower mantle (e.g. Pamato et al., 2014) offering potential for a whole-scale mantle halogen cycle. It should however be stated that no such reservoir has ever been observed to have a demonstrably high Br/Cl relative to MORB or OIB. The heavy halogen composition of the mantle is stongly argued to reflect mantle-scale homogenization (Kendrick et al., 2017) and therefore appears an unlikely source for halogens in UML at Nigerdlikasik or Pyramidefjeld.

6.3.3. Option (iii): Halogen systematics reflect interaction and emplacement within overlying C-SCLM

Serpentine veins observed in xenolith PX-01 are remarkably Cl-rich (Figure. 26; up to 1.3 wt. %), while the $\delta^{37}Cl$ composition of phlogopite from xenolith NX-01, recovered from Nigerdlikasik is statistically indistinguishable to its host UML. The veins are cross-cut by the infiltration of UML along grain boundaries, as well as forming a strong sub-parallel vein network that does not exploit grain boundaries. This textural evidence implies that halogen enriched veins and minerals phases were present

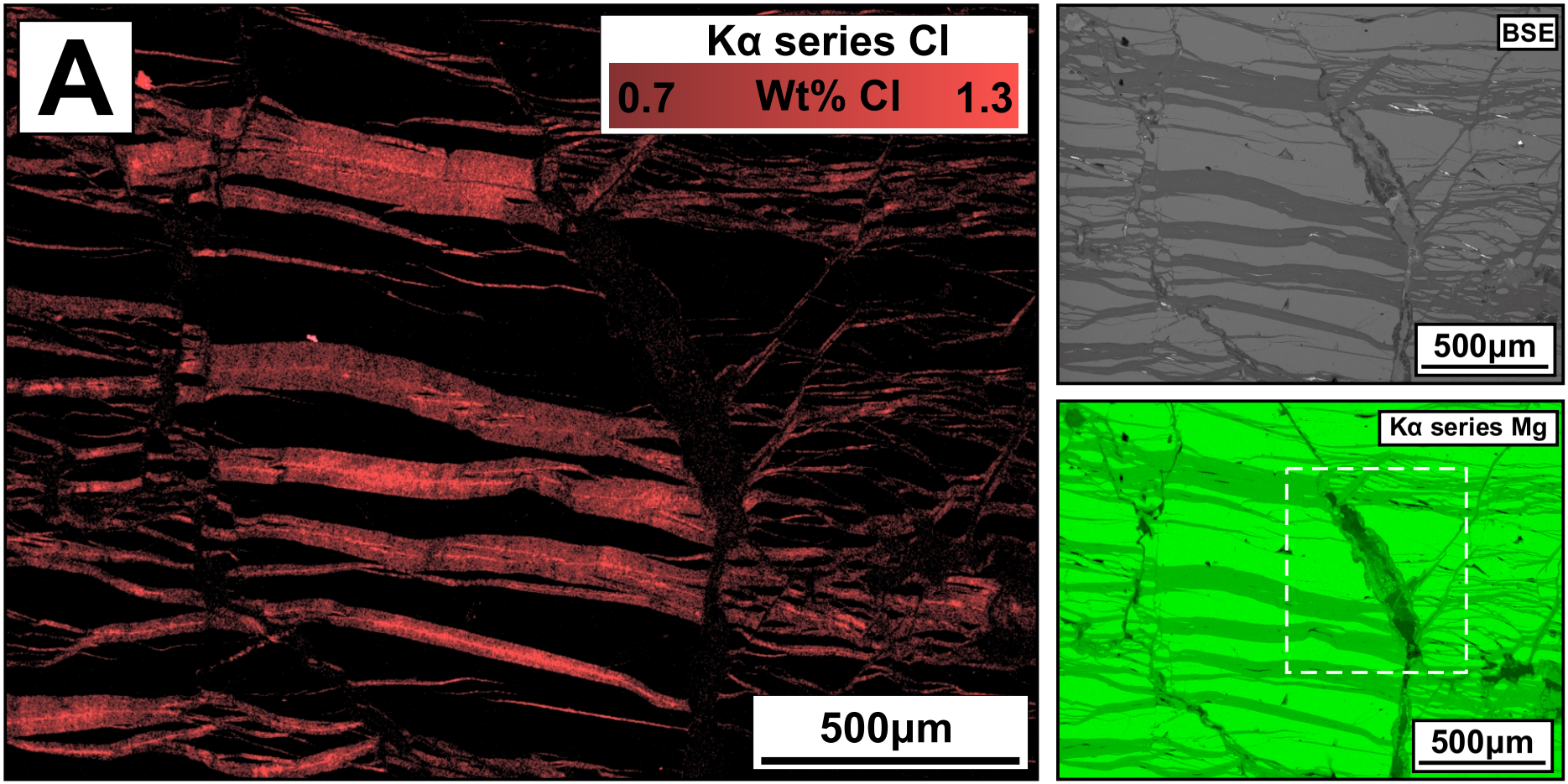

Figure 26: Kα series energy-dispersive X-ray scanning electron microscope (EDX-SEM) map of for chlorine (A) for serpentine veins in xenolith PX-01 recovered from ultramafic lamprophyre (UML) from Pyramidefjeld. Kα series foir Mg (bottom right) and back-scatter electron (BSE) image shown for comparison. White stippled field shows veins cross-cut by infiltration of UML.

within the C-SCLM preceding and prior to incorporation in UML magmatism. The southern boundary of the NAC has previously been subjected to the northward subduction of an oceanic plate during the 1.8 Ga Ketilidian Orogeny (Chadwick and Garde, 1996), which has been previously been implicated in generating metasomatism at the base of the C-SCLM on the basis of trace element systematics of Gardar period (~1.2Ga) magmatism in South Greenland and Os isotope systematics of C-SCLM sulfide phases (Goodenough et al., 2002; Wittig et al., 2010). Thus, delivery of halogens from the Earth's surficial, halogen-rich reservoirs during the northward subduction of an oceanic slab during the Ketilidian orogeny offers an obvious pathway for the recycling and delivery of halogens into the C-SCLM of the NAC, whereby it could be resampled by subsequent UML magmatism. It should be stated that the presence of halogen enriched fluids in the deep C-SCLM is already well documented within fluid inclusions in diamonds (Johnson et al., 2000; Burgess et al., 2002; Tomlinson et al., 2006; Burgess et al., 2009; Tomlinson et al., 2009) as is a subduction origin for diamonds themselves (e.g. Weiss et al., 2015).

6.3.4. The halogens subduction pathway

Within a subducting slab, the halogen elements are distributed between four principal reservoirs;

(i) marine pore-fluids,
(ii) Sediments,
(iii) Altered oceanic crust (AOC) and,
(iv) Serpentinite

The Br/Cl and $\delta^{37}Cl$ compositions of UML lie within a range of compositions reported for serpentinized oceanic peridotite and sediments delivered into the mantle during subduction (Figure. 13). The halogen compositions of both UML are also highly comparable to arc pyroclastics and lavas from the Central American Arc (Figure. 13). The respective halogen compositions of marine pore-fluids and AOC delivered into the mantle during subduction are unlikely sources of halogens in the NAC. Subducted serpentinite is considered to provide the dominant pathway for the subduction of the heavy halogens Cl, Br and I, hosting up to ~1700 p.p.m. Cl, 6.7 p.p.m. Br and 180 p.p.b. I (Kendrick et al., 2013) with efficiencies of devolatilization of between 90-96% for Cl

and even higher for Br or I (Kendrick et al., 2014b). On this basis serpentine devolatilization could be expected to provide a large enough flux of Cl and Br into the C-SCLM.

Within serpentinized oceanic peridotite the only halogen hosting phases are the polymorphs of serpentine: chrysotile, lizardite and antigorite, which form at varying P/T conditions. Serpentine breakdown is thermally dependent with chysotile and lizardite stable to < 390°C (Schwartz et al., 2013), temperatures reached early in modern subduction systems at depths typically < 30km (depending on the geothermal gradient) far shallower than the expected minimum depth of delivery of halogens expected in the NAC. However, antigorite stability in modern arc systems ranges from 3-7 GPa; i.e. maximum depths > 200km (Ulmer and Trommsdorff, 1995), with greater depth of stability corresponding to cooler subduction geotherms such as might be expected under relatively cool C-SCLM. 7 GPa is likely far in excess of the minimum depth of delivery of recycled halogens in the NAC and the inferred base of the C-SCLM at the southern boundary of the NAC (Wittig et al., 2008). However, significant Cl and Br loss might be expected during the polymorphic transformation of lizardite/chrysotile prior to formation of antigorite. Even so, efficient loss of halogens at the lizardite/chyrsotile to antigorite transformation into the fore arc will only be expected if external fluids are present (e.g. Kodolányi and Pettke, 2011) and halogens can be conserved within newly formed antigorite if external fluid flow is not significant (Kendrick et al., 2013). Furthermore, if antigorite-bearing fore-arc mantle enriched in heavy halogens from fluids released at the lizardite/chrysotile-antigorite transition is subducted, a mechanism inferred to occur in subduction systems on the basis of $\delta^{11}B$ systematics (Tonarini et al., 2011), heavy halogens could be delivered to > 200km depth. The Br/Cl and $\delta^{37}Cl$ values reported here are at the high end of the range of compositions of veins reported for eclogite-facies ophiolites that record early antigorite dehydration. The delivery of Br and Cl via antigorite dehydration in the subducting slab offers the most credible pathway for Br and Cl into the C-SCLM of the NAC; a similar interpretation to Broadley et al., (2016) for the explanation of extreme heavy halogen contents within the C-SCLM underlying the West Antarctic Rift System.

However, F/Cl ratios observed in both UML is significantly enriched compared to fluids recording antigorite dehydration (Figure 14; John et al., 2011). Therefore the F/Cl ratios require an additional F-enriched component. In terms of F contents both UML are comparable to those reported for kimberlite and Lac de Gras, Canada. The similar

petrogenesis of kimberlite and UML could suggest the F/Cl of UML from Nigerdlikasik and Pyramidefjeld is best explained by the mixing of an originally kimberlite-like melt in terms of F/Cl and a low F/Cl and enriched Br and Cl component in the C-SCLM. Such a scenario could adequately explain the depression of the F/Cl observed in both UML to kimberlite at similar F concentrations. In such a scenario the F content of the UML is controlled by melting within the sub-lithospheric mantle and the high Cl and Br contents likely derive from interaction with C-SCLM metasomatised by fluids released during antigorite dehydration during the Ketilidian orogeny.

6.3.5. A role for sediments?

Although relatively little work has been constrained halogen dehydration from sediments at specific P/T conditions during subduction, they appear to show extremely wide variability in bulk F/Cl, Br/Cl, and $\delta^{37}Cl$ compositions, spanning a range that overlaps that of both UML reported here (Figure. 13). Therefore sediment derived halogen fluxes also could offer a credible delivery of Br and Cl into the C-SCLM.

However, sediments are thought to host a relatively small proportion of subducted volatiles in comparison to serpentinite and particularly with respect to Br deep in subduction (Kendrick et al., 2013; Schmidt and Poli, 2013) and the fluid compositions themselves will be dependent on the dominant phase (s) and the specific decomposition P/T conditions of halogen-hosting phases during subduction. Furthermore, as with marine pore-fluids (Figure. 13), subducted sediments are most commonly fractionated toward isotopically negative values (Barnes et al., 2008; Barnes et al., 2009). It would also be expected that should halogen dehydration from sediment should also be coupled with distinctive trace element enrichments in both UML comparable to arc magmas. While UML from Nigerdlikasik display low Ce/Pb and LILE compositions that have a greater affinity to subduction-influenced mafic alkaline magmas such as orogenic lamproites (e.g. Ce/Pb < 10; Prelovic et al., 2008), UML from Pyramidefjeld has by contrast has Ba/Nb of 4.5 and Ce/Pb of 46.5 comparative to UML emplaced elsewhere in the NAC in Greenland with Ce/Pb of ~49 and Ba/Nb of ~5 (Tappe et al., 2011) that are also typical of OIB (Hofmann, 1988). This suggests that the trace-element composition of UML from Pyramidefjeld is largely controlled from low-degree melting of convecting mantle. The variation in whole-rock compositions between UML at Nigerdlikasik and Pyramidefjeld at invariant Br, Cl and $\delta^{37}Cl$ contents suggests that the halogen enrichment of the NAC is decoupled from enrichments and depletions in

incompatible trace element synonymous with subduction. These factors suggest sediments are an unlikely source of halogens in the C-SCLM of the NAC. Such decoupling however, is consistent from the dehydration of antigorite due to its poor hosting of most incompatible trace elements deep into subduction (Kodolányi and Pettke, 2011; Kodolányi et al., 2012). Therefore, the overall enrichment in UML, including F, from Nigerdlikasik relative to Pyramidefjeld at invariant Br and Cl contents and δ^{37}Cl compositions cannot be easily explained in terms of serpentine dehydration. Neither can such variation be explained in terms of variation in degrees of melting in the proto UML melt or greater input of metasomatised C-SCLM due to the similar abundances of compatible elements and the invariant Br and Cl concentrations of both UML. This suggests an additional 'enriched' component within UML from Nigerdlikasik. Accordingly, this variation in trace element composition between both UML must have a negligible effect on their heavy halogen inventories yet exert a strong influence on incompatible trace element compositions.

Such characteristics might be expected through addition of a subducted sediment component. It is notable that the systematic incompatible element enrichment of UML from Nigerdlikasik is also remarkably similar to anorogenic lamproite from Aillik Bay, Canada, and might be best explained in terms of a lamproite-like (e.g. MARID) source component that is absent within the C-SCLM underlying Pyramidefjeld. The similarities of trace-element composition between UML at Nigerdlikasik and the Aillik Bay lamproites strongly suggest an enriched MARID-type source sampled by both as does their similar spatial positions on the southern boundary of the NAC. This interpretation could also explain the F enrichment and correspondingly higher F/Cl of UML from Nigerdlikasik comparative to Pyramidefjeld, since lamproite from Leucite Hills, USA, contains ~7.5wt. % F (Aoki et al., 1981) implying that a lamproite source is F-enriched. The spatial position of Nigerdlikasik relative to Pyramidefjeld, at a greater distance from the suture between the NAC and the Ketilidian Mobile Belt could suggest that the enrichment of the C-SCLM underlying Nigerdlikasik and Aillik Bay might result from a flux of incompatible trace-elements deeper in subduction.

However. it should be stated that Tappe et al., (2007) reject a subduction metasomatism origin for the enriched C-SCLM domain that gave rise to lamproite magmatism at Aillik Bay on the basis of radiogenic isotope systematics. Alternatively, Tappe et al., (2007) suggest the enrichment of the along the southern boundary of the NAC at Aillik Bay is thought to have occurred in two phases, with the first occurring in

the Early Palaeoproterozoic (2.4 – 2.1 Ga) on the basis of the low radiogenic Pb composition of the lamproites in comparison to convective mantle at time of melt extraction and consistently old Nd and Hf depleted mantle model ages. This phase is interpreted to have generated a MARID style metasomatic assemblage with the later formation of a second phase of K-rich lithologies in the C-SCLM underlying Aillik Bay considered to have occurred shortly prior to the lamproite magmatism (between 1.4 and 1.2 Ga) on the basis of moderately radiogenic initial ^{87}Sr / ^{86}Sr that indicate low time-integrated Rb/Sr.

6.3.6. Sensitivity of halogens for tracing subduction metasomatism in the C-SCLM

It is notable that beyond the obvious enrichment in K_2O which requires a K-rich component, UML from Pyramidefjeld are similar to kimberlite *senso stricto* from Maniitsoq, South Greenland, in terms of composition. Whole-rock incompatible trace element compositions of older Gardar period (1.2 Ga) UML also emplaced along the southern margin of the NAC in the Ivigtuut region are also remarkably similar (c.f. Goodenough et al., 2002). Goodenough et al., (2002) argue these UML derive from low-degree volatile-rich melts from the asthenosphere that infiltrated the C-SCLM and were soon after re-melted as a result of ongoing extension. The presence of cotemporaneous basalts that display chemical affinities to arc magmas suggest an influence of a subduction modified C-SCLM along the southern boundary of the NAC. Since UML from Nigerdlikasik and Pyramidefjeld both display a clear subduction signature with respect to Br/Cl and $\delta^{37}Cl$ composition it could suggest that these proxies are particularly sensitive for tracing the presence of subduction metasomatism. The poor capacity of serpentine to host incompatible trace elements, and masking of signatures associated with fluids released from oceanic crust and subducted sediments (e.g. Kodolányi et al., 2012) could explain the lack of obvious influence in terms of traditional tracers of subduction metasomatism within UML at Pyramidefjeld.

Therefore it is argued that the elemental and isotopic halogen composition of C-SCLM xenoliths and their host magmas could offer significant potential in deciphering the metasomatic events (i.e. subduction vs. plume) in other C-SCLM regions.

6.3.7 Halogens in kimberlites and related rocks: implications from UML of South Greenland

There is no reason *a priori* to compare UML from South Greenland and kimberlite from Udachnaya-East field, Siberia, beyond the inference that both originated as carbonated melts within the convecting mantle. However, within the 'ultra-fresh' Udachnaya-East kimberlites, extreme Cl concentrations (up to several wt. %) are shown in melt inclusions, alkali chloride and magmatic halide minerals (Kamenetsky et al., 2004; Kamenetsky et al., 2009a; Kamenetsky et al., 2009b; Giuliani et al., 2012). Although whole-rock Cl contents are not reported, it clearly demonstrates the Cl-enriched character of the Udachnaya-East kimberlite to a far greater degree than UML from Nigerdlikasik and Pyramidefjeld. In conjuncture to direct observations of the Cl-rich nature of the Udachnaya-East kimberlites, several similar Cl-rich phases are reported for other kimberlites from both India (e.g. Parthasarathy et al., 2002) and Canada (e.g. Watkinson and Chao, 1973; Clarke et al., 1994). The Cl-rich nature of the Udachnaya-East kimberlites led Kamenetsky et al., (2014) to suggest a petrogenetic model for kimberlite originating as a dry convective mantle melt rich in Na and Cl. The exceptional Cl contents of the Udachnaya-East kimberlites is nonetheless contentious and been contended to reflect significant crustal assimilation of a 2km-thick succession of evaporite-bearing carbonate sediments that the kimberlites of Udachnaya-East erupt though and are emplaced within (e.g. Kopylova et al., 2013; Kopylova et al., 2016). Such controversy aside, several useful observations about kimberlite and UML can be made on the basis of the UML of South Greenland. As stated $\delta^{37}Cl$ compositions of C-SCLM phlogopite from xenolith NX-01 from Nigerdlikasik are remarkably similar and statistically indistinguishable to whole-rock $\delta^{37}Cl$ of its host UML and clearly more enriched in ^{37}Cl than melts that derive from the convecting mantle which do not sample an enriched EM-I or EM-II reservoir. On this basis the similarity of $\delta^{37}Cl$ could only have be conserved into the UML during remelting of phlogopite metasomes in the C-SCLM if; (i) the early convective upper mantle UML melt had relatively small Cl contents comparative to the assimilated C-SCLM, or (ii) the early UML melt sampled an EM-I or EM-II reservoir with a complementary $\delta^{37}Cl$ composition. The additional sampling of a + $\delta^{37}Cl$ EM-I or EM-II reservoir in the convecting mantle in addition to the high Br/Cl + $\delta^{37}Cl$ component in the C-SCLM requires a complex and specific sampling of two separate recycled reservoirs that cannot be evaluated here. Nonetheless, it should be stated that such strong Cl-enrichment is not observed in other kimberlite for

which whole-rock Cl data is available (e.g. Lac de Gras; Kjarsgaard et al., 2009) which could imply (i) is more likely. This would suggest in opposition to recent conventional thought (e.g. Kamenetsky et al., 2004; Kamenetsky et al., 2009a; Kamenetsky et al., 2014; Kamenetsky et al., 2015) early convective upper mantle melts that give rise to kimberlite and UML magmatism might not particularly Cl-rich and that these budgets have not necessarily been remobilized after emplacement (e.g. Abersteiner et al., 2017).

6.3.8. Review of the subduction model

Whole-rock halogen data of both UML suggests a scenario in which fluids released from serpentinized oceanic peridotite during antigorite dehydration of an oceanic slab at ~1.8 Ga percolated into the overlying C-SCLM forming Br and Cl-enriched metasomes. These metasomes were assimilated into subsequent UML magmas, and imprinted their Br/Cl and δ^{37}Cl characteristics onto those magmas. Such a scenario is consistent with work from Köhler et al., (2009) that suggests that the SCLM along the southern margin of the NAC and adjoining Ketilidian mobile belt is halogen enriched from subduction processes in the Ketilidian orogeny.

The High F/Cl of both UML comparative to fluids released from antigorite dehydration indicate an additional high F component in their petrogenesis. The F contents of both UML are comparable to those reported for kimberlite and suggest control via melting in the convecting mantle, or possibly the transition zone. This implies in the context of UML from Nigerdlikasik and Pyramidefjeld, F/Cl systematics result from simple mixing of a kimberlite-like melt in terms of halogen contents and a low F/Cl, Cl-Br enriched C-SCLM metasomatic component.

A corollary point however could be made about the potential secular variation of halogen composition of the Earth's oceans through time. It is argued that the Earth has remained in a state of near constant continual transfer of halogens (as implied from Cl) from mantle to crust (e.g. Jambon et al., 1995). In such a scenario would be therefore expected that the halogen composition of the Earth's ocean would remain constant. However, the generation and deposition of extensive salt deposits at ~200 Ma and ~ 550 Ma in the Phanerozoic imply that the pre-Cambrian oceans could have been significantly more saline (Knauth, 2005). Halogen metasomatism below the southern margin of the NAC, if inferred to result from slab-derived fluids during the Ketilidian orogeny at ~ 1.8 Ga, would therefore be unlikely to reflect halogen fluxes across modern-day subduction zones. Thus, the halogen composition of slab-derived fluids

could be a significantly more potent metasomatic agent in the pre-Cambrian eras in the mantle than today.

6.4. Evidence of metasomatism from xenoliths

A more complex history of metasomatism is provided by in-situ major and trace element analysis of metasomatic phases within mantle xenoliths recovered from Nigerdlikasik than is advocated from whole-rock major, trace and halogen data. Intergrown clinopyroxene and phlogopite from Nigerdlikaisk display systematics that appear reconcilable with both MARID and PIC origins (Figures. 19; 20; 22), despite the fact that these mineral assemblages are considered to form under different conditions based on their contrasting radiogenic isotope compositions (e.g. Figure. 1).

Clinopyroxene analysed in samples NX-02 and NX-03 display REE systematics consistent with Type-I clinopyroxene from PIC assemblages, yet NX-03 also displays several incompatible trace element characteristics comparable to Type-II clinopyroxene from MARID assemblages (e.g. strong Nb-Ta anomalies and suprachondritic Nb/Ta). Phlogopite from samples NX-01 and NX-03 also displays major and HFSE systematics that are comparable to both PIC and MARID assemblages. Both samples display high Nb/Ta that is also mirrored in MARID rocks from the Kaapvaal craton (Giuliani et al., 2015) as well as the whole-rock Nb/Ta of UML from Nigerdlikasik which also closely matches the suprachondritic Nb/Ta of lamproites at Aillik Bay. It is generally argued that suprachondritic Nb/Ta can be generated with the addition of a carbonatitic metasomatic agent to C-SCLM (Rudnick et al., 1993; Yaxley et al., 1998) an agent often invoked for PIC-style metasomatism. However, such a scenario would require an unrealistically large addition of a carbonatitic or carbonate-rich melt (ca. 10%) and also increase Zr/Hf, albeit at a lesser degree than Nb/Ta, which is not observed in any phlogopite population (Figure. 22). Furthermore, the strongly diverging Nb/Ta and Zr/Hf ratios observed in phlogopite from samples NX-01 and NX-03 cannot not be explained in terms of carbonate-silicate immiscibility since both Nb and Zr favor the silicate liquid over a carbonate liquid (Veksler et al., 1998).

It can be inferred that a MARID-type assemblage could be sampled by UML at Nigerdlikasik as is suggested by whole-rock data and that its composition likely reflects that of the original metasomatic agent. Nonetheless, this MARID-type assemblage in the C-SCLM is likely to have metasomatised by an agent in at least partial equilibrium with a PIC-type juvenile metasomatic agent, as inferred by the REE compositions of

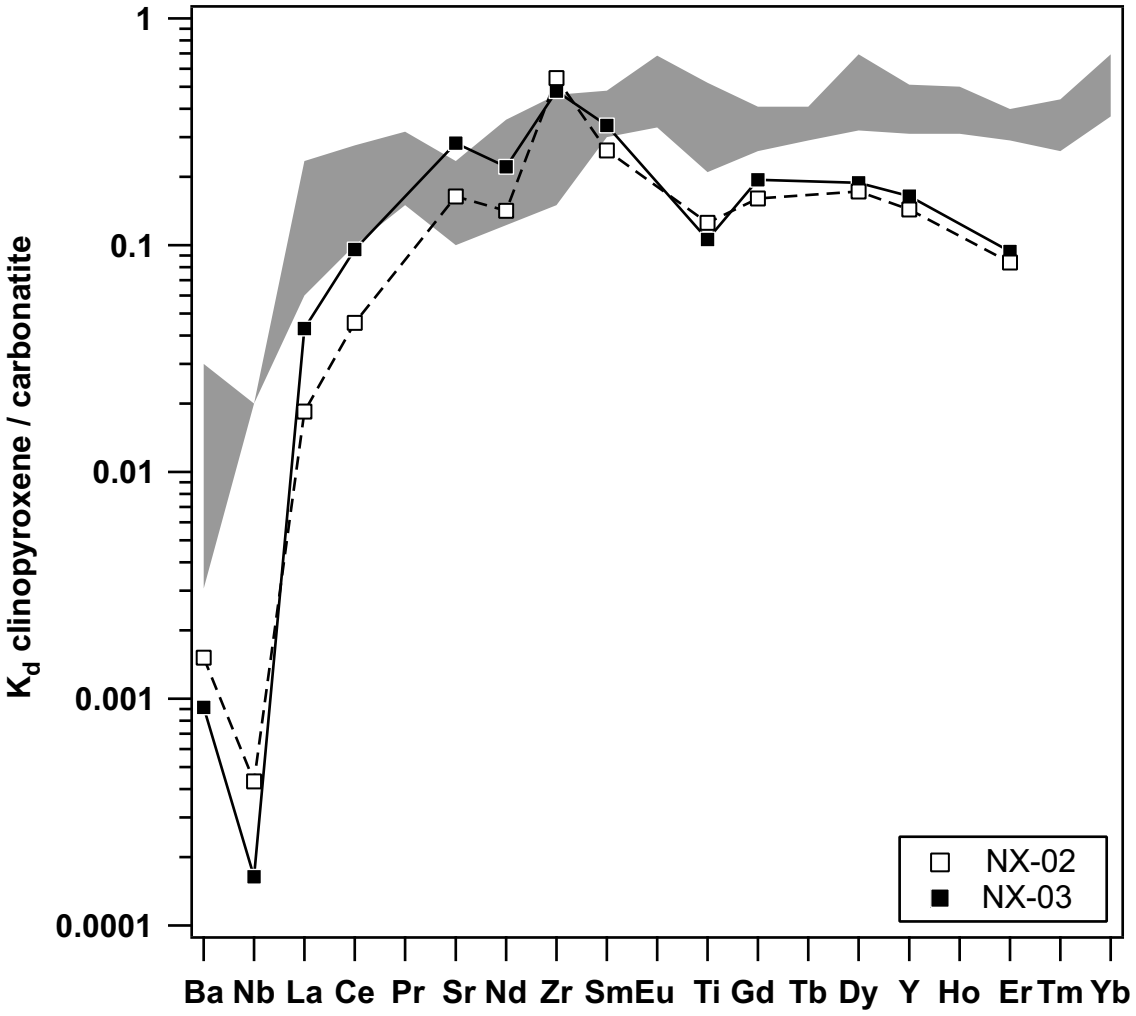

Figure 27: Clinopyroxene / carbonatite distribution coefficients (Kd) between clinopyroxene from xenoliths NX-02 and NX-03 from Nigerdlikasik and carbonatite from Coltorti et al., (1999). Shaded field shows the range in distribution coefficients (Kd) reported by Coltorti et al., (1999)

clinopyroxene in both NX-02 and NX-03. Such an interpretation is supported by calculated clinopyroxene / carbonatite K_d values for both xenoliths (Figure. 27) which show a reasonably good agreement with those reported by Coltorti et al., (1999), albeit with the slightly stronger depletions in Nb and Ti a likely result of equilibrium with nearby phlogopite or ilmenite. A MARID assemblage later modified by a juvenile PIC like metasomatic agent has been suggested previously, with both petrographic and isotopic evidence of xenoliths provided for such a scenario from the C-SCLM of the Kaapvaal Craton (c.f. Choukroun et al., 2005). It should be stated that such a series of events can also be consistent and reconcilable with UML petrogenesis (Tappe et al., 2004; Tappe et al., 2006; Tappe et al., 2008; Tappe et al., 2009; Tappe et al., 2011).

However, the + 1.3 δ^{37}Cl of phlogopite from NX-01 that manifest MARID characteristics demonstrate that that the trace-element enriched character of UML at Nigerdlikasik appears intimately linked to subduction metasomatism and provides at least direct evidence for the potential of subduction metasomatism in the generation of, or retention within, MARID metasomes. This interpretation is also supported by recent δ^{15}N isotope data for phlogopite from the Kaapvaal that also provides evidence for a subduction origin for the MARID suite (Banerjee et al., 2015). Therefore if lamproites from Aillik Bay and UML from Nigerdliaksik share a similarly formed MARID source component, subduction metasomatism is likely to have at least influenced the composition of lamproites from Aillik Bay. Conversely, it is possible that lamproite from Aillik Bay and UML from Nigerdlikasik sample a different MARID domain within the C-SCLM of the NAC, formed by different processes albeit with similar compositions, as would be inferred by the radiogenic isotope compositions of the Aillik Bay lamproites. In either scenario, the lack of such enrichment in UML from Pyramidefjeld suggests that the C-SCLM of the southern margin of the NAC is spatially heterogeneous. It is also notable that metasomatic phases analyzed within the xenolith recovered from UML at Pyramidefjeld (PX-01) manifest no MARID-type geochemical characteristics and mostly resemble those of the PIC population. This, it should be argued, is expected due to the absence of such characteristics in whole-rock geochemical data for UML from Pyramidefjeld. It should be stated clearly that the NAC illustrates the limitations in analyzing a small subset of incompatible trace elements (e.g. REE in clinopyroxene) with the intention of extracting a metasomatic history for C-SCLM domains.

Further evidence of metasomatism of the C-SCLM of the NAC is suggested by an overall enrichment of FeO within the NAC. Olivine recovered in both xenoliths and as xenocrysts within both UML display widely variable FeO contents with Mg# ranging from 84 – 93. Generally the Mg# of worldwide C-SCLM displays a strong mode of Mg# at 92.5 (e.g. Bernstein et al., 2007). Wittig et al.,(2008) found FeO enriched xenoliths in the NAC with olivine Mg# < 91, which were argued to be inconsistent with polybaric fractional melting and that the high bulk FeO contents of their host peridotite and must be a feature of metasomatism at increasing mantle depth. Significantly, the high FeO contents of these xenoliths requires a varying process from that of olivine-orthopyroxene SiO_2 melt reactions (Figure. 18) that generated the low FeO observed in Kaapvaal craton (e.g. Walters, 2003; Lee, 2006). Of olivine recovered from UML there is a strong mode of olivine Mg# between 91.5 and 92.5 (Figure. 15); slightly lower than the ultra-depleted olivine observed within the NAC at Ubekendt Eijland, but comparable to C-SCLM olivine from Wiedemann Fjord (Bernstein et al., 1998; Bernstein et al., 2006). The modal Mg# of olivine in the UML suggest that depleted olivine (Mg# ~92) is by far the most common constituent of the C-SCLM of the NAC. By contrast Mg# of olivine within xenoliths are most commonly < 90 that display obvious recrystallization textures and generation of neoblastic olivine and introduction of modal metasomatic phases (e.g. phlogopite). FeO enrichment of the NAC appears inconsistent with metasomatism related with UML emplacement due to the contrastingly highly magnesian nature of sub-lithospheric melts. This is supported by the Mg# of olivine in recovered in xenoliths and as xenocrysts entrained within UML, which largely plot outside the range of Mg# and NiO of the inferred early melt composition as preserved in olivine rims (Mg# ~90.5). Evidence of periodic FeO melt enrichment during the evolution of the UML is also implied by an Mg# 87 overgrowth shown in Figure. 7e, which displays complex FeO zonation in olivine. Complex FeO zonation in olivine is also observed in other alkaline-ultramafic rocks and is not unique to the NAC (e.g. Kamenetsky et al., 2008). This might feasibly result from episodic FeO enrichment of the UML during assimilation of a variably FeO enriched C-SCLM during formation. Should this result from subduction metasomatism or infiltration of FeO-enriched convecting mantle melts it would be implied to be a bottom up mechanism, with the most pervasive metasomatism occurring at greatest depths in the C-SCLM. However, the most pervasively metasomatised sample appears at < 100 km depth (e.g. NX-03) as implied by the presence of antigorite. It appears that metasomatism must

have been localized, perhaps along vein networks within the C-SCLM (which are common to most xenoliths) that reaches even the shallowest C-SCLM.

6.5. Petrogenesis of the Nigerdlikasik and Pyramidefjeld UML suites

The data presented here suggests a complex melting history of upwelling of convecting upper mantle with complex C-SCLM components and metasomatism driven by fluids released from a subducting slab. Petrogenesis of the Nigerdlikasik and Pyramidefjeld UML suites are illustrated in Figure 28a and 28b and support the following scenario:

1) Subduction metasomatism and halogen enrichment of the southern margin of the NAC from fluids released at antigorite dehydration within a subducting oceanic slab beneath the NAC at ~1.8 Ga. This metasomatism was likely highly channelized (i.e. not pervasive) as is suggested by the modal abundances of xenocrystic olivine recovered from both UML with high Mg# average of ~ 92.

2) Low-degree CO_2-rich melts formed in response to the lithospheric attenuation of the NAC in the early stages of the opening of the Labrador Sea assimilated subduction-derived halogens later freezing as complex hybrid vein networks in the C-SCLM.

3) Continued lithospheric attenuation in the NAC (~150 Ma) subsequently drives re-melting of the relatively juvenile PIC-like components inducing volatile-fluxed melting of the surrounding halogen-enriched wall-rock. At Nigerdlikasik an additional MARID component is present in the C-SCLM of the NAC which is sampled during wall-rock assimilation (e.g. Foley, 1992).

This scenario for the genesis of both Nigerdlikasik and Pyramidefjeld UML suites is similar to the mechanism suggested for the generation of the Torngat and Aillik Bay UML suites on the Canadian portion of the NAC (Tappe et al., 2007; Tappe et al., 2008) and for UML from Sarfartoq on the Northern boundary of the NAC in Greenland (Tappe et al., 2011).

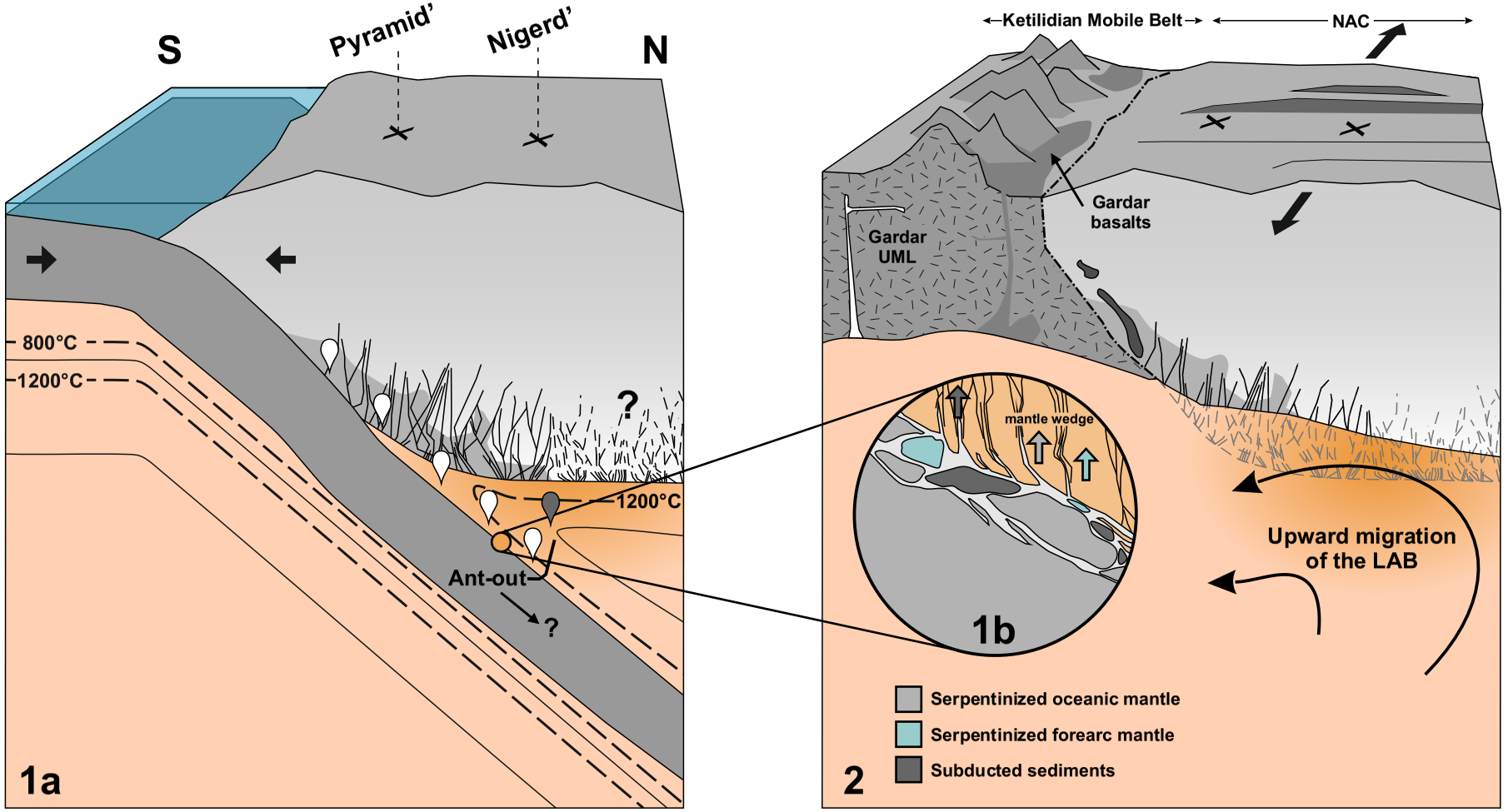

Figure 28a: Schematic displaying the evolution of the North Atlantic Craton (NAC) through time. 1a displays the NAC at ~1.8 Ga with the ongoing subduction of oceanic slab from the South. Potential sources for fluids liberated from the oceanic slab is shown (1b); with sepentinized oceanic lithosphere (grey), metasomatised forearc mantle (blue) and a potential additional sedimentary source (e.g. sediments; dark grey) implied for Nigerdlikasik. 1b displays the NAC during extension and rifting associated with the opening of the Labrador Sea (~150 Ma), upward migration of the lithosphere-asthenosphere boundary (LAB) and localization of low-degree melts into the cratonic sub-continental lithospheric mantle (C-SCLM). Gardar magmatism is shown demonstrating the migration of UML magmatism into the craton interior through time.

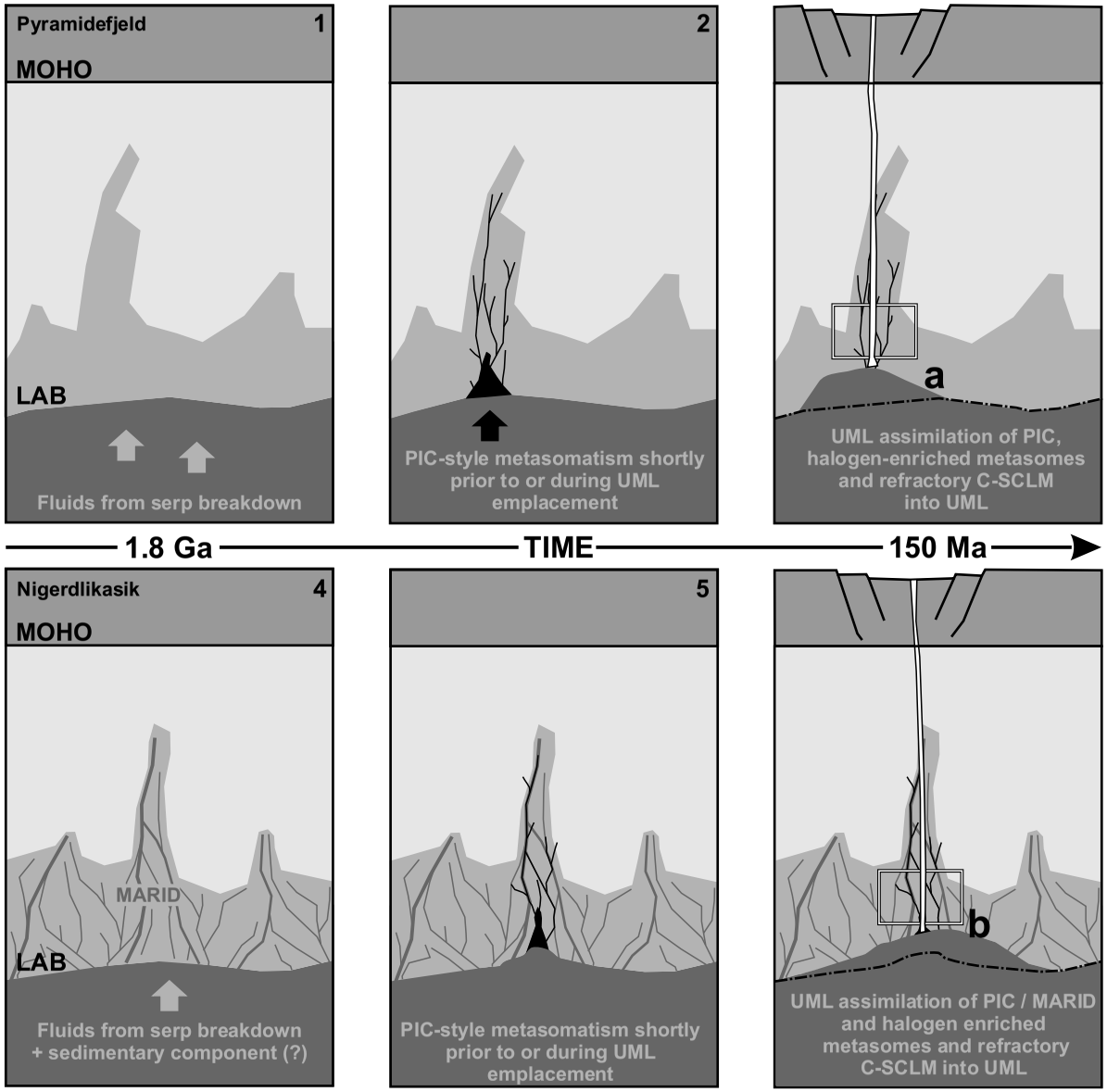

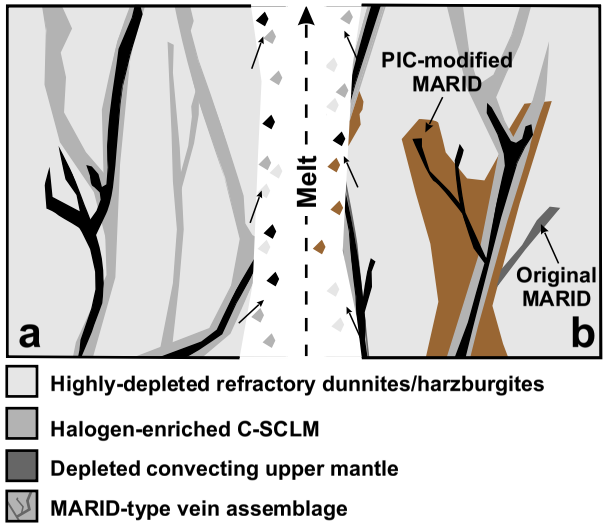

Figure 29b: Schematic of the evolution of the cratonic sub-continental lithospheric mantle (C-SCLM) of the southern boundary of the North Atlantic Craton (NAC) through time. Panels 1-3 depict the C-SCLM underlying Pyramidefjeld. Panel 1 shows the highly depleted refractory C-SCLM of the NAC metasomatised by trace-element depleted fluids released from serpentine breakdown in the oceanic slab below the NAC at ~ 1.8 Ga. Panel 2 displays PIC-style metasomatism of the C-SCLM shortly prior to or during ultramafic lamprophyre (UML) emplacement. Panel 3 depicts the emplacement of the UML into the C-SCLM and assimilation/sampling of pre-existing highly depleted C-SCLM and preconditioned metasomatic C-SCLM. Panels 4-6 display the same scenario for Nigerdlikasik. The scenario for Nigerdlikasik deviates from that of Pyramidefjeld in that a pre-existing MARID or additional subducted sedimentary component that lead to formation of a MARID type assemblage, is present. This domain is subsequently metasomatised prior to or during emplacement generating a complex assemblage that manifests both PIC and MARID characteristics.

7.0 Synthesis

Over the last decade the halogen elements have emerged as a powerful geochemical tracer for volatile recycling in the Earth's convecting mantle. Yet their application to volatile recycling in the Earth's C-SCLM, which is isolated from mantle convection, remains poorly utilized. Volatiles introduced into the C-SCLM drive metasomatism, ultramafic magmatism and diamond formation, yet the source of these volatiles, their abundance and residence in the C-SCLM is poorly unconstrained. The overwhelming concentration of the halogen elements in the Earth's surficial reservoirs suggest that the investigation of the halogen inventory of intra-plate continental magmatism and their hosted C-SCLM xenoliths could offer significant potential in the discrimination of metasomatic agents acting on C-SCLM.

The investigation of the halogen composition of ultramafic lamprophyre (UML) provide an excellent opportunity to elucidate the provenance of metasomatic agents in the C-SCLM. UML are formed by low-degree carbonated asthenospheric melts formed in response to rifting which interacts with cold variably enriched overlying cratonic lithosphere. This generates hybrid magmas of C-SCLM and convecting upper mantle components. The nominal depletion of halogens in the convecting mantle suggest that UML are exceptionally sensitive to the addition of halogens from C-SCLM. This thesis provides the first combined elemental (F, Cl and Br) and isotopic (δ^{37}Cl) investigation into intra-plate continental magmatism through the study of two Jurassic ultramafic lamprophyres from Nigerdlikasik and Pyramidefjeld, South Greenland. The principal contributions and conclusions of this thesis in the context of halogen geochemistry can be summarized as four core findings:

Finding #1: Halogen compositions of UML at Nigerdlikasik and Pyramidefjeld have been influenced by interaction with subduction metasomatised C-SCLM along the southern margin of the NAC

Investigation of whole-rock elemental and isotopic compositons of UML from Nigerdlikasik and Pyramidefjeld and their hosted C-SCLM xenoliths suggest that Br and Cl were delivered to the C-SCLM of the NAC via from fluids/melts released from serpentinized oceanic peridotite during antigorite dehydration. This is likely linked to the subduction of an oceanic plate from the South at 1.8 Ga and subsequent formation of the Ketilidian Mobile Belt. Such a scenario is consistent with work from Köhler et

al., (2009), which suggests that the SCLM along the southern margin of the NAC and adjoining Ketilidian mobile belt is enriched from subduction processes in the Ketilidian orogeny. The high F/Cl of both UML comparative to fluids released during antigorite dehydration but low F/Cl comparative to kimberlite likely results from the mixing of an originally kimberlite-like melt in terms of F/Cl and a low F/Cl enriched Br and Cl component in the C-SCLM.

Finding #2: The C-SCLM of the southern margin of the NAC is spatially heterogeneous

UML from Pyramidefjeld are typical of those emplaced elsewhere in the NAC in terms of mantle incompatible trace element compositions. By contrast, UML from Nigerdlikasik closely match 1.2 Ga lamproites also emplaced along the southern boundary of the NAC at Aillik Bay, Canada. The chemical composition of UML from Nigerdlikasik could sample a MARID type source. The spatial position of UML at Nigerdlikasik relative to those from Pyramidefjeld could suggest the trace element enriched source sampled by UML at Nigerdlikasik might reflect a flux of incompatible trace elements released at greater depth in subduction (e.g. from subducted sediments) in addition to fluids released during antigorite dehydration. The similarities of trace-element composition between UML at Nigerdlikasik and the Aillik Bay lamproites could demonstrate an as yet unrecognized link between the lamproite source region at Aillik Bay and subduction metasomatism. However, in the absence of halogen data for the Aillik Bay lamproites the link is equivocal. The $\delta^{37}Cl$ composition of MARID type phlogopite from xenolith NX-01 entrained within UML at Nigerdlikasik clearly demonstrates the potential of the formation, or retention, of subducted volatiles in the MARID suite as already implied on the basis of $\delta^{15}N$ systematics of MARID xenoliths.

Finding #3: Halogens can be effectively decoupled from traditional trace element proxies traditionally used to discriminate subduction metasomatism

The constancy of Br/Cl and $\delta^{37}Cl$ compositions between UML at Nigerdlikasik and Pyramidefjeld yet strong variation in incompatible trace element compositions suggest halogens released during antigorite dehydration can be effectively decoupled from traditional indicators used in the discrimination of subduction metasomatism and may remain undetected in continental intraplate magmatism (c.f. Goodenough et al., 2002).

Such a scenario is consistent with the dilution of trace-element signatures synnonmous with serpentine dehydration by fluids released by AOC and marine sediments in modern subduction zones (Kodolányi et al., 2012).

Finding #4: The elemental and isotopic elemental composition of C-SCLM xenoliths and their host magmas offer potential for isolating subduction vs. plume metasomatism

The highly contrasting elemental and isotopic halogen composition of the lithologies comprising the Earth's crust and mantle suggest that the halogen elements are an effective tracer of subduction metasomatism in C-SCLM. Therefore C-SCLM xenoliths and their host magmas could offer significant potential in deciphering metasomatic events (i.e. subduction vs. plume) in the C-SCLM. It also follows that the halogen elements could offer significant insight into the debate concerning formation models of C-SCLM (i.e. Archaean shallow-slab subduction and slab imbrication vs. a refractory residue after high-degrees of melting in a plume).

References

Abersteiner, A., Kamenetsky, V.S., Kamenetsky, M., Goemann, K., Ehrig, K., and Rodemann, T., 2017, Significance of halogens (F, Cl) in kimberlite melts: Insights from mineralogy and melt inclusions in the Roger pipe (Ekati, Canada): Chemical Geology, , no. May, p. 0–1, doi: 10.1016/j.chemgeo.2017.06.008.

Aiuppa, A., Baker, D.R., and Webster, J.D., 2009, Halogens in volcanic systems: Chemical Geology, v. 263, no. 1–4, p. 1–18, doi: 10.1016/j.chemgeo.2008.10.005.

Allègre, C., Manhes, G., and Lewin, E., 2001, Chemical composition of the Earth and the volatility control on\rplanetary genetics: Earth and Planetary Science Letters, v. 185, p. 49–69.

Allègre, C.J., Poirier, J.-P., Humler, E., and Hofmann, A.W., 1995, The Chemical Composition of the Earth: Earth and Planetary Science Letters, v. 134, no. 3–4, p. 512–526, doi: 10.1098/rspa.1980.0106.

Allen, R.O.J., and Reed, G.W.J., 1965, Cl, Br and I in chondrites: Eos, v. 46, p. 123–124.

Anderson, D.L., 1983, Chemical composition of the mantle: Journal of Geophysical Research: Planets, v. 88, no. S01.

Andrews, J.R., and Emeleus, C.H., 1971, Preliminary account of kimberlite intrusions from the Frederikshtb district, South-West Greenland: Rapp. Grznlands Geol. Unders., no. 31, p. 1– 28.

Andrews, J.R., and Emeleus, C.H., 1975, Structural aspects of kimberlite dyke and sheet intrusion in south-west Greenland: Physics and Chemistry of the Earth, v. 9, no. C, p. 43–50, doi: 10.1016/0079-1946(75)90005-1.

Aoki, K., Ishiwaka, K., and Kanisawa, S., 1981, Fluorine geochemistry of basaltic rocks from continental and oceanic regions and petrogenetic application: Contributions to Mineralogy and Petrology, v. 76, no. 1, p. 53–59, doi: 10.1007/BF00373683.

Armytage, R.M.G., Jephcoat, A.P., Bouhifd, M.A., and Porcelli, D., 2013, Metal-silicate partitioning of iodine at high pressures and temperatures: Implications for the Earth's core and 129*Xe budgets: Earth and Planetary Science Letters, v. 373, p. 140–149, doi: 10.1016/j.epsl.2013.04.031.

Aulbach, S., Griffin, W.L., Pearson, N.J., and O'Reilly, S.Y., 2013, Nature and timing of metasomatism in the stratified mantle lithosphere beneath the central Slave

craton (Canada): Chemical Geology, v. 352, p. 153–169, doi: 10.1016/j.chemgeo.2013.05.037.

Aulbach, S., O'Reilly, S.Y., and Pearson, N.J., 2011, Constraints from eclogite and MARID xenoliths on origins of mantle Zr/Hf-Nb/Ta variability: Contributions to Mineralogy and Petrology, v. 162, no. 5, p. 1047–1062, doi: 10.1007/s00410-011-0639-y.

Banerjee, S., Kyser, T.K., and Mitchell, R., 2015, Nitrogen isotopic compositions and concentrations in MARID xenoliths: Chemical Geology, v. 391, p. 83–89, doi: 10.1016/j.chemgeo.2014.11.003.

Barnes, J.D., and Sharp, Z.D., 2006, A chlorine isotope study of DSDP/ODP serpentinized ultramafic rocks: Insights into the serpentinization process: Chemical Geology, v. 228, no. 4, p. 246–265, doi: 10.1016/j.chemgeo.2005.10.011.

Barnes, J.D., and Sharp, Z.D., 2017, Chlorine Isotope Geochemistry: Reviews in Mineralogy and Geochemistry, v. 82, no. 1, doi: 10.2138/rmg.2017.82.9.

Barnes, J.D., Sharp, Z.D., Fischer, T.P., Barnes, J.D., Sharp, Z.D., and Fischer, T.P., 2008, Chlorine isotope variations across the Izu-Bonin-Mariana arc: Geology, doi: 10.1130/G25182A.1.

Barnes, J.D., Sharp, Z.D., Fischer, T.P., Hilton, D.R., and Carr, M.J., 2009, Chlorine isotope variations along the Central American volcanic front and back arc: Geochemistry, Geophysics, Geosystems, v. 10, no. 11, doi: 10.1029/2009GC002587.

Bell, D.R., Grégoire, M., Grove, T.L., Chatterjee, N., Carlson, R.W., and Buseck, P.R., 2005, Silica and volatile-element metasomatism of Archean mantle: A xenolith-scale example from the Kaapvaal Craton: Contributions to Mineralogy and Petrology, v. 150, no. 3, p. 251–267, doi: 10.1007/s00410-005-0673-8.

Belousova, E.A., Walters, S., Griffin, W.L., and O'Reilly, S.Y., 2001, Trace-element signatures of apatites in granitoids from the Mt Isa Inlier, Northwestern Queensland: Australian Journal of Earth Sciences, v. 48, no. 4, p. 603–619, doi: 10.1046/j.1440-0952.2001.00879.x.

Bernstein, S., Hanghøj, K., Kelemen, P.B., and Brooks, C.K., 2006, Ultra-depleted, shallow cratonic mantle beneath West Greenland: Dunitic xenoliths from Ubekendt Ejland: Contributions to Mineralogy and Petrology, v. 152, no. 3, p. 335–347, doi: 10.1007/s00410-006-0109-0.

Bernstein, S., Kelemen, P.B., and Brooks, C.K., 1998, Depleted spinel harzburgite xenoliths in Tertiary dykes from East Greenland: Restites from high degree melting: Earth and Planetary Science Letters, v. 154, no. 1–4, p. 221–235, doi: 10.1016/S0012-821X(97)00175-1.

Bernstein, S., Kelemen, P.B., and Hanghøj, K., 2007, Consistent olivine Mg# in cratonic mantle reflects Archean mantle melting to the exhauston of orthopyroxene: Geology, v. 35, no. 5, p. 459–462, doi: 10.1130/G23336A.1.

Beyer, C., Klemme, S., Wiedenbeck, M., Stracke, A., and Vollmer, C., 2012, Fluorine in nominally fluorine-free mantle minerals: Experimental partitioning of F between olivine, orthopyroxene and silicate melts with implications for magmatic processes: Earth and Planetary Science Letters, v. 337–338, p. 1–9, doi: 10.1016/j.epsl.2012.05.003.

Bonifacie, M., Jendrzejewski, N., Agrinier, P., Humler, E., Coleman, M., and Javoy, M., 2008, The Chlorine Isotope Composition of Earth's Mantle: Science, v. 319, no. 5869, p. 1518–1520.

Boyd, F.R., 1989, Compositional distinction between oceanic and cratonic lithosphere: Earth and Planetary Science Letters, v. 96, no. 1–2, p. 15–26, doi: 10.1016/0012-821X(89)90120-9.

Boyd, F.R., Pearson, D.G., and Mertzman, S.A., 1999, Spinel-facies peridotites from the Kaapvaal Root: Proceedings of the 7th International Kimberlite Conference

Brett, R.C., Russell, J.K., and Moss, S., 2009, Origin of olivine in kimberlite: Phenocryst or impostor? Lithos, v. 112, p. 201–212, doi: 10.1016/j.lithos.2009.04.030.

Brey, G.P., Bulatov, V.K., Girnis, A. V., and Lahaye, Y., 2008, Experimental melting of carbonated peridotite at 6-10 GPa: Journal of Petrology, v. 49, no. 4, p. 797–821, doi: 10.1093/petrology/egn002.

Bridgwater, D., 1970, A compilation of K/Ar age determinations on rocks from Greenland carried out in 1969: Rapp. Grenlands Geol. Unders., no. 28, p. 47–55.

Broadley, M.W., Ballentine, C.J., Chavrit, D., Dallai, L., and Burgess, R., 2016, Sedimentary halogens and noble gases within Western Antarctic xenoliths: Implications of extensive volatile recycling to the sub continental lithospheric mantle: Geochimica et Cosmochimica Acta, v. 176, p. 139–156, doi: 10.1016/j.gca.2015.12.013.

Bureau, H., Keppler, H., and Métrich, N., 2000, Volcanic degassing of bromine and iodine: Experimental fluid/melt partitioning data and applications to stratospheric chemistry: Earth and Planetary Science Letters, v. 183, no. 1–2, p. 51–60, doi: 10.1016/S0012-821X(00)00258-2.

Burgess, R., Cartigny, P., Harrison, D., Hobson, E., and Harris, J., 2009, Volatile composition of microinclusions in diamonds from the Panda kimberlite, Canada: Implications for chemical and isotopic heterogeneity in the mantle: Geochimica et Cosmochimica Acta, v. 73, no. 6, p. 1779–1794, doi: 10.1016/j.gca.2008.12.025.

Burgess, R., Layzelle, E., Turner, G., and Harris, J.W., 2002, Constraints on the age and halogen composition of mantle fluids in Siberian coated diamonds: Earth and Planetary Science Letters, v. 197, no. 3–4, p. 193–203, doi: 10.1016/S0012-821X(02)00480-6.

Bussweiler, Y., Foley, S.F., Prelević, D., and Jacob, D.E., 2015, The olivine macrocryst problem: New insights from minor and trace element compositions of olivine from Lac de Gras kimberlites, Canada: Lithos, v. 220–223, p. 238–252, doi: 10.1016/j.lithos.2015.02.016.

Chadwick, B., and Garde, A.A., 1996, Palaeoproterozoic oblique plate convergence in South Greenland : a reappraisal of the Ketilidian Orogen: Precambrian Crustal Evolution in the North Atlantic Region, , no. 112, p. 179–196, doi: 10.1144/GSL.SP.1996.112.01.10.

Chakhmouradian, A.R., 2006, High-field-strength elements in carbonatitic rocks: Geochemistry, crystal chemistry and significance for constraining the sources of carbonatites: Chemical Geology, v. 235, no. 1–2, p. 138–160, doi: 10.1016/j.chemgeo.2006.06.008.

Chavrit, D., Burgess, R., Sumino, H., Teagle, D.A.H., Droop, G., Shimizu, A., and Ballentine, C.J., 2016, The contribution of hydrothermally altered ocean crust to the mantle halogen and noble gas cycles: Geochimica et Cosmochimica Acta, v. 183, p. 106–124, doi: 10.1016/j.gca.2016.03.014.

Chiaradia, M., Barnes, J.D., and Cadet-Voisin, S., 2014, Chlorine stable isotope variations across the Quaternary volcanic arc of Ecuador: Earth and Planetary Science Letters, v. 396, p. 22–33, doi: 10.1016/j.epsl.2014.03.062.

Choukroun, M., O'Reilly, S.Y., Griffin, W.L., Pearson, N.J., and Dawson, J.B., 2005, Hf isotopes of MARID (mica-amphibole-rutile-ilmenite-diopside) rutile trace

metasomatic processes in the lithospheric mantle: Geology, v. 33, no. 1, p. 45–48, doi: 10.1130/G210841.1.

Chu, M.F., Wang, K.L., Griffin, W.L., Chung, S.L., O'Reilly, S.Y., Pearson, N.J., and Iizuka, Y., 2009, Apatite composition: Tracing petrogenetic processes in Transhimalayan granitoids: Journal of Petrology, v. 50, no. 10, p. 1829–1855, doi: 10.1093/petrology/egp054.

Clarke, D.B., Mitchell, R.H., Chapman, C.A.T., and Mackay, R.M., 1994, Occurrence and origin of djerfisherite from the Elwin Bay kimberlite, Somerset Island, Northwest Territories: Canadian Mineralogist, v. 32, no. 4, p. 815–823.

Clay, P.L., Burgess, R., Busemann, H., Ruzié-Hamilton, L., Joachim, B., Day, J.M.D., and Ballentine, C.J., 2017, Halogens in chondritic meteorites and terrestrial accretion: Nature, v. 551, no. 7682, p. 614–618, doi: 10.1038/nature24625.

Clement, C.R., 1982, A comparitive geological study of some major kimberlite pipes in the Northern Cape and Orange Free State.

Coltorti, M., Bonadiman, C., Hinton, R.W., Siena, F., and Upton, B.G.J., 1999, Carbonatite Metasomatism of the Oceanic Upper Mantle : Evidence from Clinopyroxenes and Glasses in Ultramafic Xenoliths of Grande Comore , Indian Ocean: Journal of Petrology, v. 40, no. 1, p. 133–165, doi: 10.1093/petroj/40.1.133.

Crépisson, C., Blanchard, M., Bureau, H., Sanloup, C., Withers, A.C., Khodja, H., Surblé, S., Raepsaet, C., Béneut, K., Leroy, C., Giura, P., and Balan, E., 2014, Clumped fluoride-hydroxyl defects in forsterite: Implications for the upper-mantle: Earth and Planetary Science Letters, v. 390, p. 287–295, doi: 10.1016/j.epsl.2014.01.020.

Dalou, C., Koga, K.T., Le Voyer, M., and Shimizu, N., 2014, Contrasting partition behavior of F and Cl during hydrous mantle melting: implications for Cl/F signature in arc magmas: Progress in Earth and Planetary Science, v. 1, no. 1, p. 26, doi: 10.1186/s40645-014-0026-1.

Dasgupta, R., Hirschmann, M.M., McDonough, W.F., Spiegelman, M., and Withers, A.C., 2009, Trace element partitioning between garnet lherzolite and carbonatite at 6.6 and 8.6 GPa with applications to the geochemistry of the mantle and of mantle-derived melts: Chemical Geology, v. 262, no. 1–2, p. 57–77, doi: 10.1016/j.chemgeo.2009.02.004.

Davies, G.R., Stolz, A.J., Mahotkin, I.L., Nowell, G.M., and Pearson, D.G., 2006, Trace element and Sr-Pb-Nd-Hf isotope evidence for ancient, fluid-dominated enrichment of the source of Aldan Shield lamproites: Journal of Petrology, v. 47, no. 6, p. 1119–1146, doi: 10.1093/petrology/egl005.

Dawson, J.B., and Hawthorne, J.B., 1973, Magmatic sedimentation and carbonatitic differentiation in kimberlite sills at Benfontein, South Africa: Journal of the Geological Society, v. 129, no. 1, p. 61–85, doi: 10.1144/gsjgs.129.1.0061.

Dawson, J.B., and Smith, J. V., 1977, The MARID (mica-amphibole-rutile-ilmenite-diopside) suite of xenoliths in kimberlite: Geochimica et Cosmochimica Acta, v. 41, no. 2, doi: 10.1016/0016-7037(77)90239-3.

Eggenkamp, H.C. 22, 2014, Advances in Isotope Geochemistry The Geochemistry of Stable Chlorine and Bromine Isotopes Chapter 2:

Eggenkamp, H.G.M., 1994. The Geochemistry of Chlorine Isotopes (Ph.D. Thesis) Universiteit Utrecht, (151 pp.).

Eggenkamp, H.G.M., and Groos, A.F.K. Van, 1997, Chlorine stable isotopes in carbonatites : evidence for isotopic heterogeneity in the mantle: Chemical Geology, v. 140, p. 137–143.

Emeleus, C.H., 1963, Structural and petrographic obsrevations on layered granites from Southern Greenland: Mineralogical Society of America, v. Special pa, no. 1, p. 22–29.

Emeleus, C.H., and Andrews, J.R., 1975, Mineralogy and petrology of kimberlite dyke and sheet intrusions and included peridotite xenoliths from South-West Greenland: Physics and Chemistry of the Earth, v. 9, no. C, p. 179–197, doi: 10.1016/0079-1946(75)90016-6.

Fehn, U., Lu, Z., Tomaru, H., 2006. 129I/I ratios and halogen concentrations in pore water of Hydrate Ridge and their relevance for the origin of gas hydrates: a progress report. In: Trehu, A.M.,

Fehn, U., Snyder, G.T., Muramatsu, Y., 2007. Iodine as a tracer of organic material: 129I results from gas hydrate systems and fore arc fluids. J. Geochem. Explor. 95, 66–80.

Fitton, J.G., 1995, Coupled molybdenum and niobium depletion in continental basalts: Earth and Planetary Science Letters, v. 136, no. 3–4, p. 715–721, doi: 10.1016/0012-821X(95)00171-8.

Frey, F. A., Green, D. H. & Roy, S. D. (1978). Integrated models of basalt petrogenesis

a study of quartz tholeiites to olivine melilitites from south eastern Australia utilizing geochemical and experimental petrological data Journal of Petrology 19, 463–513.

Foley, S., 1992, Vein-plus-wall-rock melting mechanisms in the lithosphere and the origin of potassic alkaline magmas: Lithos, v. 28, no. 3–6, p. 435–453, doi: 10.1016/0024-4937(92)90018-T.

Gaffney, A.M., Blichert-Toft, J., Nelson, B.K., Bizzarro, M., Rosing, M., and Albarède, F., 2007, Constraints on source-forming processes of West Greenland kimberlites inferred from Hf-Nd isotope systematics: Geochimica et Cosmochimica Acta, v. 71, no. 11, p. 2820–2836, doi: 10.1016/j.gca.2007.03.009.

Garde, A.A., Hamilton, M.A., Chadwick, B., Grocott, J., and McCaffrey, K.J.W., 2002, The Ketilidian orogen of South Greenland : geochronology, tectonics, magmatism, and fore-arc accretion during Palaeoproterozoic oblique convergence: Canadian Journal of Earth Sciences, v. 39, no. 5, p. 765–793, doi: 10.1139/E02-026.

Garrit, D., 2002, The nature of the Archaean and Proterozoic lithospheric mantle and lower crust in West Greenland illustrated by the geochemistry and petrography of xenoliths from kimberlites: unpublished ph. d. thesis, University of Copenhagen, pp 289.

Giuliani, A., Kamenetsky, V.S., Phillips, D., Kendrick, M.A., Wyatt, B.A., and Goemann, K., 2012, Nature of alkali-carbonate fluids in the sub-continental lithospheric mantle: Geology, v. 40, no. 11, p. 967–970, doi: 10.1130/G33221.1.

Giuliani, A., Phillips, D., Woodhead, J.D., Kamenetsky, V.S., Fiorentini, M.L., Maas, R., Soltys, A., and Armstrong, R.A., 2015, Did diamond-bearing orangeites originate from MARID-veined peridotites in the lithospheric mantle? Nature Communications, v. 6, p. 6837, doi: 10.1038/ncomms7837.

Goodenough, K.M., Upton, B.G.J., and Ellam, R.M., 2002, Long-term memory of subduction processes in the lithospheric mantle: evidence from the geochemistry of basic dykes in the Gardar Province of South Greenland: Journal of the Geological Society, v. 159, no. 6, p. 705–714, doi: 10.1144/0016-764901-154.

Grégoire, M., Bell, D.R., and le Roex, A., 2003, Garnet Lherzolites from the Kaapvaal Craton (South Africa): Trace Element Evidence for a Metasomatic History: Journal of Petrology, v. 44, no. 4, p. 629–657, doi: 10.1093/petrology/44.4.629.

Grégoire, M., Bell, D., and Le Roex, A., 2002, Trace element geochemistry of phlogopite-rich mafic mantle xenoliths: their classification and their relationship to phlogopite-bearing peridotites and kimberlites revisited: Contributions to Mineralogy and Petrology, v. 142, no. 5, p. 603–625, doi: 10.1007/s00410-001-0315-8.

Griffin, W.L., O'Reilly, S.Y., Afonso, J.C., and Begg, G.C., 2009, The composition and evolution of lithospheric mantle: A re-evaluation and its tectonic implications: Journal of Petrology, v. 50, no. 7, p. 1185–1204, doi: 10.1093/petrology/egn033.

Gudfinnsson, G.H., and Presnall, D.C., 2005, Continuous gradations among primary carbonatitic, kimberlitic, melilititic, basaltic, picritic, and komatiitic melts in equilibrium with garnet lherzolite at 3-8 GPa: Journal of Petrology, v. 46, no. 8, p. 1645–1659, doi: 10.1093/petrology/egi029.

Halldórsson, S.A., Barnes, J.D., Stefánsson, A., Hilton, D.R., Hauri, E.H., and Marshall, E.W., 2016, Subducted lithosphere controls halogen enrichments in the Iceland mantle plume source: Geology, v. 44, no. 8, p. 679–682, doi: 10.1130/G37924.1.

Harte, B., 1983. Mantle peridotites and processes the kimberlites sample. *Continental basalts and mantle.* Shiva Press (1983), pp. 46-91

Heaman, L.M., and Kjarsgaard, B.A., 2000, Timing of eastern North American kimberlite magmatism: Continental extension of the Great Meteor hotspot track? Earth and Planetary Science Letters, v. 178, no. 3–4, p. 253–268, doi: 10.1016/S0012-821X(00)00079-0.

Heaman, L.M., Kjarsgaard, B.A., and Creaser, R.A., 2004, The temporal evolution of North American kimberlites: Lithos, v. 76, no. 1–4 SPEC. ISS., p. 377–397, doi: 10.1016/j.lithos.2004.03.047.

Hofmann, A.W., 1988, Chemical differentiation of the Earth: the relationship between mantle, continental crust, and oceanic crust: Earth and Planetary Science Letters, v. 90, no. 3, p. 297–314, doi: 10.1016/0012-821X(88)90132-X.

Irvine, G.J., Pearson, D.G., Kjarsgaard, B.A., Carlson, R.W., Kopylova, M.G., and Dreibus, G., 2003, A Re–Os isotope and PGE study of kimberlite-derived peridotite xenoliths from Somerset Island and a comparison to the Slave and Kaapvaal cratons: Lithos, v. 71, no. 2–4, p. 461–488, doi: 10.1016/S0024-4937(03)00126-9.

Jambon, A., Déruelle, B., Dreibus, G., and Pineau, F., 1995, Chlorine and bromine abundance in MORB: the contrasting behaviour of the Mid-Atlantic Ridge and

East Pacific Rise and implications for chlorine geodynamic cycle: Chemical Geology, v. 126, no. 2, p. 101–117, doi: 10.1016/0009-2541(95)00112-4.

Jambon, A., Weber, H.W., and Begemann, F., 1985, Helium and argon from an Atlantic MORB glass: concentration, distribution and isotopic composition: Earth and Planetary Science Letters, v. 73, no. 2–4, p. 255–268, doi: 10.1016/0012-821X(85)90074-3.

Jarosewich, E., Nelen, J. a, and Norberg, J., 1980, Reference samples for electron microprobe analysis: Geostand. Newsl., v. 4, no. 22, p. 43–47.

Joachim, B., Pawley, A., Lyon, I.C., Marquardt, K., Henkel, T., Clay, P.L., Ruzié, L., Burgess, R., and Ballentine, C.J., 2014, Experimental partitioning of F and Cl between olivine, orthopyroxene and silicate melt at Earth's mantle conditions: Chemical Geology, v. 416, p. 65–78, doi: 10.1016/j.chemgeo.2015.08.012.

John, T., Layne, G.D., Haase, K.M., and Barnes, J.D., 2010, Chlorine isotope evidence for crustal recycling into the Earth's mantle: Earth and Planetary Science Letters, v. 298, no. 1–2, p. 175–182, doi: 10.1016/j.epsl.2010.07.039.

John, T., Scambelluri, M., Frische, M., Barnes, J.D., and Bach, W., 2011, Dehydration of subducting serpentinite: Implications for halogen mobility in subduction zones and the deep halogen cycle: Earth and Planetary Science Letters, v. 308, no. 1–2, p. 65–76, doi: 10.1016/j.epsl.2011.05.038.

Johnson, L.H., Burgess, R., Turner, G., Milledge, H.J., and Harris, J.W., 2000, Noble gas and halogen geochemistry of mantle fluids: Comparison of African and Canadian diamonds: Geochimica et Cosmochimica Acta, v. 64, no. 4, p. 717–732, doi: 10.1016/S0016-7037(99)00336-1.

Jones, A.P., Smith, J.V. and Dawson, J.B., 1982. Mantle metasomatism in 14 veined peridotites from Bultfontein Mine, South Africa. The Journal of Geology, 90(4), pp.435-453.

Kamenetsky, V.S., Golovin, A. V., Maas, R., Giuliani, A., Kamenetsky, M.B., and Weiss, Y., 2014, Towards a new model for kimberlite petrogenesis: Evidence from unaltered kimberlites and mantle minerals: Earth-Science Reviews, v. 139, p. 145–167, doi: 10.1016/j.earscirev.2014.09.004.

Kamenetsky, V.S., Kamenetsky, M.B., Sobolev, A. V., Golovin, A. V., Demouchy, S., Faure, K., Sharygin, V. V., and Kuzmin, D. V., 2008, Olivine in the Udachnaya-East kimberlite (Yakutia, Russia): Types, compositions and origins: Journal of Petrology, v. 49, no. 4, p. 823–839, doi: 10.1093/petrology/egm033.

Kamenetsky, V.S., Kamenetsky, M.B., Weiss, Y., Navon, O., Nielsen, T.F.D., and Mernagh, T.P., 2009a, How unique is the Udachnaya-East kimberlite? Comparison with kimberlites from the Slave Craton (Canada) and SW Greenland: Lithos, v. 112, p. 334–346, doi: 10.1016/j.lithos.2009.03.032.

Kamenetsky, V.S., Maas, R., Kamenetsky, M.B., Paton, C., Phillips, D., Golovin, A. V., and Gornova, M.A., 2009b, Chlorine from the mantle: Magmatic halides in the Udachnaya-East kimberlite, Siberia.:

Kamenetsky, V.S., Mitchell, R.H., Maas, R., Giuliani, A., Gaboury, D., and Zhitova, L., 2015, Chlorine in mantle-derived carbonatite melts revealed by halite in the St.-Honore intrusion (Quebec, Canada): Geology, v. 43, no. 8, p. 687–690, doi: 10.1130/G36843.1.

Kamenetsky, M.B., Sobolev, A. V., Kamenetsky, V.S., Maas, R., Danyushevsky, L. V., Thomas, R., Pokhilenko, N.P., and Sobolev, N. V., 2004, Kimberlite melts rich in alkali chlorides and carbonates: A potent metasomatic agent in the mantle: Geology, v. 32, no. 10, p. 845–848, doi: 10.1130/G20821.1.

Kargel, J.S., and Lewis, J.S., 1993, The composition and evolution of the early Earth: Icarus, v. 105, p. 1–25.

Kendrick, M.A., Arculus, R.J., Danyushevsky, L. V., Kamenetsky, V.S., Woodhead, J.D., and Honda, M., 2014a, Subduction-related halogens (Cl, Br and I) and H2O in magmatic glasses from Southwest Pacific Backarc Basins: Earth and Planetary Science Letters, v. 400, p. 165–176, doi: 10.1016/j.epsl.2014.05.021.

Kendrick, M.A., Hémond, C., Kamenetsky, V.S., Danyushevsky, L., Devey, C.W., Rodemann, T., Jackson, M.G., and Perfit, M.R., 2017, Seawater cycled throughout Earth's mantle in partially serpentinized lithosphere: Nature Geoscience, v. 10, no. February, doi: 10.1038/ngeo2902.

Kendrick, M.A., Honda, M., Pettke, T., Scambelluri, M., Phillips, D., and Giuliani, A., 2013, Subduction zone fluxes of halogens and noble gases in seafloor and forearc serpentinites: Earth and Planetary Science Letters, v. 365, p. 86–96, doi: 10.1016/j.epsl.2013.01.006.

Kendrick, M.A., Jackson, M.G., Hauri, E.H., and Phillips, D., 2015, The halogen (F, Cl, Br, I) and H2O systematics of Samoan lavas: Assimilated-seawater, EM2 and high-3He/4He components.:

Kendrick, M.A., Jackson, M.G., Kent, A.J.R., Hauri, E.H., Wallace, P.J., and Woodhead, J., 2014b, Contrasting behaviours of CO2, S, H2O and halogens (F, Cl,

Br, and I) in enriched-mantle melts from Pitcairn and Society seamounts: Chemical Geology, v. 370, p. 69–81, doi: 10.1016/j.chemgeo.2014.01.019.

Kendrick, M.A., Scambelluri, M., Honda, M., and Phillips, D., 2011, High abundances of noble gas and chlorine delivered to the mantle by serpentinite subduction: Nature Geoscience, v. 4, no. 11, p. 807–812, doi: 10.1038/ngeo1270.

Kendrick, M.A., Woodhead, J.D., and Kamenetsky, V.S., 2012, Tracking halogens through the subduction cycle: Geology, v. 40, no. 12, p. 1075–1078, doi: 10.1130/G33265.1.

Kjarsgaard, B.A., Pearson, D.G., Tappe, S., Nowell, G.M., and Dowall, D.P., 2009, Geochemistry of hypabyssal kimberlites from Lac de Gras, Canada: Comparisons to a global database and applications to the parent magma problem: Lithos, v. 112, p. 236–248, doi: 10.1016/j.lithos.2009.06.001.

Knauth, L.P., 2005, Temperature and salinity history of the Precambrian ocean: Implications for the course of microbial evolution: Palaeogeography, Palaeoclimatology, Palaeoecology, v. 219, no. 1–2, p. 53–69, doi: 10.1016/j.palaeo.2004.10.014.

Kodolányi, J., and Pettke, T., 2011, Loss of trace elements from serpentinites during fluid-assisted transformation of chrysotile to antigorite - An example from Guatemala: Chemical Geology, v. 284, no. 3–4, p. 351–362, doi: 10.1016/j.chemgeo.2011.03.016.

Kodolányi, J., Pettke, T., Spandler, C., Kamber, B.S., and Ling, K.G., 2012, Geochemistry of ocean floor and fore-arc serpentinites: Constraints on the ultramafic input to subduction zones: Journal of Petrology, v. 53, no. 2, p. 235–270, doi: 10.1093/petrology/egr058.

Köhler, J., Schönenberger, J., Upton, B., and Markl, G., 2009, Halogen and trace-element chemistry in the Gardar Province, South Greenland: Subduction-related mantle metasomatism and fluid exsolution from alkalic melts: Lithos, v. 113, no. 3–4, p. 731–747, doi: 10.1016/j.lithos.2009.07.004.

Konzett, J., Armstrong, R.A., Sweeney, R.J., and Compston, W., 1998, The timing of MARID metasomatism in the Kaapvaal mantle: an ion probe study of zircons from MARID xenoliths: Earth and Planetary Science Letters, v. 160, no. 1–2, p. 133–145, doi: 10.1016/S0012-821X(98)00073-9.

Konzett, J., Sweeney, R.J., Thompson, a. B., and Ulmer, P., 1997, Potassium Amphibole Stability in the Upper Mantle: an Experimental Study in a Peralkaline

KNCMASH System to 8.5 GPa: Journal of Petrology, v. 38, no. 5, p. 537–568, doi: 10.1093/petroj/38.5.537.

Kopylova, M.G., Gaudet, M., Kostrovitsky, S.I., Polozov, A.G., and Yakovlev, D.A., 2016, Origin of salts and alkali carbonates in the Udachnaya East kimberlite: Insights from petrography of kimberlite phases and their carbonate and evaporite xenoliths: Journal of Volcanology and Geothermal Research, v. 327, p. 116–134, doi: 10.1016/j.jvolgeores.2016.07.003.

Kopylova, M.G., Kostrovitsky, S.I., and Egorov, K.N., 2013, Salts in southern Yakutian kimberlites and the problem of primary alkali kimberlite melts: Earth-Science Reviews, v. 119, p. 1–16, doi: 10.1016/j.earscirev.2013.01.007.

Kopylova, M.G., Matveev, S., and Raudsepp, M., 2007, Searching for parental kimberlite melt: Geochimica et Cosmochimica Acta, v. 71, no. 14, p. 3616–3629, doi: 10.1016/j.gca.2007.05.009.

Kramers, J.D., 2003, Volatile element abundance patterns and an early liquid water ocean on Earth: Precambrian Research, v. 126, no. 3–4, p. 379–394, doi: 10.1016/S0301-9268(03)00106-2.

Van Kranendonk, M.J., St-Onge, M.R., and Henderson, J.R., 1993, Paleoproterozoic tectonic assembly of Northeast Laurentia through multiple indentations: Precambrian Research, v. 63, no. 3–4, p. 325–347, doi: 10.1016/0301-9268(93)90039-5.

Larsen, L.M., Sørensen, H., 1987. The Illímaussaq intrusion - progressive crystallization and formation of layering in an agpaitic magma. In: Fitton, J.G., Upton, B.G.J. (eds.): Alkaline igneous rocks. Geological Society Special Publication (London) 30, 473–488.

Larsen, L.M., Heaman, L.M., Creaser, R. a., Duncan, R. a., Frei, R., and Hutchison, M., 2009, Tectonomagmatic events during stretching and basin formation in the Labrador Sea and the Davis Strait: evidence from age and composition of Mesozoic to Palaeogene dyke swarms in West Greenland: Journal of the Geological Society, v. 166, no. 6, p. 999–1012, doi: 10.1144/0016-76492009-038.

Larsen, L.M., and Rex, D.C., 1992, A review of the 2500 Ma span of alkaline-ultramafic, potassic and carbonatitic magmatism in West Greenland: Lithos, v. 28, no. 3–6, p. 367–402, doi: 10.1016/0024-4937(92)90015-Q.

Lee, C.T.A., 2003. Compositional variation of density and seismic velocities in natural peridotites at STP conditions: Implications for seismic imaging of compositional

heterogeneities in the upper mantle. Journal of Geophysical Research: Solid Earth, 108(B9).

Li, X., Wang, Y., and Zhang, Q., 2016, Determination of halogen levels in marine geological samples: Spectroscopy Letters, v. 49, no. 3, p. 151–154, doi: 10.1080/00387010.2015.1109522.

Lyubetskaya, T., and Korenaga, J., 2007, Chemical composition of Earth's primitive mantle and its variance: 1. Method and results: Journal of Geophysical Research: Solid Earth, v. 112, no. 3, p. 1–21, doi: 10.1029/2005JB004223.

Magenheim, A.J., Spivack, A.J., Volpe, C., and Ransom, B., 1994, Precise Determination of Stable Chlorine Isotopic-Ratios in Low-Concentration Natural Samples: Geochimica et Cosmochimica Acta, v. 58, no. 14, p. 3117–3121.

Le Maitre, R.W., Streckeisen, A., Zanettin, B., Le Bas, M.J., Bonin, B., and Bateman, P., 2002, Igneous rocks: a classification and glossary of terms: recommendations of the International Union of Geological Sciences Subcommission on the Systematics of Igneous Rocks: Cambridge University Press.

Manzini, M., Bouvier, A.-S., Barnes, J.D., Bonifacie, M., Rose-Koga, E.F., Ulmer, P., Métrich, N., Bardoux, G., Williams, J., Layne, G.D., Straub, S., Baumgartner, L.P., and John, T., 2017, SIMS chlorine isotope analyses in melt inclusions from arc settings: Chemical Geology, v. 449, p. 112–122, doi: 10.1016/j.chemgeo.2016.12.002.

McDonough, W.F., 2003, Compositional model for the Earth's core, in Treatise on Geochemistry, p. 547–568.

McDonough, W.F., and Sun, S. s., 1995, The composition of the Earth: Chemical Geology, v. 120, no. 3–4, p. 223–253, doi: 10.1016/0009-2541(94)00140-4.

Mitchell, R.H., 1995, Kimberlites, Orangeites and Related Rocks: Springer Science & Business Media.

Mitchell, R.H., 2013, Paragenesis and oxygen isotopic studies of serpentine in kimberlite. In: Proceedings of 10th International Kimberlite Conference (pp. 1-12). Springer, New Delhi.

Mitchell, R.H., 2006, Potassic magmas derived from metasomatized lithospheric mantle: Nomenclature and relevance to exploration for diamond-bearing rocks: Journal of the Geological Society of India, v. 67, no. 3, p. 317–327.

Mitchell, Roger H., and Bergman, S.C., 1991, Petrology of Lamproites:

Morgan, J.W., and Anders, E., 1980, Chemical composition of Earth, Venus, and Mercury: Proceedings of the National Academy of Sciences, v. 77, no. 12, p. 6973–6977, doi: 10.1073/pnas.77.12.6973.

Muramatsu, Y., Fehn, U., and Yoshida, S., 2001, Recycling of iodine in fore-arc areas: Evidence from the iodine brines in Chiba, Japan: Earth and Planetary Science Letters, v. 192, no. 4, p. 583–593, doi: 10.1016/S0012-821X(01)00483-6.

Murphy, D.T., Collerson, K.D., and Kamber, B.S., 2002, Lamproites from gaussberg, Antarctica: Possible transition zone melts of archaean subducted sediments: Journal of Petrology, v. 43, no. 6, p. 981–1001, doi: 10.1093/petrology/43.6.981.

Nelson, D.R., 1989, Isotopic characteristics and petrogenesis of the lamproites and kimberlites of central west Greenland: Lithos, v. 22, no. 4, p. 265–274, doi: 10.1016/0024-4937(89)90029-7.

Nielsen, T.F.D., Jensen, S.M., Secher, K., and Sand, K.K., 2009, Distribution of kimberlite and aillikite in the Diamond Province of southern West Greenland: A regional perspective based on groundmass mineral chemistry and bulk compositions: Lithos, v. 112, p. 358–371, doi: 10.1016/j.lithos.2009.05.035.

Pamato, M.G., Myhill, R., Boffa Ballaran, T., Frost, D.J., Heidelbach, F., and Miyajima, N., 2014, Lower-mantle water reservoir implied by the extreme stability of a hydrous aluminosilicate: Nature Geoscience, v. 8, no. 1, p. 75–79, doi: 10.1038/ngeo2306.

Park, R.G., 1994, Early Proterozoic tectonic overview of the northern British Isles and neighbouring terrains in Laurentia and Baltica: Precambrian Research, v. 68, no. 1–2, p. 65–79, doi: 10.1016/0301-9268(94)90065-5.

Park, R.G., 1995, Palaeoproterozoic Laurentia-Baltica relationships: a view from the Lewisian: Geological Society, London, Special Publications, v. 95, no. 1, p. 211–224, doi: 10.1144/GSL.SP.1995.095.01.13.

Parthasarathy, G., Chetty, T.R.K., and Haggerty, S.E., 2002, Thermal stability and spectroscopic studies of zemkorite: A carbonate from the Venkatampalle kimberlite of southern India: American Mineralogist, v. 87, no. 10, p. 1384–1389.

Paul, D.K., Buckley, F., and Nixon, P.H., 1976, Fluroine and chlorine geochemistry of kimberlites: Chemical Geology, v. 17.

Pearson, D.G., Brenker, F.E., Nestola, F., McNeill, J., Nasdala, L., Hutchison, M.T., Matveev, S., Mather, K., Silversmit, G., Schmitz, S., Vekemans, B., and Vincze,

L., 2014, Hydrous mantle transition zone indicated by ringwoodite included within diamond.: Nature, v. 507, no. 7491, p. 221–4, doi: 10.1038/nature13080.

Pearson, D.G., Carlson, R.W., Shirey, S.B., Boyd, F.R., and Nixon, P.H., 1995a, Stabilisation of Archaean lithospheric mantle: A ReOs isotope study of peridotite xenoliths from the Kaapvaal craton: Earth and Planetary Science Letters, v. 134, no. 3–4, p. 341–357, doi: 10.1016/0012-821X(95)00125-V.

Pearson, D.G., Shirey, S.B., Carlson, R.W., Boyd, F.R., Pokhilenko, N.P., and Shimizu, N., 1995b, ReOs, SmNd, and RbSr isotope evidence for thick Archaean lithospheric mantle beneath the Siberian craton modified by multistage metasomatism: Geochimica et Cosmochimica Acta, v. 59, no. 5, p. 959–977, doi: 10.1016/0016-7037(95)00014-3.

Peslier, A.H., 2010, A review of water contents of nominally anhydrous natural minerals in the mantles of Earth, Mars and the Moon: Journal of Volcanology and Geothermal Research, v. 197, no. 1–4, p. 239–258, doi: 10.1016/j.jvolgeores.2009.10.006.

Prelević, D., Foley, S.F., Romer, R., and Conticelli, S., 2008, Mediterranean tertiary lamproites derived from multiple source components in postcollisional geodynamics: Geochimica et Cosmochimica Acta, v. 72, no. 8, p. 2125–2156, doi: 10.1016/j.gca.2008.01.029.

Pyle, D.M., and Mather, T.A., 2009, Halogens in igneous processes and their fluxes to the atmosphere and oceans from volcanic activity: A review: Chemical Geology, v. 263, no. 1–4, p. 110–121, doi: 10.1016/j.chemgeo.2008.11.013.

Ringwood, A.E., 1962, A model for the upper mantle: Journal of Geophysical Research: Planets, v. 67, p. 858–867.

Roberge, M., Bureau, H., Bolfan-Casanova, N., Frost, D.J., Raepsaet, C., Surble, S., Khodja, H., Auzende, A.L., and Fiquet, G., 2015, Is the transition zone a deep reservoir for fluorine? Earth and Planetary Science Letters, v. 429, p. 25–32, doi: 10.1016/j.epsl.2015.07.051.

Rock, N.M.S., 1991, Lamprophyres: s. Blackie, Glasgow, U.K

Le Roex, A., 2003, Petrogenesis of Group I Kimberlites from Kimberley, South Africa: Evidence from Bulk-rock Geochemistry: Journal of Petrology, v. 44, no. 12, p. 2261–2286, doi: 10.1093/petrology/egg077.

Le Roex, A., and Class, C., 2016, Metasomatic enrichment of Proterozoic mantle south of the Kaapvaal Craton, South Africa: origin of sinusoidal REE patterns in

clinopyroxene and garnet: Contributions to Mineralogy and Petrology, v. 171, no. 2, p. 1–24, doi: 10.1007/s00410-015-1222-8.

Rudnick, R.L., Barth, M., Horn, I., and McDonough, W.F., 2000, Rutile-Bearing Refractory Eclogites: Missing Link Between Continents and Depleted Mantle: Science, v. 287, no. 5451, p. 278–281, doi: 10.1126/science.287.5451.278.

Rudnick, R.L. and Gao, S., 2003. Composition of the continental crust. Treatise on geochemistry, 3, p.659.

Rudnick, R.L., McDonough, W.F., and Chappell, B.W., 1993, Carbonatite metasomatism in the northern Tanzanian mantle: petrographic and geochemical characteristics: Earth and Planetary Science Letters, v. 114, no. 4, p. 463–475, doi: 10.1016/0012-821X(93)90076-L.

Saal, A.E., Hauri, E.H., Langmuir, C.H., and Perfit, M.R., 2002, Vapour undersaturation in primitive mid-ocean-ridge basalt and the volatile content of Earth's upper mantle: Nature, v. 419, no. 6906, p. 451–455, doi: 10.1038/nature01073.

Schauble, E. a, Rossman, G.R., and Taylor, H.P.J., 2003, Theoretical estimates of equilibrium chlorine-isotope fractionations, Geochimica et Cosmochimica Acta: Geochim Cosmochim Acta, v. 67, no. 17, p. 3267–3281, doi: 10.1016/S0016-7037(00)01375-3.

Schmidt, M.W., and Poli, S., 2013, Devolatilization During Subduction: Elsevier Ltd.

Schwartz, S., Guillot, S., Reynard, B., Lafay, R., Debret, B., Nicollet, C., Lanari, P., and Auzende, A.L., 2013, Pressure-temperature estimates of the lizardite/antigorite transition in high pressure serpentinites: Lithos, v. 178, p. 197–210, doi: 10.1016/j.lithos.2012.11.023.

Selverstone, J., and Sharp, Z.D., 2015, Chlorine isotope behavior during prograde metamorphism of sedimentary rocks: Earth and Planetary Science Letters, v. 417, p. 120–131, doi: 10.1016/j.epsl.2015.02.030.

Shannon, R.D., 1976, Revised effective ionic radii and systematic studies of interatomic distances in halides and chalcogenides: Acta Crystallographica Section A, v. 32, no. 5, p. 751–767, doi: 10.1107/S0567739476001551.

Sharp, Z.D., Barnes, J.D., Brearley, a J., Chaussidon, M., Fischer, T.P., and Kamenetsky, V.S., 2007, Chlorine isotope homogeneity of the mantle, crust and carbonaceous chondrites.: Nature, v. 446, no. 7139, p. 1062–1065, doi: 10.1038/nature05748.

Sharp, Z.D., and Draper, D.S., 2013, The chlorine abundance of Earth: Implications for a habitable planet: Earth and Planetary Science Letters, v. 369–370, p. 71–77, doi: 10.1016/j.epsl.2013.03.005.

Sharp, Z.D., Mercer, J.A., Jones, R.H., Brearley, A.J., Selverstone, J., Bekker, A., and Stachel, T., 2013, The chlorine isotope composition of chondrites and Earth: Geochimica et Cosmochimica Acta, v. 107, p. 189–204, doi: 10.1016/j.gca.2013.01.003.

Simon, N.S.C., Carlson, R.W., Pearson, D.G., and Davies, G.R., 2007, The origin and evolution of the Kaapvaal Cratonic Lithospheric Mantle: Journal of Petrology, v. 48, no. 3, p. 589–625, doi: 10.1093/petrology/egl074.

Smith, C.B., 1983, Pb, Sr and Nd isotopic evidence for sources of southern African Cretaceous kimberlites: Nature, v. 304, no. 5921, p. 51–54, doi: 10.1038/304051a0.

Smith, J. V., Delaney, J.S., Hervig, R.L., and Dawson, J.B., 1981, Storage of F and Cl in the upper mantle: geochemical implications: Lithos, v. 14, no. 2, p. 133–147, doi: 10.1016/0024-4937(81)90050-5.

Stamm, N., and Schmidt, M.W., 2017, Asthenospheric kimberlites: Volatile contents and bulk compositions at 7 GPa: Earth and Planetary Science Letters, v. 474, p. 309–321, doi: 10.1016/j.epsl.2017.06.037.

Straub, S.M., and Layne, G.D., 2003, The systematics of chlorine, fluorine, and water in Izu arc front volcanic rocks: Implications for volatile recycling in subduction zones: Geochimica et Cosmochimica Acta, v. 67, no. 21, p. 4179–4203, doi: 10.1016/S0016-7037(03)00307-7.

Sudo, A., and Tatsumi, Y., 1990, Phlogopite and K-amphibole in the upper mantle: Implication for magma genesis in subduction zones: Geophysical Research Letters, v. 17, no. 1, p. 29–32.

Sun, S.S., 1982, Chemical composition and origin of the earth's primitive mantle: Geochimica et Cosmochimica Acta, v. 46, no. 2, p. 179–192, doi: 10.1016/0016-7037(82)90245-9.

Tachibana, Y., Kaneoka, I., Gaffney, A., and Upton, B., 2006, Ocean-island basalt-like source of kimberlite magmas from West Greenland revealed by high 3He/4He ratios: Geology, v. 34, no. 4, p. 273–276, doi: 10.1130/G22201.1.

Tappe, S., Foley, S.F., Jenner, G.A., Heaman, L.M., Kjarsgaard, B.A., Romer, R.L., Stracke, A., Joy, N., and Hoefs, J., 2006, Genesis of Ultramafic Lamprophyres and

Carbonatites at Aillik Bay, Labrador: a Consequence of Incipient Lithospheric Thinning beneath the North Atlantic Craton: Journal of Petrology, v. 47, no. 7, p. 1261–1315, doi: 10.1093/petrology/egl008.

Tappe, S., Foley, S.F., Jenner, G.A., and Kjarsgaard, B.A., 2005, Integrating ultramafic lamprophyres into the IUGS classification of igneous rocks: Rationale and implications: Journal of Petrology, v. 46, no. 9, p. 1893–1900, doi: 10.1093/petrology/egi039.

Tappe, S., Foley, S.F., Kjarsgaard, B.A., Romer, R.L., Heaman, L.M., Stracke, A., and Jenner, G.A., 2008, Between carbonatite and lamproite—Diamondiferous Torngat ultramafic lamprophyres formed by carbonate-fluxed melting of cratonic MARID-type metasomes: Geochimica et Cosmochimica Acta, v. 72, no. 13, p. 3258–3286, doi: 10.1016/j.gca.2008.03.008.

Tappe, S., Foley, S.F., Stracke, A., Romer, R.L., Kjarsgaard, B.A., Heaman, L.M., and Joyce, N., 2007, Craton reactivation on the Labrador Sea margins: 40Ar/39Ar age and Sr-Nd-Hf-Pb isotope constraints from alkaline and carbonatite intrusives: Earth and Planetary Science Letters, v. 256, no. 3–4, p. 433–454, doi: 10.1016/j.epsl.2007.01.036.

Tappe, S., Jenner, G.A., Foley, S.F., Heaman, L., Besserer, D., Kjarsgaard, B.A., and Ryan, B., 2004, Torngat ultramafic lamprophyres and their relation to the North Atlantic Alkaline Province: Lithos, v. 76, no. 1–4 SPEC. ISS., p. 491–518, doi: 10.1016/j.lithos.2004.03.040.

Tappe, S., Pearson, D.G., Nowell, G., Nielsen, T., Milstead, P., and Muehlenbachs, K., 2011, A fresh isotopic look at Greenland kimberlites: Cratonic mantle lithosphere imprint on deep source signal: Earth and Planetary Science Letters, v. 305, no. 1–2, p. 235–248, doi: 10.1016/j.epsl.2011.03.005.

Tappe, S., Romer, R.L., Stracke, A., Steenfelt, A., Smart, K.A., Muehlenbachs, K., and Torsvik, T.H., 2017, Sources and mobility of carbonate melts beneath cratons, with implications for deep carbon cycling, metasomatism and rift initiation: Earth and Planetary Science Letters, v. 466, p. 152–167, doi: 10.1016/j.epsl.2017.03.011.

Tappe, S., Steenfelt, A., Heaman, L.M., and Simonetti, A., 2009, The newly discovered Jurassic Tikiusaaq carbonatite-aillikite occurrence, West Greenland, and some remarks on carbonatite–kimberlite relationships: Lithos, v. 112, p. 385–399, doi: 10.1016/j.lithos.2009.03.002.

Tappe, S., Steenfelt, A., and Nielsen, T., 2012, Asthenospheric source of Neoproterozoic and Mesozoic kimberlites from the North Atlantic craton, West Greenland: New high-precision U-Pb and Sr-Nd isotope data on perovskite: Chemical Geology, v. 320–321, p. 113–127, doi: 10.1016/j.chemgeo.2012.05.026.

Taylor, W.R., Tompkins, L.A., and Haggerty, S.E., 1994, Comparative geochemistry of West African kimberlites: Evidence for a micaceous kimberlite endmember of sublithospheric origin: Geochimica et Cosmochimica Acta, v. 58, no. 19, p. 4017–4037, doi: 10.1016/0016-7037(94)90264-X.

Tomlinson, E.L., Jones, A.P., and Harris, J.W., 2006, Co-existing fluid and silicate inclusions in mantle diamond: Earth and Planetary Science Letters, v. 250, no. 3–4, p. 581–595, doi: 10.1016/j.epsl.2006.08.005.

Tomlinson, E.L., Müller, W., and Edinburgh Ion Microprobe Facility, 2009, A snapshot of mantle metasomatism: Trace element analysis of coexisting fluid (LA-ICP-MS) and silicate (SIMS) inclusions in fibrous diamonds: Earth and Planetary Science Letters, v. 279, no. 3–4, p. 362–372, doi: 10.1016/j.epsl.2009.01.010.

Tonarini, S., Leeman, W.P., and Leat, P.T., 2011, Subduction erosion of forearc mantle wedge implicated in the genesis of the South Sandwich Island (SSI) arc: Evidence from boron isotope systematics: Earth and Planetary Science Letters, v. 301, no. 1–2, p. 275–284, doi: 10.1016/j.epsl.2010.11.008.

Ulmer, P., and Trommsdorff, V., 1995, Serpentine Stability to Mantle Depths and Subduction-Related Magmatism: Science, v. 268, no. 5212, p. 858–861, doi: 10.1126/science.268.5212.858.

Veksler, I. V., Petibon, C., Jenner, G.A., Dorfman, A.M., and Dingwell, D.B., 1998, Trace Element Partitioning in Immiscible Silicate-Carbonate Liquid Systems: an Initial Experimental Study Using a Centrifuge Autoclave: Journal of Petrology, v. 39, no. 11–12, p. 2095–2104, doi: 10.1093/petroj/39.11-12.2095.

Wagner, P. A. 1928. The evidence of kimberlite pipes on the constitution of the outer part of the earth. S. Afr. J. Sei. 25: 127-48

Wang, C., Liu, Y., Min, N., Zong, K., Hu, Z., and Gao, S., 2016, Paleo-Asian oceanic subduction-related modification of the lithospheric mantle under the North China Craton: Evidence from peridotite xenoliths in the Datong basalts: Lithos, v. 261, p. 109–127, doi: 10.1016/j.lithos.2015.12.011.

Walter, M.J., 2003. Melt extraction and compositional variability in mantle lithosphere. Treatise on geochemistry, 2, p.568.

Wardle, R.J., and Hall, J., 2002, Proterozoic evolution of the northeastern Canadian shield: Lithoprobe Eastern Canadian Shield Onshore-Offshore Transect (ECSOOT), introduction and summary: Canadian Journal of Earth Sciences, v. 39, no. 5, p. 563–567, doi: 10.1139/e02-029.

Watkinson, W.H.., and Chao, G.Y., 1973, Shortite in Kimberlite from the Upper Canada Gold Mine , Ontario Author (s): David H . Watkinson and G. Y. Chao Published by : The University of Chicago Press Stable URL : http://www.jstor.org/stable/30061149: Journal of Geology, v. 81, no. 2, p. 229–233.

Weiss, Y., McNeill, J., Pearson, D.G., Nowell, G.M., and Ottley, C.J., 2015, Highly saline fluids from a subducting slab as the source for fluid-rich diamonds: Nature, v. 524, no. 7565, p. 339–342, doi: 10.1038/nature14857.

Weyer S., Mu ¨nker C., Mezger K., 2003, Nb/Ta, Zr/Hf and REE in the depleted mantle: implications for the differentiation history of the crust-mantle system. Earth Planet Sci Lett 205(3–4): 309–324

Wilbur, D.S., 2013, Enigmatic astatine: Nature Chemistry, v. 5, no. 3, p. 246–246, doi: 10.1038/nchem.1580.

Wittig, N., Pearson, D.G., Webb, M., Ottley, C.J., Irvine, G.J., Kopylova, M., Jensen, S.M., and Nowell, G.M., 2008, Origin of cratonic lithospheric mantle roots: A geochemical study of peridotites from the North Atlantic Craton, West Greenland: Earth and Planetary Science Letters, v. 274, no. 1–2, p. 24–33, doi: 10.1016/j.epsl.2008.06.034.

Wittig, N., Webb, M., Pearson, D.G., Dale, C.W., Ottley, C.J., Hutchison, M., Jensen, S.M., and Luguet, A., 2010, Formation of the North Atlantic Craton: Timing and mechanisms constrained from Re-Os isotope and PGE data of peridotite xenoliths from S.W. Greenland: Chemical Geology, v. 276, no. 3–4, p. 166–187, doi: 10.1016/j.chemgeo.2010.06.002.

Woolley, A.R., and Kjarsgaard, B.A., 2008, Paragenetic types of carbonatite as indicated by the diversity and relative abundances of associated silicate rocks: Evidence from a global database: Canadian Mineralogist, v. 46, no. 4, p. 741–752, doi: 10.3749/canmin.46.4.741.

Yaxley, G.M., Crawford, A.J., and Green, D.H., 1991, Evidence for carbonatite metasomatism in spinel peridotite xenoliths from western Victoria, Australia: Earth

and Planetary Science Letters, v. 107, no. 2, p. 305–317, doi: 10.1016/0012-821X(91)90078-V.

Yaxley, G.M., Green, D.H., and Kamenetsky, V., 1998, Carbonatite Metasomatism in the Southeastern Australian Lithosphere: Journal of Petrology, v. 39, no. 11–12, p. 1917–1930, doi: 10.1093/petroj/39.11-12.1917.